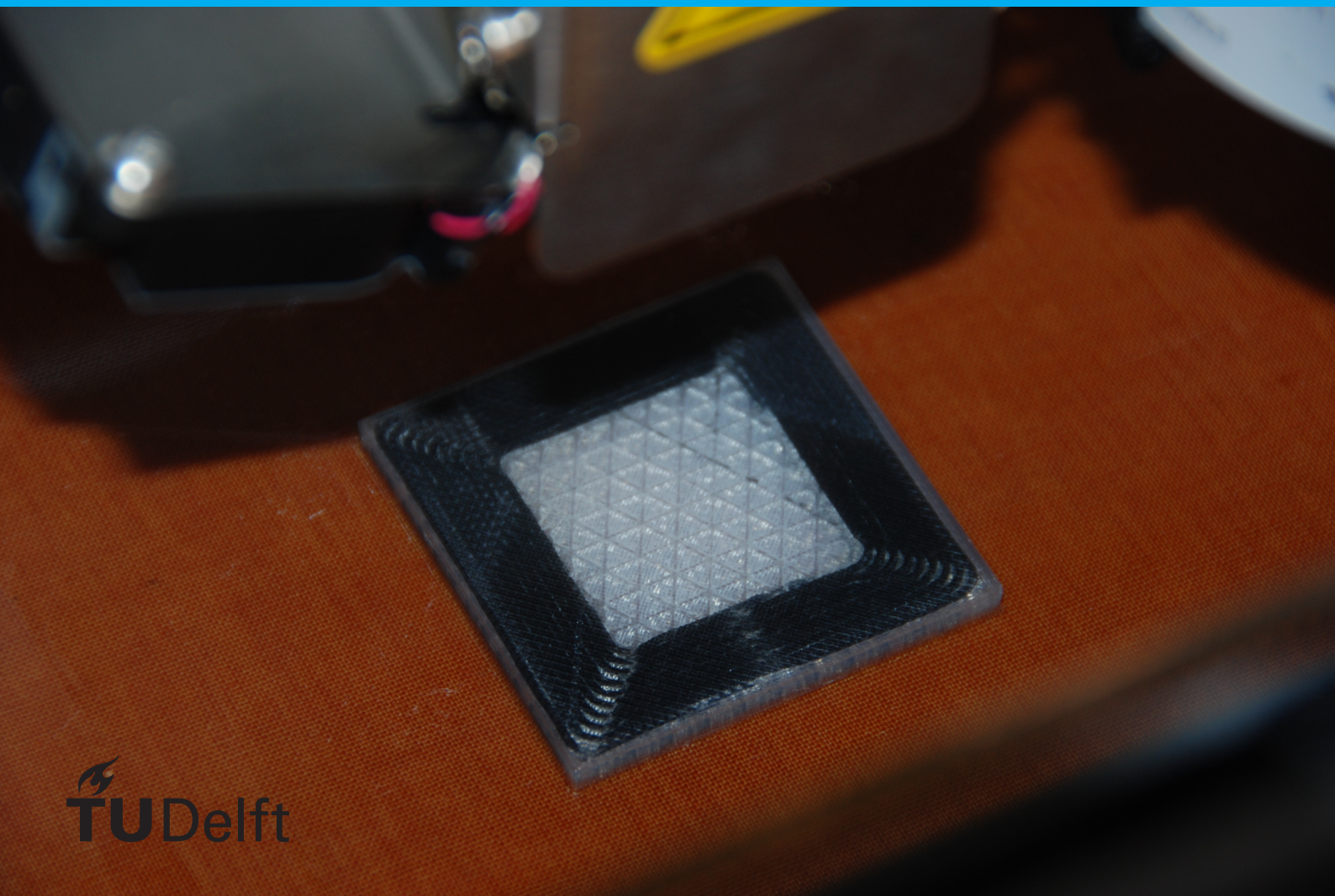


3D Printed Unidirectional Carbon Fibre Reinforced Poly- mers for Aerospace Applications

F. van der Klift
MSc. Student
Material Science and Engineering



3D Printed Unidirectional Carbon Fibre Reinforced Polymers for Aerospace Applications

by

F. van der Klift
MSc. Student
Material Science and Engineering

to obtain the degree of Master of Science
at the Delft University of Technology,
to be defended publicly on Tuesday October 31, 2017 at 14:00h.

Student number: 4085531
Project duration: November 15, 2016 – October 31, 2017
Thesis committee: dr. ir. M.J.M. Hermans, TU Delft, supervisor
Ir. W.M. van den Brink, NLR/NOP
dr. M. Janssen, TU Delft
PhD. M.A. Bessa, TU Delft

An electronic version of this thesis is available at <http://repository.tudelft.nl/>.

Acknowledgements

*F. van der Klift
MSc. Student
Material Science and Engineering
Delft, Date 2017*

Since it is the 21st century, basically everyone is connected to everyone and I can't even begin listing all the people that have supported me in whatever way possible. But there are of course some people who have helped me in such a way that without their help this thesis would not have turned out the way it has. I would like to dedicate my thanks to those who have helped me, but special thanks to the ones named below.

First of all I want to thank dr. M.J.M. Hermans from the Delft university of technology and Ir. W.M. van den Brink from the Dutch Aerospace Center for supervising and assisting me during these nine months of research. I also want to thank the Dutch Aerospace Center in general for allowing me to perform research at their facilities.

Furthermore I want to thank prof. A. Todoroki from the Tokyo Institute of Technology in Tokyo Japan for allowing me to use the Eiger[®] software that came with the MarkForged[®] 3D printers, that his lab owns. Without the access to this software I could not have been able to see how the prints were going to turn out before actually printing. This way I could perform simulations and calculations without actually printing first.

I also want to thank Mr. J. Docter from the NLR/NOP in helping me with obtaining ASTM and ISO standards for the mechanical testing. I want to thank Mr. G. Bos and Mr. F. Hoekstra for helping me with performing the mechanical tests in the labs of the Dutch Aerospace Center. Furthermore I would like to thank Mr. M. van der Kroeg and Mr. R Veenstra for assisting me in preparing the coupons for microscopic inspection. From the Delft university of technology I would like to thank Mr. S. van Asperen and Mr. W. de Goeij for aiding me in the usage of the SEM microscope. Moreover, special thanks to Mr. F. Shackman from Shackman's 3D printing hub for printing the parts helping me in any way possible with questions regarding the material and the printers.

Final thanks go to my mom and sister, for coping with me during this time and supporting me in any way possible. Thank you all very much.

Abstract

In order to save weight and reduce the impact on the environment, the aerospace industry keeps searching for strong and lightweight materials to reduce fuel consumption. A relatively new manufacturing technique made it possible to print nylon, reinforced with continuous unidirectional carbon fibres on a layer-by-layer basis and praised itself for making materials as strong as Aluminium 6061-T6. In this study, several coupons were 3D printed and tested in tensile, compression and three point bending mode to determine the material properties. When loaded in the direction of the fibres, the material did not live up to the upper limit of the rule of mixtures for fibre reinforced composites, which is mainly due to the amount of voids in the material. These voids were discovered when studying the micro-structure of the material and were both in between the layers, as well as in the layers themselves.

The mechanical tests were performed to validate constructed finite element models, simulated in Abaqus/CAE. The simulation results showed some mismatches with the mechanical test results, which were caused by the assumptions made to simplify the models. Finally, an air plane chair bracket, which has as task to transfer loads from the back seat panel to the chair, was modelled, simulated and designed. Major issues in the designing process were the limitations of the printer, such as not being able to choose which exact areas to reinforce in a specific layer. The final design of the chair bracket was manufactured and was tested to see if it could withstand a load of 375 N. The part did not fracture under the load, but a high displacement of the back seat was observed, as well as damage occurring at other locations than the simulations indicated.

The study showed that this 3D printing technique is able to print structural aerospace parts, given that the part is not too complex and that it is loaded in a static nature. More freedom in the design software of the 3D printer could allow the user to successfully design more complex structural aerospace parts. Since the constructed parts were only tested under static loading, further research has to be conducted into dynamic loading of these parts before it is possible to actually implement these in air planes.

*F. van der Klift
MSc. Student
Material Science and Engineering
Delft, October 2017*

List of Figures

1.1	Schematic drawing of the Selective Laser Sintering (SLS) process. A powder is sintered by a laser to form a 3D object. ^[1]	3
1.2	Schematic drawing of the Laminated Object Modelling (LOM) process. A laser cuts out the cross-section from sheets, which are then deposited and adhered by a roller. ^[2]	4
1.3	Overview of the Three Dimensional Printing (3DP) technology. An inkjet print head deposits a liquid binder onto each layer of powder individually to build a 3D part. ^[3]	5
1.4	Example of the stereolithography (SL) process. A UV-laser is used to trace the cross-section of each layer into a liquid bath of photosensitive polymer in order to fabricate a 3D object. ^[4]	6
1.5	Schematic overview of the Fused Deposition Modelling (FDM) process. A print head with two nozzles, one for build material and one for support material, deposits material layer by layer on a build platform ^[5]	6
1.6	The materials used for the fuselage of a Boeing 787. ^[6]	7
2.1	Schematic overview on how the material is deposited in FDM processes. It can be observed that voids can occur in between the deposited strips.	12
2.2	The Mark One [®] 3D printer by MarkForged [®] . The black case on the left is the container for the nylon matrix material.	14
2.3	The spools with fibre filament used by the Mark One [®] . From left to right: Glass Fibre, Carbon Fibre, Aramid [®] Fibre. Each spool contains 50 cm^3 of fibre filament	16
2.4	Schematic overview of the nylon and fibre feeding systems of the MarkForged [®] 3D printers. Note that the red area in the print head indicates the area that is heated.	16
2.5	Top view of the Mark One [®] . In this image both the nylon and fibre extruder (red) can be seen as well as the top of the print head (red). The transporting tubes are not fully visible, but have been traced with a green line.	17
2.6	Top-angled view of the Mark One [®] showing the servo motors.	18
2.7	Screen shot of the Eiger [®] software program. Different aspects of the interface are highlighted.	19
2.8	2D image of one of the layers the sample shown in fig.2.7 from the Eiger [®] software program. The blue lines indicate the carbon fibres.	19
2.9	Standard settings in the Eiger [®] software program.	20

2.10	Concentric fibre placement as shown by the Eiger [®] software. The yellow lines show the orientation of the fibre filament. The white lines are the wall layers.	21
2.11	Isotropic fibre placement as shown by the Eiger [®] software. The yellow lines show the orientation of the fibre filament. The white lines are the wall layers.	22
2.12	Square sample with isotropic fibre fill and 10 concentric fibre rings. The fibre filament is shown in blue. It can be seen that the concentric rings reinforce the walls, the isotropic fibre filament is placed inside the area surrounded by the concentric rings.	22
2.13	Advanced settings in the Eiger [®] software program.	23
2.14	Hinge sample created in Eiger [®] . The black lines are the wall layers, the yellow lines are the carbon fibre filaments. The red triangles in the center of the part are made of nylon and represent the triangular fill pattern.	24
2.15	Triangular filled components showing different percentages of fill density. Minimum fill density (0 %), 50 % fill density and Maximum fill density (100 %).	25
2.16	Stages of the printing process. a) After printing 2 carbon fibre concentric rings. b) After printing 4 concentric rings. c) After 8 concentric rings d) Completed layer.	25
2.17	Finished test sample used to test the 3D printer. An occurring discontinuity is encircled in red.	26
3.1	A completed sample by the Mark Two [®] . The fibre bundles are placed concentric so that these are unidirectional in the long parts of the sample.	30
3.2	Schematic drawing of where the printed sample would be sawed.	31
3.3	Sample after being ground and polished up to 1 μm	31
3.4	Sketch of the cross-section of an ASTM D3039-14 sample printed by the Mark One [®] . The different areas represent different types of layers, these are: floor layers (yellow), ceiling layers (grey), wall layers (red) and CF reinforced layers (green).	32
3.5	Initial test set-up of the ASTM D3039-14 tensile tests on the Instron [®] 5900R tensile test machine. The coupon is placed between the two clamps and an extensometer was applied.	35
3.6	The test set-up of the compression test EN2850. The sample is encircled in red and is clamped in between the two hydraulic presses.	35
3.7	Initial test set-up of the ASTM D790-03 three point bending tests.	36
4.1	Picture taken by the HiROX [®] digital microscope KH-1300 at 700x magnification. A single bundle of MarkForged [®] Carbon Fibre Filament is shown. The white circular dots are the carbon fibres.	39
4.2	3D image obtained by a Keyence VHX-100 microscope. The small particles on the fibre bundle are dust particles.	39

4.3	Graph showing the elemental counts vs KeV measured by backscatter electrons in the SEM. Only the resin material in the carbon fibre bundle was measured.	40
4.4	Stress-strain graph of the tensile test coupons T1 till T5. The circle indicates the point of failure. It can be observed that the failure is sudden and brittle.	41
4.5	Failed tensile test coupon after being loaded in tensile. The specimen failed with a lateral crack at the top grip (LAT). The dents in the nylon at the end are due to the hydraulic pressure of the clamps.	41
4.6	Stress-strain graph created with the data from the bending test coupons.	42
4.7	Compressive coupon after testing. The failure area is visible and failure starts from the edges and moved inwards.	43
4.8	Stress-strain graph created with the data from the bending test coupons. The jumps in the cyan line of the B5 coupon was caused by the jumping away of the lower support rollers.	44
4.9	All five bending coupons after their respective tests. It can be observed that not all samples failed at the same point, as indicated by the kink angles in the samples.	44
4.10	Complete image of the T1 tensile test coupon taken in the x-z plane.	45
4.11	Tensile test coupons after failure. Besides the main tensile failures, other compressive failures were observed at the opposite end of the samples.	45
4.12	The tensile failure area of the T1 tensile test coupon.	46
4.13	One of the many voids in the T1 tensile test coupon. It can be seen that this void is in between two layers and spans into the y-direction.	46
4.14	Failure of the compressive specimen in the x-y plane. The left kinked area is shown in green, the right kinked area in red.	48
4.15	Microscopic view of a compression test coupon in the x-y plane. The green circle indicated the location of fig. 4.16.	49
4.16	Zoomed in view of the failed area in the x-y plane. It can be seen that the fibres kinked into one single direction and finally breaking.	49
4.17	Microscopic image of the B1 three point bending test coupon.	50
4.18	Failed area of the B1 sample - zoomed in view.	50
5.1	comparison of computation time for specific elements in abaqus [®] . ^[7]	54
5.2	Stress-strain curve of a nylon coupon tested in tensile. ^[8] The inconsistencies in the curve can be ignored and are related to the machine malfunctioning.	57
5.3	Three models with different mesh sizes. a) 4 mm per mesh element, b) 2 mm per mesh element, and c) 1 mm per mesh element.	57
5.4	Sketch of the cross-section of a modelled coupon. The different areas represent different types of layers, these are: nylon (red) and carbon fibre reinforced (green).	59

5.5	Simulation results of the tensile coupon in abaqus [®] . The maximum stresses observed are 625 <i>MPa</i>	60
5.6	Simulation result of the compression coupon in abaqus [®] , showing a maximum compressive stress of 122 <i>MPa</i>	60
5.7	Simulation result of the bending coupon in abaqus [®] . Maximum stress observed was a tensile stress of 370 <i>MPa</i>	61
6.1	Abaqus model of nylon torque link as designed by the NLR ^[9] . Figure a shows the unloaded state, figure b shows the stresses when an upward load is placed on the hole on the right. The brighter yellow the colour, the higher the stresses.	64
6.2	The NLR torque link model ^[9] consisting of two components. Fig. a shows the bottom part, fig. b shows the top part.	64
6.3	a) The chair bracket design made in Abaqus. The back frame is attached to the two small holes. The other holes are for fixing the chair bracket to the rest of the chair. b) shows the same part in the Eiger [®] software with the fibres in blue.	65
6.4	Abaqus simulation result of the original chair bracket design tested with a 750 N load per bracket applied to the top of the back panel of the seat. It can be seen that especially the compressive load is a factor 3 too high.	66
6.5	Abaqus simulation result of a primitive model showing where the stresses are located. The highest tensile and compressive stresses are located in the outer reinforced ring.	66
6.6	Design 2 of the composite chair link. The dimensions are still the same, but the geometry has changed. The minimum stress is reduced to -162.8 <i>MPa</i> , but the costs went up to 400 Euro.	67
6.7	Design 3 decreased the costs to 360 Euro but the compressive load rose to -158 <i>MPa</i>	68
6.8	With the third redesign, the compressive load dropped to -145.9 <i>MPa</i> The costs however, were 340 Euro.	68
6.9	Final part as printed by the Mark Two [®] . It can be seen that the bottom 30 and top 30 layers are reinforced. The costs of this part are 248 Euro.	69
6.10	Test set-up for testing the 3D printed chair bracket. The bracket is mounted to a steel plate by two bolts. The metal part at the end of the arm is used to hang the load on.	70
6.11	Complete test set-up. The weights can be stacked on the pendulum in order to increase the load on the bracket. A wooden board is placed under the pendulum to prevent any damage to the floor in case of failure.	70
6.12	Final stage of the test. (a) A total load of 37.5 <i>kg</i> hanging from the pendulum. (b) The bracket under a load of 375 <i>N</i> . The arm is no longer in a straight position.	71
6.13	3D printed chair bracket after testing. The bracket is still attached to the steel plate, but the damage to the pin holes (encircled in red) is clearly visible.	71

7.1	Part designed that needs to have only the outer walls and the holes for the pin connections to be reinforced. Sadly Eiger® will also reinforce the other gap, which was created in order to save material, weight, and costs.	74
7.2	The tensile modulus versus temperature of a semi-crystalline polymer. ^[10] . .	76
A1.1	Individual stress-strain graph of the T1 coupon	88
A1.2	Individual stress-strain graph of the T2 coupon	89
A1.3	Individual stress-strain graph of the T3 coupon	89
A1.4	Individual stress-strain graph of the T4 coupon	90
A1.5	Individual stress-strain graph of the T5 coupon	90
A2.1	Individual stress-strain graph of the C1 coupon	91
A2.2	Individual stress-strain graph of the C2 coupon	92
A2.3	Individual stress-strain graph of the C3 coupon	92
A2.4	Individual stress-strain graph of the C4 coupon	93
A2.5	Individual stress-strain graph of the C5 coupon	93
A3.1	Individual stress-strain graph of the B2 coupon	94
A3.2	Individual stress-strain graph of the B3 coupon	95
A3.3	Individual stress-strain graph of the B4 coupon	95
A3.4	Individual stress-strain graph of the B5 coupon	96

List of Tables

2.1	Advantages and disadvantages of the FDM based 3D printing as of 2008. ^[11]	13
2.2	Selected mechanical properties of the matrix materials used by the MarkForged [®] 3D printers ^[12]	15
2.3	Information on mechanical properties of fibre reinforced nylon composite specimens ^[12]	15
3.1	Geometrical and volumetric data of ASTM D3039-14 sample given by the Eiger [®] software	32
3.2	Values of parameters used in eqs. 3.2 - 3.5	33
3.3	Comparison between the dimensions of a design and the dimensions considering thermal effects.	34
4.1	Elemental composition of fibre bundle resin material.	39
4.2	Dimensions and mechanical test results of the tensile test coupons.	40
4.3	Average width and thickness of the compression coupons, together with the measured test results.	42
4.4	Dimensions of the bending test coupons. The test values of the B1 coupon are missing due to incorrect test settings.	43
4.5	Comparison between tensile test data on carbon fibre reinforced composite material supplied by the MarkForged [®] company ^[12] and the tensile test data obtained in this study.	47
5.1	Carbon fibre material values used as input for abaqus [®] simulations.	59
5.2	Comparison between mechanical and simulation results.	61
7.1	Comparison between material properties of Aluminium 6061-T6 and the printed composite material	78
7.2	Comparison between the mechanical properties of nylon ^[12] and the 14.15% carbon fibre reinforced nylon.	78
7.3	Comparison between the mechanical properties of 6CF specimens ^[8] and the 14.15% carbon fibre reinforced tensile test coupons.	79

List of Symbols

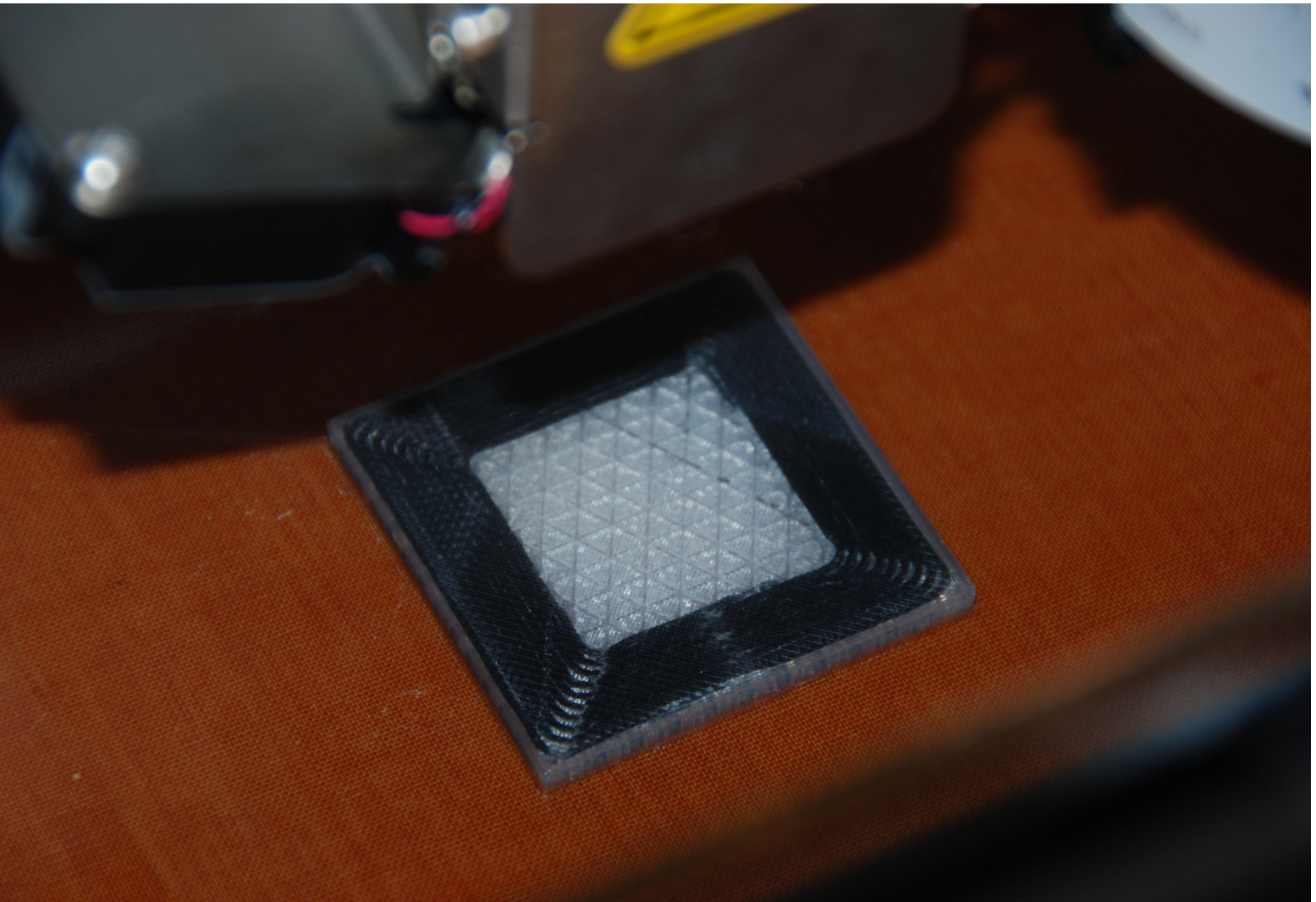
$n_{concentric}$	=	Number of concentric fibre rings
n_{fc}	=	Number of floor/ceiling layers
n_{fibre}	=	Number of fibre reinforced layers
$n_{wall-layer}$	=	Number of wall layers per wall
t	=	Thickness in mm
t_{layer}	=	Thickness of one printed layer in mm
E	=	Young's Modulus in GPa
E_f	=	Young's Modulus of the fibres in GPa
E_m	=	Young's Modulus of the matrix material in GPa
G	=	Shear Modulus in GPa
L	=	Length in mm
T_g	=	Glass transition Temperature in $^{\circ}C$
T_m	=	Melting Temperature in $^{\circ}C$
V_{FC}	=	Total volume of floor or ceiling layers in a printed sample
V_f	=	Fibre Volume Fraction
V_{fibres}	=	Total volume occupied by fibres in mm^3
V_{total}	=	Total Volume of sample in mm^3
$V_{wall-layer}$	=	Total volume of wall layers in a printed layer in mm^3
W	=	Width in mm
W_{fibres}	=	Width of one printed fibre bundle in mm
W_{swl}	=	Width of a single wall layer in mm
ϵ	=	Engineering strain in mm/mm
ϵ_0	=	True strain in mm/mm
σ	=	Engineering stress in MPa
σ_0	=	True stress in MPa

Contents

Acknowledgements	iii
Abstract	v
List of Figures	vii
List of Tables	xiii
List of Symbols	xv
1 Introduction	1
1.1 Background Information	2
1.1.1 Types of AM processes	2
1.1.2 AM processes for continuous fibre reinforced polymers	7
1.2 Scope and research question	9
1.2.1 Outline of thesis report	10
2 The Printing Process	11
2.1 Fused Deposition Modelling based 3D Printing	12
2.2 The Mark Two [®] 3D Printer	13
2.2.1 Comparing the printers	13
2.2.2 Material supply to the print head	14
2.3 The Eiger [®] software	18
2.3.1 Selection of printer parameters in Eiger [®]	20
2.4 Determining printing process via test print	24
2.5 Printer limitations	26
3 Mechanical Test Samples and Test Set-ups	29
3.1 Printer settings	30
3.2 The Samples	30
3.3 Geometrical calculations on the samples	32
3.4 Mechanical tests	34
4 Results and Discussion	37
4.1 Initial results	38
4.2 Fibre bundle inspection	38
4.3 Tensile test results	40
4.4 Compression test results	41
4.5 Three point bending test results	42
4.6 Discussion of results and microscopic images	44
4.6.1 Tensile test discussion	44

4.6.2	Compression test discussion	47
4.6.3	Bending test discussion	50
5	The Abaqus/CAE® Models	53
5.1	The Abaqus® environment	53
5.1.1	Creating parts	54
5.1.2	Supplying material data	55
5.1.3	Creating assembly and assigning interactions	55
5.1.4	Define steps, boundary conditions and loads	55
5.1.5	Assigning a mesh and creating the job	56
5.2	The nylon sample	57
5.3	Simulating the coupons	58
6	Designing the aircraft part	63
6.1	Designing aircraft parts	63
6.1.1	The Torque Link	64
6.1.2	The Chair bracket	65
6.1.3	Other designs for the Chair	67
6.2	Testing the chair part	69
7	Discussion	73
7.1	The printer	73
7.2	Models	76
7.3	Comparison of materials	77
7.3.1	Aluminium 6061-T6	77
7.3.2	Polyamide-6	78
7.3.3	comparing to previous research	79
7.4	The chair part	80
8	Conclusion	81
	Bibliography	82
	Appendix A1	88
	Individual Tensile Test Graphs	88
	Appendix A2	91
	Individual Bending Test Graphs	91
	Appendix A3	94
	Individual Bending Test Graphs	94
	Appendix B	97
	Fibre bundle tests	97

Introduction



A composite is a material, consisting of two or more different materials processed to form a single material. This resulting composite material, has mechanical, chemical, optical, and/or electrical properties that differ from the base materials. In this way a material with unique combination of properties can be obtained.

Composite materials have been around for a long time. The earliest record being in 3400 B.C. in ancient Mesopotamia,^[13] where wooden strips were used to create plywood. This composite was the first recorded to be used for structural applications.

Nowadays research is performed on many different types composites, consisting of different materials. This study focuses on the carbon fibre reinforced polymers. In this case the matrix material is a polymer, which is strengthened by using carbon fibres to enhance its mechanical properties. The composite material will be manufactured through additive manufacturing (AM), which is a technique that is build around building a part layer by layer.

1.1. Background Information

Even though composites have been used for almost 5500 years, it was not until the introduction of rapid prototyping and manufacturing (RP&M) techniques that the industry could produce high strength, light weight composite materials, like carbon fibre reinforced thermo polymers, more efficiently. Yan and Gu^[14] stated that, before RP&M, the industry would benefit from reducing the production time and flexibility of batch size products. However, a gap between computer aided design (CAD) and actual production of parts still existed.

Additive manufacturing (AM) has the ability to create a product directly from a Three Dimensional CAD drawing. AM has been described by the ASTM to be: "the process of joining materials to make objects from 3D model data, usually layer upon layer".^[15] One of the main advantages of AM over conventional production techniques is that AM does not require any tools, fixtures and coolants.^[16] Up to date, AM has many applications in many different fields e.g. healthcare^[16–19], civil engineering and architecture.^[20, 21]

1.1.1. Types of AM processes

Many types of AM processes exist, but these all operate in the same basic principle. First a digital drawing in 3D of the desired object has to be created. For the computer aided design (CAD) numerous software packages are available, e.g. SolidWorks[®], Abaqus/CAE[®] or Catia[®]. The CAD image is stored as an .stl-file. The .stl-file was designed by 3D Systems Inc. in 1987 to aid the Stereolithography technology and 'stl' stands for Standard Tessellation Language.^[22] The subsequent preparation step is the slicing of the 3D CAD image into layers. Nowadays the .stl-file extension is the standard format for any AM machine. Once the .stl-file is created, it is send to the AM-machine, which will build the part.^[16]

There are many different types of AM processes available and each of these works in a different way and with different materials. Some of the most used AM processes are: Selective Laser Sintering (SLS)^[1, 14, 23–33], Laminated Object Manufacturing (LOM)^[2, 14, 16, 23, 31, 34–36], Three Dimensional Printing (3DP)^[3, 14, 16, 23, 34, 35, 37, 38], Stereolithography (SL)^[4, 14, 16, 22, 23, 34, 35, 39], and Fused Deposition Modelling (FDM).^[5, 14, 16, 23, 34, 35, 40–44] All of these technologies will be briefly described in the following sections.

Selective Laser Sintering

Selective Laser Sintering (SLS) is the process of binding powder material together by means of a laser^[14]. The powder is brought to an elevated temperature, just below the melting point. The laser then supplies the final amount of heat to sinter the powder to form a solid part. The powder is not melted by the laser, since sintering is the process of forming a solid mass of material by means of heat, without liquifying the material first. After a layer is completed, the bed drops and a new layer of powder is deposited from the powder supply. This way a 3D product can be created by sintering layer by layer. The advantage over many other powder based processes is that SLS does not need a binder material^[23]. A schematic drawing of the machine is shown in fig. 1.1^[1]

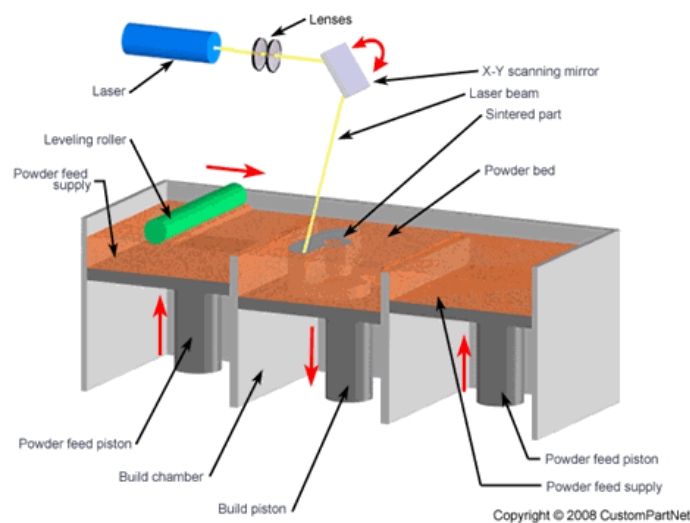


Figure 1.1: Schematic drawing of the Selective Laser Sintering (SLS) process. A powder is sintered by a laser to form a 3D object.^[1].

In terms of materials, any material that is in powder form and can be sintered by a laser can be used. In case of SLS, materials are usually polymers, glasses or ceramics. When using metals, the name of the process is referred to as Direct Metal Laser Sintering (DMLS)^[24]. Traditionally, SLS parts were made with just one type of powder, but powder mixtures are nowadays also possible as described by Simchi *et al.*^[25]. However, with SLS processes, parts without voids are almost never achieved due to the porosity of the sintered parts^[25, 26]. This happens a lot when there is just one type of powder that is being sintered. When two powders are sintered, the technique is referred to as liquid phase sintering (LPS). One powder has a high melting point, the other a low melting point. The laser sinters the powders with the high melting point. The other powder melt and will fill the pores.

One of the drawbacks of SLS processes is that the parts created have limited mechanical properties. The types of materials that can be used with SLS are for example: Nickel Alloys^[27], PEEK^[28], SiC/Polyamide Composites^[29], Nylon^[30], Fe-Cu and WC-Co powder mixtures^[26], Aluminum^[31], Titanium^[32] and various Cu alloys, including bronze.^[33] It is, however, not possible to create composites with continuous fibres as reinforcement. Because of this, this technique will not be used in this research.

Laminated Object Modelling

Laminated object modelling (LOM) makes use of thin sheets of material to build a 3D part. The sheet is spanned between 2 rolls, with 2 additional rolls for support. A laser cuts out the desired cross-section, which is deposited on a print bed. The deposited layers are then adhered by hot rolling. The layers of material have been pre-treated with an adhesive to make adhering possible. A schematic drawing of the LOM process can be seen in fig. 1.2

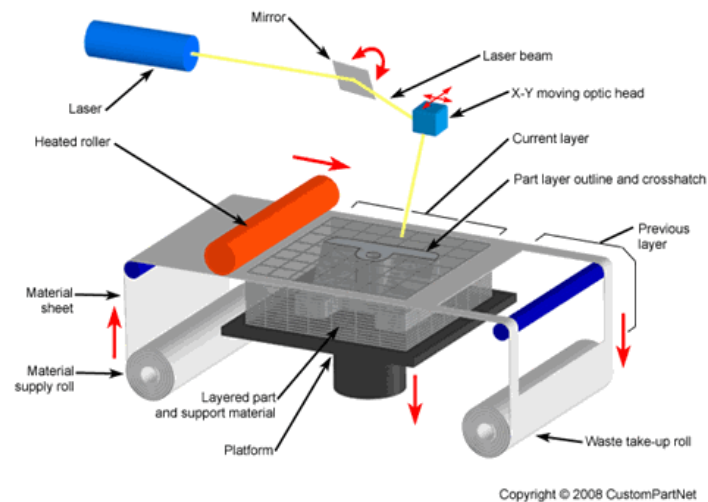


Figure 1.2: Schematic drawing of the Laminated Object Modelling (LOM) process. A laser cuts out the cross-section from sheets, which are then deposited and adhered by a roller.^[2]

The laser that cuts the material has been calibrated so that it only cuts one layer thickness and does not damage the part below. Usually, a CO_2 laser with a power of 25 to 50 W is applied.^[23]

One of the main advantages of LOM is the speed of the process. Only the outlinings have to be cut by the laser, which makes the process faster than other AM processes.^[36]

Another advantage of LOM is the wide range of materials that can be used. By means of laser cutting, materials like metals, ceramics or even prefabricated composites can be used by LOM. However, if another cutting technology like knife cutting or heated wire cutting is used, the range of material can be even broader and the LOM processes is able to also create parts out of paper, polymers and polymer foam sheets^[35].

Some of the challenges for LOM are that the materials should have a minimum tensile strength in order to be spanned between the rolls and increase the accuracy of the cutting process.^[31] Even though LOM is capable of creating parts with continuous fibre reinforcements, the base material already must contain these reinforcements, which means expensive base material has to be used. For this reason this technology will also not be used in this research.

Three Dimensional Printing

Three Dimensional printing involves the curing of powder by using a liquid binder^[37]. A print head deposits the liquid binder onto the powder, which solidifies almost instantaneously. A schematic drawing of the 3DP process can be seen in fig.1.3

As can be seen from fig. 1.3, 3DP machines have two different platforms. One for building the part, the other for supplying the powder. Before starting, the feed piston is raised, and a

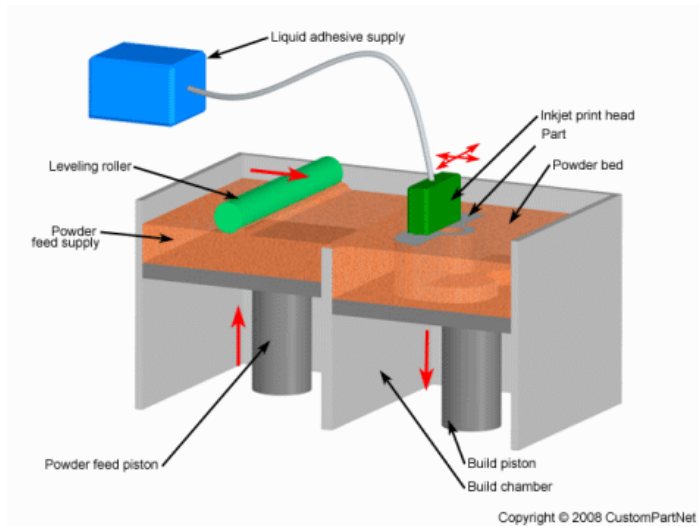


Figure 1.3: Overview of the Three Dimensional Printing (3DP) technology. An inkjet print head deposits a liquid binder onto each layer of powder individually to build a 3D part.^[3]

roller distributes a layer of powder on build tray. A print head will deposit the liquid binder to create a solid section. Once a layer is completed, the print head moves out of the way. The build piston lowers, while the feed piston elevates. A roller distributes the next layer of powder onto the build tray and the next layer can be build.

The advantages of 3D printing are that it is a very fast fabrication technique and it has relatively low material costs.^[38] A disadvantage is that the resolution in the z-direction, which is more commonly known as the layer thickness, is $500\mu\text{m}$, which is quite high.^[23] However, because this technology is powder based, it is impossible to create continuous fibre reinforced composites, and thus this technique will not be implemented for this research.

Stereolithography

Stereolithography was the first of the AM processes, invented by 3D Systems Inc.^[22] The SL process uses a liquid polymer that solidifies when coming in contact with UV-light. By deploying a UV-laser a cross-section of the desired product can be solidified into the liquid polymer. A schematic drawing of this process can be seen in fig.1.4.

SL is limited in its use of materials, since the process is dependent on materials that are liquid at room temperature and only will solidify if locally exposed to UV. Furthermore, Pham *et al.*^[39] distinguished three types of errors for SL. These are tessellation errors, curing errors and control errors. The tessellation error will be present in all AM processes, and is due to approximating the area of each layer by making use of triangles. These triangles will not always fit inside the area, thus over- or underestimating it. By increasing the number of triangles (or by decreasing the size of the triangles) the tessellation error becomes smaller, however this require more computing power.

The curing errors are caused by over-curing the material of a layer so that it adheres to the previous layers. Over-curing means that more heat is supplied to the layer than needed, so that the material bonds easier to previous layers. However, the bottom layer does not have to adhere, but still is over-cured and will deform due to this.

The control errors are referring to controlling the layer thickness, which will vary if these errors are present and this will deform the part.

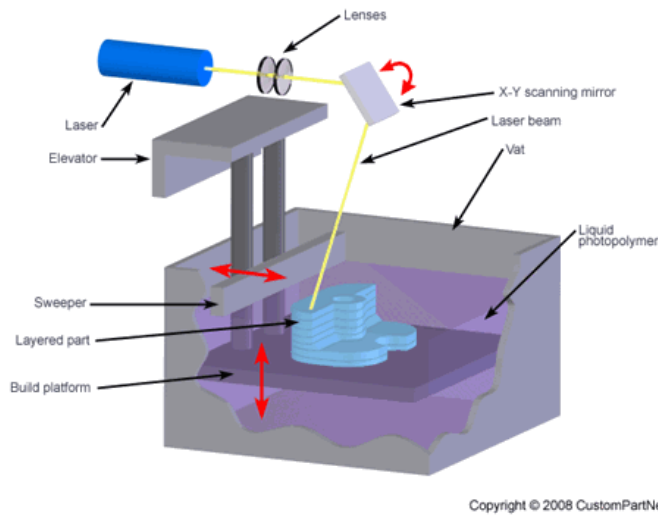


Figure 1.4: Example of the stereolithography (SL) process. A UV-laser is used to trace the cross-section of each layer into a liquid bath of photosensitive polymer in order to fabricate a 3D object.^[4]

All in all this technique is not capable of printing composites with continuous fibres as reinforcement and thus will not be made use of in this research.

Fused Deposition Modelling

FDM was introduced by Stratasys[®]^[40]. Controversial to SLS, the material is heated to just above the melting temperature. Once melted, the material is deposited on a bed where it solidifies within a time of approximately 0.1 seconds, adhering to subsequent layers. A schematic overview of the process is shown in fig. 1.5^[5]

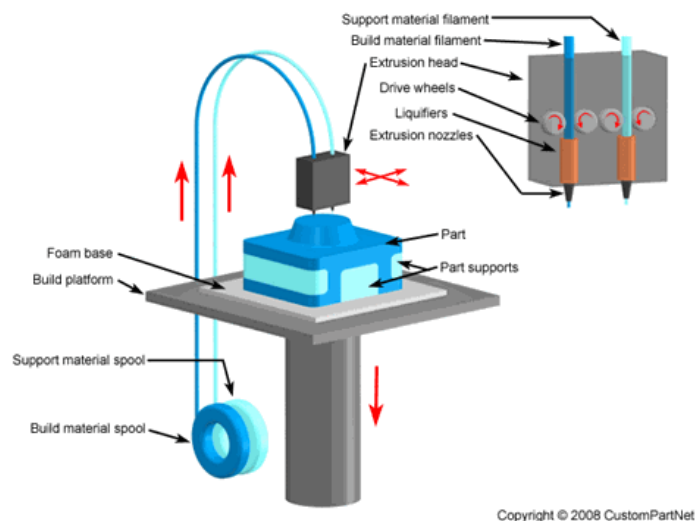


Figure 1.5: Schematic overview of the Fused Deposition Modelling (FDM) process. A print head with two nozzles, one for build material and one for support material, deposits material layer by layer on a build platform^[5].

FDM is usually applied to materials like ABS, PLA, Nylon, elastomers and wax^[35]. Kumar *et al.*^[34] also reported usage of Iron-Nylon composites, Aluminium, Alumina and ceramics. Advantages of FDM are the high part build speed, due to a high speed motion control

system^[41]. Another advantage is that the FDM print head has two separate nozzles. One nozzle deposits the part material, whereas the other nozzle deposits support material, usually a wax.^[42] However one of the drawbacks of FDM is the lower accuracy, as described by Boschetto *et al.*^[43]. Another disadvantage is the adhering between the different layers, which is not uniform. Also the delamination caused by the temperature changes.^[16, 44] An advantage is that one of the nozzles can be used to print continuous fibres, which makes this technique suitable for this research. This technique, as well as the machine used, will be explained in more detail in chapter 2.

1.1.2. AM processes for continuous fibre reinforced polymers

Nearly 90 % of the sold AM machines were 3D printers for making polymer based parts.^[45] This is because of several reasons, one of which is the low cost of desktop 3D printers^[46]. Besides the low initial costs, 3D printing is also a more and more upcoming production technique in the industry due to the low amounts of waste material and fast production times.^[46] Nowadays, 3D printers can make object of almost all complex shapes and sizes.^[47] Please note that the term "3D printer" here does not refer to the 3DP AM technology specifically, but this terminology is used to refer to any Three Dimensional part building AM machine. This is rather confusing and the division between AM and 3D printing is very slim and purely depends on how the technology is used. From now on the term "3D Printing" will be used instead of additive manufacturing throughout this report.

Over the last few years, the 3D printing technology has been going into the direction of printing fibre reinforced polymers (FRP). Carbon fibre reinforced polymers (CFRP) were already used for aerospace applications since the discovery of the carbon fibre in 1964. However, the automotive and aerospace industries, became more interested in these materials for weight-saving purposes. Furthermore, CFRP materials became attractive candidates for these industries because of their relatively high strength and low weight.^[48] Nowadays most of the fuselage of a Boeing 787 consists of some type of composite material as is shown in fig. 1.6^[6].

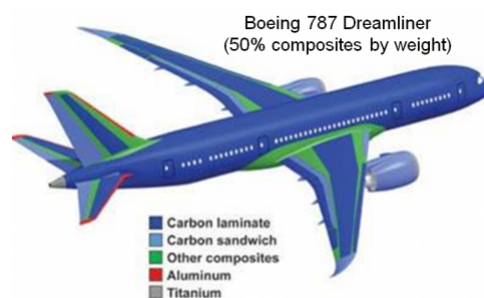


Figure 1.6: The materials used for the fuselage of a Boeing 787.^[6]

It should be noted that only the LOM, SL and FDM processes are capable of creating FRP composites. The LOM technology can only create composite parts if the base material consists of a sheet of composite material, whereas for SL and FDM the fibres can be added separately from the matrix material. Only FDM is capable of printing composites with continuous fibres.

Most of the studies on 3D printing CFRP are focussing on short fibres, constructed with various techniques, such as impregnation^[49], mixing and extruding^[50] and fused deposition modelling^[51]. Research on 3D printing polymer materials reinforced with unidirectional continuous fibres is not reported often in literature. This is surprising since unidirectionally aligned fibre composites can be used in the aerospace and automotive applications to replace parts that are loaded in tensile. A specific reason for this is that unidirectional CFRP, loaded in tensile, has a tensile modulus and tensile strength which are independent of the strain rate. Whereas the tensile strength and modulus in the transverse direction increase linearly with the strain rate.^[52] Moreover, unidirectional continuous fibres have superior mechanical properties compared to unidirectional chopped fibres.^[53]

There are also disadvantages to unidirectional FRP composites. One of these disadvantages, was pointed out by Okabe and Takeda.^[54] They showed that the composite strength decreases as the size of the samples increases, due to fibre cluster formation. Furthermore, Gamstedt and Talreja^[55] reported that fatigue damage in unidirectional CFRP was caused by a widespread de-bonding, where the fibres and matrix material would become de-attached from one another, thus lowering the mechanical properties of the composite material. The unidirectional CFRP, using a thermo-setting matrix, showed a higher fatigue resistance. However, this is purely depending on the matrix material used, since carbon fibres themselves are almost insensitive to fatigue.^[56]

Many of the properties of CFRP materials are, however, influenced by the production technique. This includes e.g. the data scattering, researched by Maekawa *et al.*^[57] They showed that the scatter of tensile strength in unidirectional CFRP laminates at room temperature can vary by 10.7%. The explanation for this was due to the fibres possibly not being fully unidirectional.

Most of the research done on FRP materials has not been performed on FRP materials made by FDM based 3D printing with continuous fibres. A recent paper by Namiki *et al.*^[58], reported on mechanical behaviour of a composite material created by a 3D printer based on fused deposition modelling. It was shown that the tensile modulus was roughly 10 % lower than theoretically estimated by the upper limit of the rule of mixture. This discrepancy was explained by voids between the filament layers and fibres not being fully embedded in the matrix material. Matsuzaki *et al.*^[59] created a FDM based 3D printer with in-nozzle impregnation. Here the fibres and matrix material are mixed within the nozzle itself, just before being extruded to the print bed.

In a previous article from the author^[8] CFRP samples with continuous fibres were printed and tested in tensile by using an FDM based 3D printer called the Mark One[®]. This printer extrudes both materials separately, and the matrix and fibres mix on the print bed. It was shown that the samples did not live up to the rule of mixture for fibre dominated properties of composites. The rule of mixtures calculates the Young's modulus of a fibre reinforced composites, by using the young's modulus of the fibres and the matrix, as well as volume fraction of fibres used in the composite. The formula for the rule of mixture is shown in eq.

1.1

$$E = E_f * V_f + E_m * (1 - V_f) \quad (1.1)$$

, here E is the Young's Modulus of the composite in the fibre direction, E_f and E_m are the Young's moduli of the fibres and matrix material respectively, and V_f is the fibre volume fraction in the composite. The main reason for the samples not living up to this rule of mixtures was the presence of voids in the samples.

In a recent paper, Malenka *et al.*^[60] also tested the Mark One[®] with Aramid[®] fibres to evaluate and predict the tensile properties of samples with different fibre filament volume fractions, ranging from a few percent to just over 10 % as a maximum. It was found here that the addition of fibres increases the tensile strength and tensile modulus of the specimens. The higher the fibre filament volume fraction, the better the predictions were.

1.2. Scope and research question

This thesis research focusses on the continuous fibre reinforced composite material created through FDM based 3D printing. The composite material consists of a nylon matrix, with continuous unidirectional carbon fibres as reinforcements. For this the Mark Two[®] by MarkForged[®] was used. The composite material was already partially researched by van der Klift *et al.*^[8] and this research is a continuation of this paper, but with several improvements made:

- In the article^[8] the printed samples had some of their nylon ground off. This increased the volume percentage of carbon fibre material, but also increased the scatter due to inaccuracy in the dimensions. In the current research, the samples will not be ground to improve the accuracy of mechanical test results.
- The samples from the article^[8] were printed by the Mark One[®], but will now be printed by the Mark Two[®] which is considered to be an upgrade from the Mark One[®].

The main goal of this research is to understand the material properties and to see what the printer and the printed parts are capable of, with the main question being:

"Is the composite material with continuous carbon fibres printed by a FDM based 3D printer feasible for structural aerospace applications?"

Besides the main research question, other important questions that need answering are:

- How does the Mark Two[®] operate, how does the printing process work? What are the advantages and disadvantages? What are the limitations of the printing process and materials? How can this be improved?
- What are the mechanical properties of the parts created? Is there much scatter in the data? If so, what are the reasons? And what are the reasons the part failed this way?
- What does the microstructure look like? Are there any defects? How can these defects be explained?

- Can a structural aerospace part be designed and printed with the given printer and material? What are the design limiting factors if any? If it is not feasible to create a structural aerospace part, is this due to the material, the printer, or both?

1.2.1. Outline of thesis report

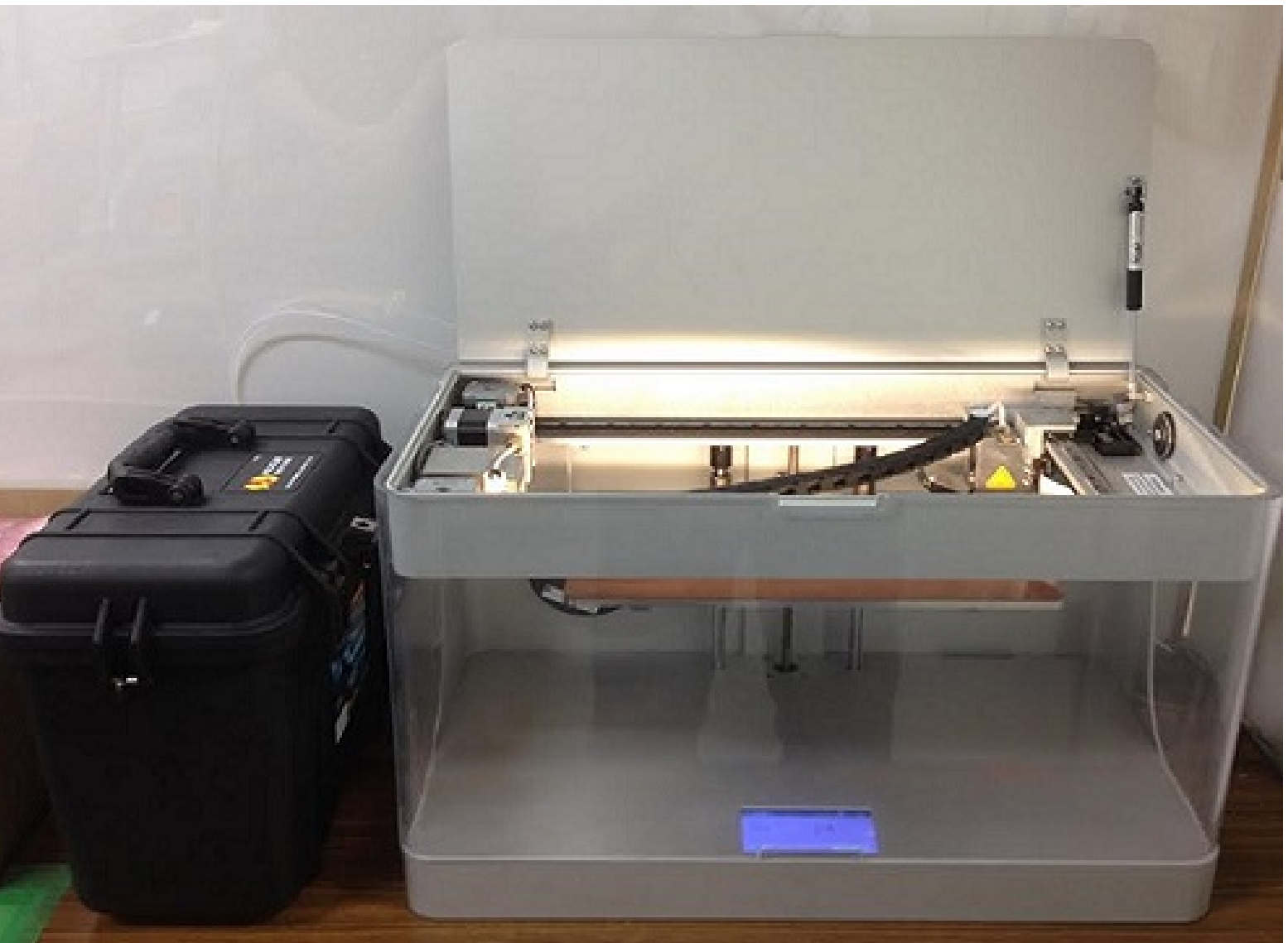
After this introduction (chapter 1), chapter 2 will explain the FDM process in more detail. Furthermore, the 3D printer and the complete printing process will also be described. Chapter 3 will be about the samples, their geometry and the preparation for the specific tests. The experiments performed on the coupons will also be explained here.

After this, chapter 4 will contain both the results of mechanical tests and of the microscopic characterisation. A discussion on the results of the mechanical tests will conclude this chapter.

Chapter 5 deals with the modelling of the coupons that were tested and the results of these models are compared to the experimental test data. Chapter 6 describes the demo part. The design, model, and printing of this part are presented. The test performed on this demo part will also be described in chapter 6. Finally, chapter 7 will provide the final discussion and chapter 8 provides the conclusions to this research.

2

The Printing Process



This chapter will give a short overview of FDM based 3D printing, after which the Mark One[®] and the Mark Two[®] 3D printers will be introduced by explaining the working principle and naming the core components of these printers. The software that is necessary for printing parts will also be explained. Finally, a square test sample was created to determine the limitations of the printers and their differences.

2.1. Fused Deposition Modelling based 3D Printing

Fused deposition modelling (FDM) is one of the most common techniques for making 3D polymer parts. Most used materials for FDM are Acrylonitrile Butadiene Styrene (ABS), Polylactic Acid (PLA), and Polycarbonate (PC), though all thermoplastic materials can be employed. The materials are supplied as filaments, wound on spools. The filament is guided through a tube towards the print head, where the filament is heated to just above the melting temperature. After being melted, the material is very viscous and can be deposited in small strips on the print bed, as is depicted in fig. 2.1. Usually the print bed is first treated with a glue or other substance to make sure the print can be easily removed from the print bed once the production is finished.

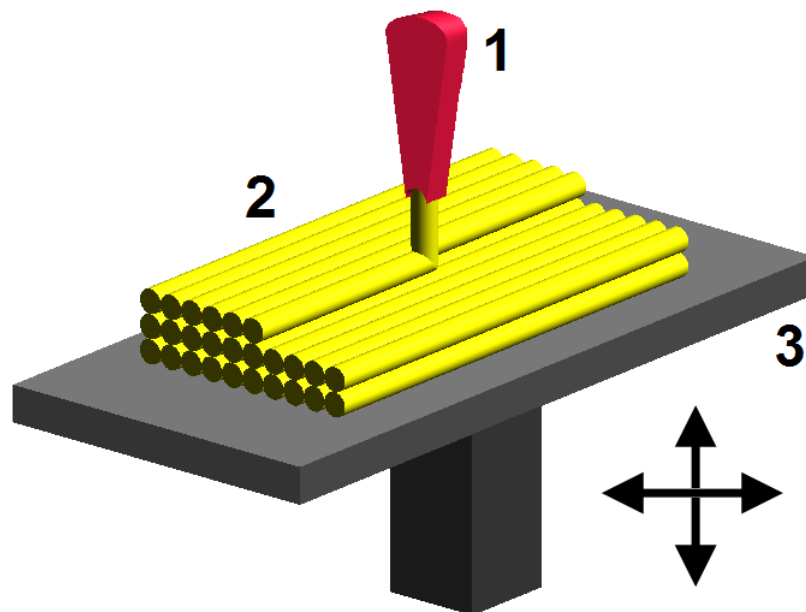


Figure 2.1: Schematic overview on how the material is deposited in FDM processes. It can be observed that voids can occur in between the deposited strips.

The print head can move in the x- and y-direction, whereas the print bed can only move in the z-direction. The print head will start depositing the first layer of material. Once the layer is completed, the print bed will move downwards and a second layer can be printed. This process will continue until the part is finished.

Important parameters for FDM are the printing temperature, print head velocity and the minimum step size of the print bed in the z-direction. The printing temperature is determined by the printed materials. If the maximum temperature is lower than the melting temperature of the material, that material is not suited for this specific FDM printer. The printing temperature in combination with the print head velocity are important for part quality. If the temperature is too high, the material might solidify too late, under- or over-sizing the part. When the print head velocity is too high, the deposition of material will become discontinuous, resulting in poorer mechanical properties and lower overall quality. When the velocity is too low the filament material might solidify in the print head nozzle,

causing it to clog.

The minimum step size of the print bed in the z-direction, determines the minimum layer thickness possible. The thinner the layers are, the higher the dimensional accuracy of the part is. The minimum step size is often referred to as the resolution of the printer.

When checking the literature on FDM, several other advantages and disadvantages to the FDM based 3D printing technology of polymers are described. These advantages and disadvantages are listed in table 2.1.

Table 2.1: Advantages and disadvantages of the FDM based 3D printing as of 2008.^[11]

FDM Advantages	FDM Disadvantages
A wide variety of materials available	Seam line between layers
Easy material change	The extrusion head must always continue moving, or else material bumps up
Low maintenance costs	Supports may be required
Thin parts produced fast	Part strength is weak perpendicular to build axis
Resolution of +/- 0.125 mm	More area in slices requires longer build times
No supervision required	Temperature fluctuations during production may lead to delamination
Very compact size machines	Very compact size machines

These characteristics are also valid for fibre reinforced polymers. Some of the disadvantages in table 2.1 can be avoided though post processing, e.g. the seam line between layers. This seam line is a visible line on the edge of a printed part, at the point where 2 layers adhere. This seam line can be ground away to improve the surface quality of the part. Other disadvantages, like the necessity of supports, can be avoided or reduced by selecting an optimal print orientation of the part. Future research, which is beyond the scope of this thesis, has to be conducted to try and reduce these disadvantages further.

2.2. The Mark Two[®] 3D Printer

In 2015 the company MarkForged[®] released a new type 3D printer, the Mark One[®], this printer is shown in fig. 2.2. This 3D printer was unique, because it was the first FDM based 3D printer able to print nylon products reinforced with continuous fibres. Due to the success of this printer, an improved printer, the Mark Two[®] was introduced in 2016.

2.2.1. Comparing the printers

The Mark One[®] 3D Printer is rather compact and can be used as a desktop printer. The maximum size of printed samples is 320 mm by 132 mm by 154 mm in length, width and height respectively. These dimensions are the same for the Mark Two[®]. As with all FDM

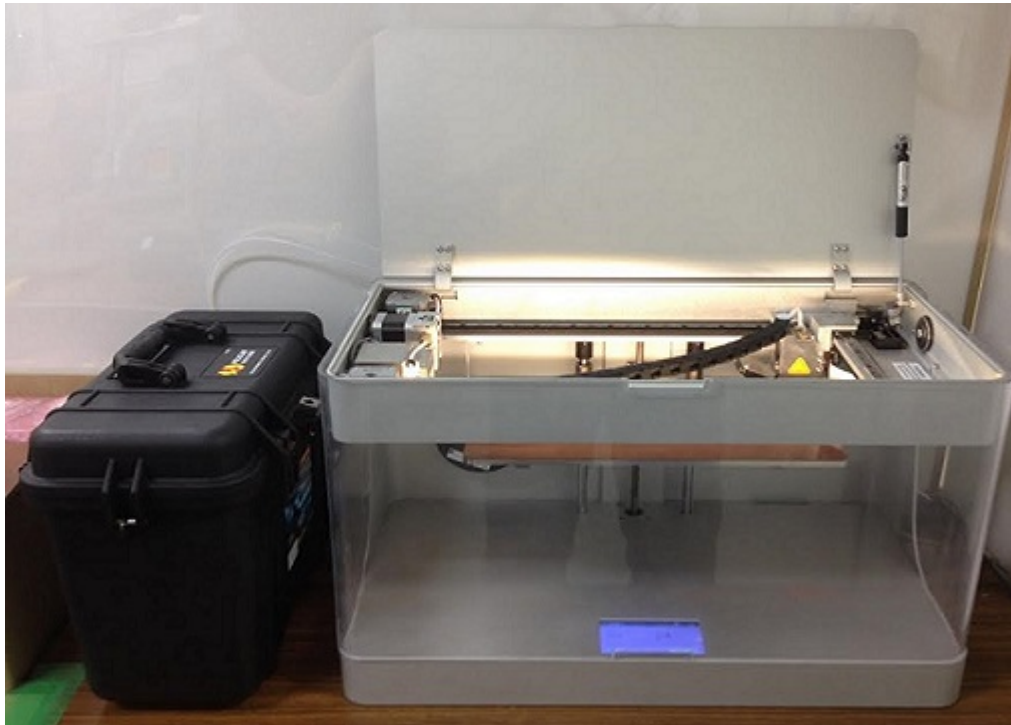


Figure 2.2: The Mark One[®] 3D printer by MarkForged[®]. The black case on the left is the container for the nylon matrix material.

based 3D printers, the print head has two nozzles. One nozzle is for printing the nylon matrix material, the other nozzle is used to deposit the fibre filament. The nylon spool consists of 1000 cm^3 of filament and is mounted in a waterproof, black container, which can be seen on the left side in fig. 2.2. The reason for this is that nylon can absorb water with relative ease, which may become dangerous when the nylon filament is heated to 265° C . The absorbed water will start to boil and expands rapidly, disintegrating the filament and creating poor prints. The Mark Two[®] can, besides nylon, also print Onyx[®] as matrix material. The Onyx[®] material is nylon pre-impregnated with carbon micro-fibres. Onyx[®] is stronger than nylon and has a matte black finish. It is possible to use Onyx[®] as a stand alone material in prints, but it is also possible to reinforce it with fibre filaments.

There are three types of fibre filament that the Mark One[®] can print, which are shown in fig. 2.3. These are glass-, carbon-, or Aramid[®] fibre filaments. The Mark Two[®] is also capable of printing high strength high temperature (HSHT) fibre filament,^[61] which is a type of glassfibre.

The Markforged[®] company has published data sheets on the mechanical properties of the matrix materials and on fibre reinforced nylon composites. This data of matrix and fibre reinforced nylon materials are presented in table 2.2 and table 2.3, respectively.^[12]

2.2.2. Material supply to the print head

Both the Nylon filament spool and the fibre filament spool supply the materials through separate tubes to their respective nozzles on the print head. A schematic overview of the material feeding system of the MarkForged[®] 3D printers is shown in fig. 2.4. It should be

Table 2.2: Selected mechanical properties of the matrix materials used by the MarkForged[®] 3D printers^[12]

Property	Test standard	Nylon	Onyx
Tensile Stress at Break [MPa]	ASTM D638	54	30
Tensile Modulus [GPa]	ASTM D638	0.94	1.4
Tensile Strain at Break [%]	ASTM D638	260	58
Tensile Stress at Yield [MPa]	ASTM D638	31	36
Tensile Strain at Yield [%]	ASTM D638	27	25
Flexural Strength at Break [MPa]	ASTM D790	32	81
Flexural Modulus [GPa]	ASTM D790	0.84	2.9
Flexural Strain at Break [%]	ASTM D790	n/a	n/a

Table 2.3: Information on mechanical properties of fibre reinforced nylon composite specimens^[12]

Property	Test standard	Carbon CFF	Aramid CFF	fibre-glass CFF	HSHT Glass CFF
Tensile Strength [MPa]	ASTM D3039	700	610	590	600
Tensile Modulus [GPa]	ASTM D3039	54	27	21	21
Tensile Strain at Break [%]	ASTM D3039	1.5	2.7	3.8	3.9
Flexural Strength [MPa]	ASTM D790	470	190	210	420
Flexural Modulus [GPa]	ASTM D790	51	26	22	21
Flexural Strain at Break [%]	ASTM D790	1.2	2.1	1.1	2.2
Compressive Strength [MPa]	ASTM D6641	320	97	140	192
Compressive Modulus [GPa]	ASTM D6641	54	28	21	21
Compressive Strain at Break [%]	ASTM D6641	0.7	1.5	n/a	n/a

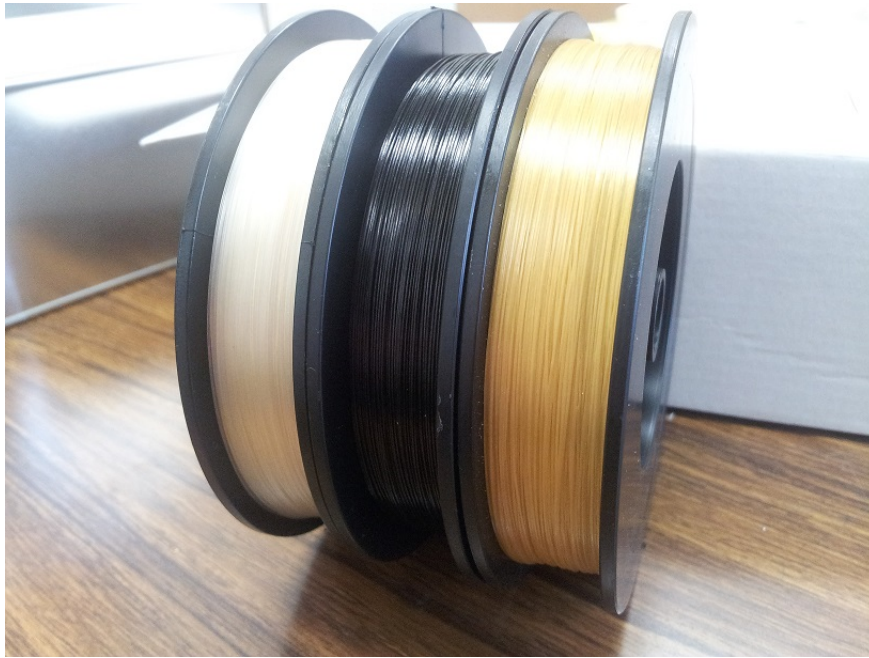


Figure 2.3: The spools with fibre filament used by the Mark One[®]. From left to right: Glass Fibre, Carbon Fibre, Aramid[®] Fibre. Each spool contains 50 cm³ of fibre filament

noted that the MarkForged[®] printers will only print one type of material at a time. The printer is either depositing matrix material or fibre filament, never both at the same time.

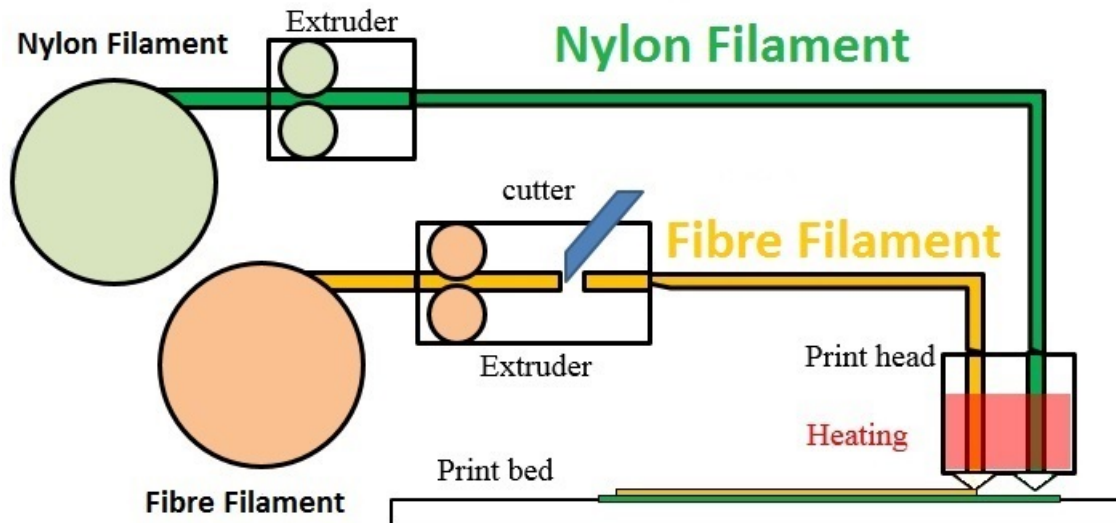


Figure 2.4: Schematic overview of the nylon and fibre feeding systems of the MarkForged[®] 3D printers. Note that the red area in the print head indicates the area that is heated.

The nylon filament system (green) and the fibre filament system (yellow) are both practically the same except for the fact that the fibre system has a cutting tool, that cuts the fibre filament at a required length. The nylon spool is fed to the extruder, which then pulls the filament from the spool into the tube leading to the print head. In the print head, the nylon

gets heated to 265° C, which is above the melting temperature, making the nylon ready to be deposited.

The fibre filament is fed to the fibre extruder, which will pull the fibre through a tube towards the print head. When fibre reinforcement is required in the sample, the print head will first construct the nylon outlines of the layer, after which it pauses. During this pause, the fibre filament is fed through the tube until it the tip of the nozzle. The fibre filament is also heated to 265° C, in order to melt the fibre filament resin, which acts as a binder between the fibres and the matrix. Once the fibre filament is extruded from the nozzle, the print head will continue its movements. When enough fibre is used for the current layer, the cutter is automatically activated, cutting the fibre filament to avoid waste of material. Fig. 2.5 shows the location of both the nylon and fibre feeding systems in the Mark One[®].

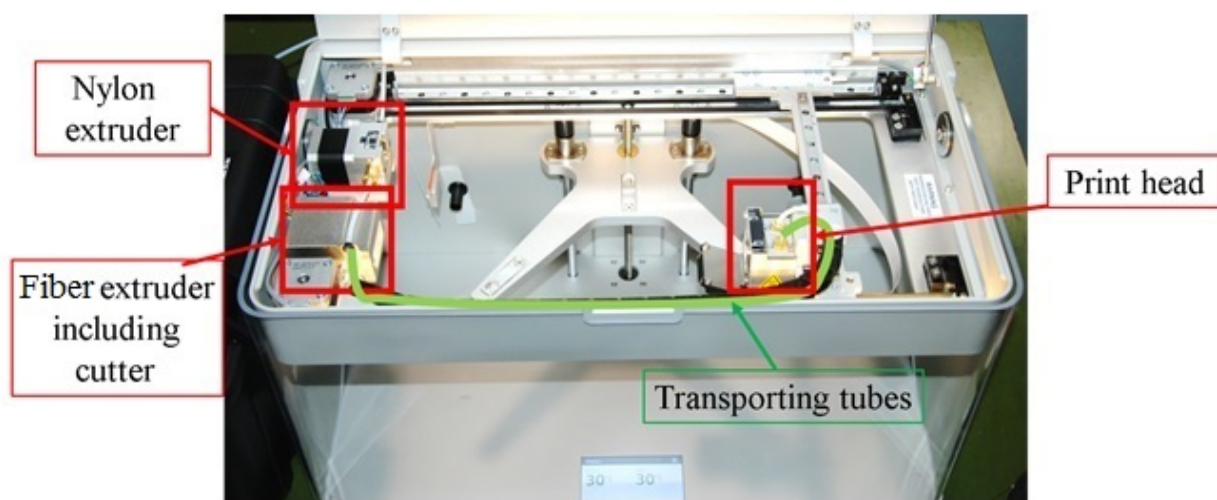


Figure 2.5: Top view of the Mark One[®]. In this image both the nylon and fibre extruder (red) can be seen as well as the top of the print head (red). The transporting tubes are not fully visible, but have been traced with a green line.

During the printing of one layer, the print bed will not move, but the print head will move in the horizontal x- and y-directions and is controlled by servo motors, highlighted in fig. 2.6.

Once the layer is finished, the print head stops moving and the print bed will move in the z-direction to be able to print the next layer on top of the previous one. These movements of the print bed and print head are operated automatically during printing. The print bed moves along a spindle and moves with predetermined steps of 0.1 mm for glass and Aramid[®] and 0.125 mm for carbon fibres. This difference in step size is because of the diameter of the fibre filament bundles.

The diameter of the carbon fibre filament was measured to be 0.374 mm. The other bundles have a diameter of 0.33 mm. These are a factor 3 different from the layer thickness, so in order to fit the fibre filament inside the dimensions of the layer, it has to change from a cylindrical shape to a rectangular shape. The area of the carbon fibre filament bundle is 0.10986 mm², which has to be translated to a rectangular shape. The height of this rectangular shape is the same as the layer thickness, so the width of the rectangular shaped fibre

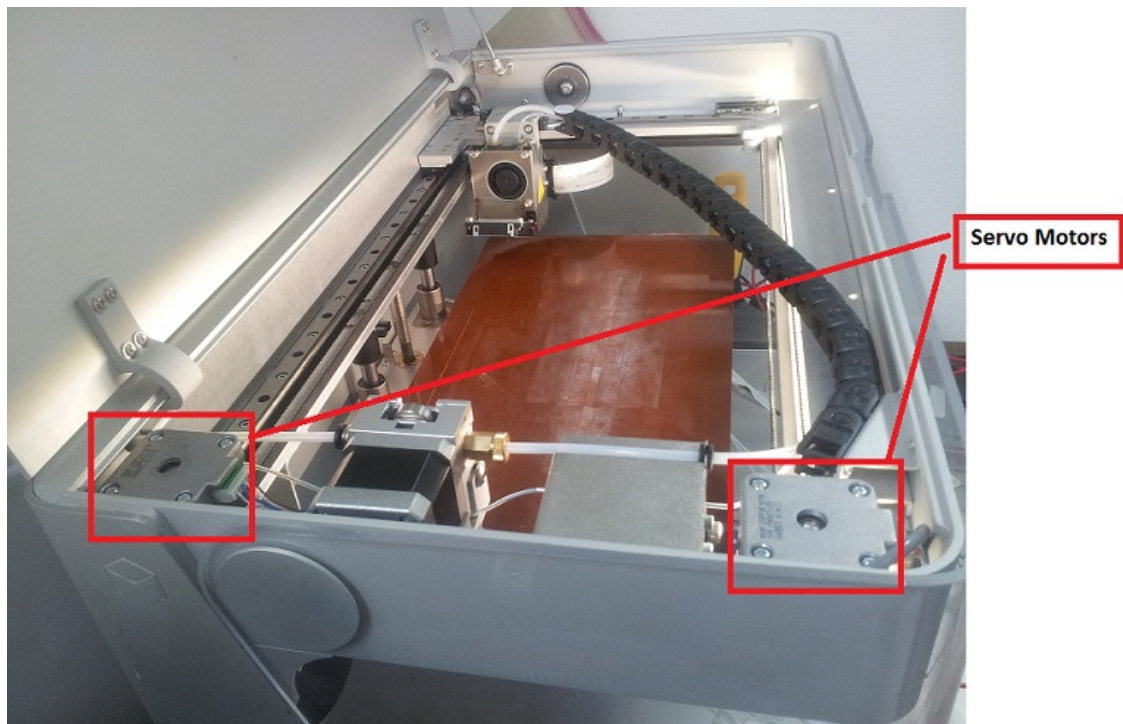


Figure 2.6: Top-angled view of the Mark One[®] showing the servo motors.

bundle is $0.10986 \text{ mm}^2 / 0.125 \text{ mm} = 0.87888 \text{ mm}$.

The other fibre bundles have an area of 0.0855 mm^2 . To obtain the same width in square form as the carbon fibre bundle has, the layer has to be $0.0855 \text{ mm}^2 / 0.87888 \text{ mm} = 0.0973 \text{ mm}$ thick, which is rounded up to 0.1 mm .

2.3. The Eiger[®] software

The MarkForged[®] printers have their own software program for uploading the .stl-files to the printer. The software, called Eiger[®], has several options for modifying the stl-files, according to the users desired specifications. A screenshot of a .stl-file in the Eiger[®] program is shown in fig. 2.7.

The simple square sample, shown in fig. 2.7, was used to test the MarkForged[®] 3D printers. The sample has a simple geometry with fibre reinforcements at the edges and nylon material in the center. An internal view of one of the layers of the sample is shown in fig. 2.8.

In this figure it can be seen how the fibres are orientated in the sample. When designing and printing, the following aspects should be noted:

- 1 Eiger[®] does not allow a print to start with a fibre reinforced layer, nor to end with one. These outer layers need to be of matrix material.
- 2 The layer thickness for glass- and Aramid[®] fibres is fixed at 0.1 mm , while the layer thickness of carbon fibre layers is fixed at 1.25 mm .

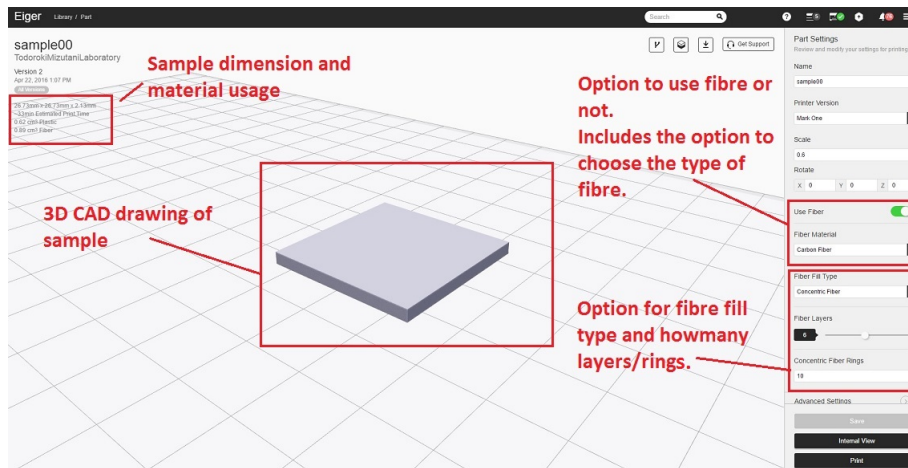


Figure 2.7: Screen shot of the Eiger[®] software program. Different aspects of the interface are highlighted.

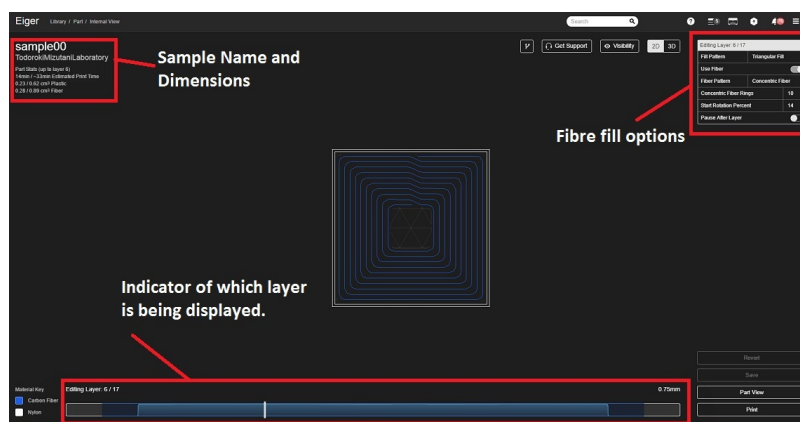


Figure 2.8: 2D image of one of the layers the sample shown in fig.2.7 from the Eiger[®] software program. The blue lines indicate the carbon fibres.

- 3 There is a minimum area that can be reinforced with fibres, when the area of the layer is lower than this minimum, the printing fails.
- 4 The Eiger[®] software requires the print to have at least 1 wall layer of pure nylon around the fibre filament reinforcements.
- 5 The temperature and print head velocity, as well as the layer thickness are predetermined and cannot be changed by the operator.

These design constraints were discovered during preliminary studies to try and reduce the dimensions of the sample shown in fig.2.7. All the samples that were printed should have nylon layers on the bottom and top. These so-called floor and ceiling layers will be at least 1 layer thick and can be 10 layers thick at maximum, however it is recommended to have a thickness of 4 layers for both floor and ceiling to obtain a waterproof sample with good surface quality, without increasing the printing time too much.

A second type of layer that is added to the design by the Eiger[®] software is the so-called wall layer. Wall layers can be set to a minimum of 1 and a maximum of 4 layers on each edge. Each wall layer is 0.4 mm in width. The recommended number of wall layers is 2.

2.3.1. Selection of printer parameters in Eiger[®]

Standard parameters

The screenshot displays the standard settings interface in the Eiger software. It is organized into five distinct sections, each highlighted with a colored border and a corresponding number:

- Section 1 (Red):** 'Printer Model' dropdown menu set to 'Mark One'.
- Section 2 (Orange):** 'Scale' input field set to '0.6', 'Rotate' button with a question mark, 'Manual Rotation' button, and 'X', 'Y', 'Z' coordinate input fields, all set to '0'.
- Section 3 (Dark Green):** 'Plastic Material' dropdown menu set to 'Nylon'.
- Section 4 (Light Green):** 'Use Fiber' toggle switch is turned on, 'Fiber Material' dropdown menu is set to 'Carbon Fiber', and 'Preserve Custom Fiber' toggle switch is turned off.
- Section 5 (Blue):** 'Fiber Fill Type' dropdown menu is set to 'Concentric Fiber', 'Walls to Reinforce' dropdown menu is set to 'Outer Shell Only', 'Fiber Layers' slider is set to '6', and 'Concentric Fiber Rings' input field is set to '10'.

Figure 2.9: Standard settings in the Eiger[®] software program.

Fig. 2.9 shows the interface of the standard group of settings that can be selected by the user. The options that are shown in fig. 2.9 will be explained from top to bottom.

The first option (red) is to choose which printer to print with. All MarkForged[®] printers that are bought are linked to the owners Eiger[®] account so that the .stl-files only have to be uploaded once.

Option 2 (orange) is about the scale of the part and its orientation on the print bed. When a .stl-file is uploaded in the Eiger[®] cloud, it might be the case that it does not fit on the print bed. In this case, the scale of the part can be changed as desired, without having to rescale the base file in the CAD imaging software program. Besides rescaling, the part can also be rotated in the x-, y-, and z-directions to find the most optimal printing direction in order to reduce printing time or achieve a more favourable fibre orientation.

The third option (dark green) gives the option to choose the matrix material. If during option 1 a Mark One[®] was chosen, only Nylon is available as material.

Option number 4 (light green) is the option to use fibres. If it is chosen to use fibre filaments, the user has the option to choose which type of fibre filament is used. For the Mark One[®], only the glass-, carbon-, and Aramid[®] filaments are available. The HSH filament is also available if the Mark Two[®] was chosen in option 1 (red).

The Preserve Custom Fiber option (light green fig. 2.9 can be turned on after all standard and advanced details of the fibre filament placement have been determined. This option makes sure that nothing can be changed with regards to the fibre filament settings that were selected.

The final and fifth of the standard options (blue) is only available if fibre reinforcements are required. In the first field, the fill type has to be chosen. The options are: 1) concentric fibre placement and 2) isotropic fibre placement.

Concentric fibre placement will have the print head follow the contours of the part and deposits the fibre filaments along the wall layers. Fig. 2.10 shows an example of concentric fibre placement. It can be observed that the concentric fibres form rings.

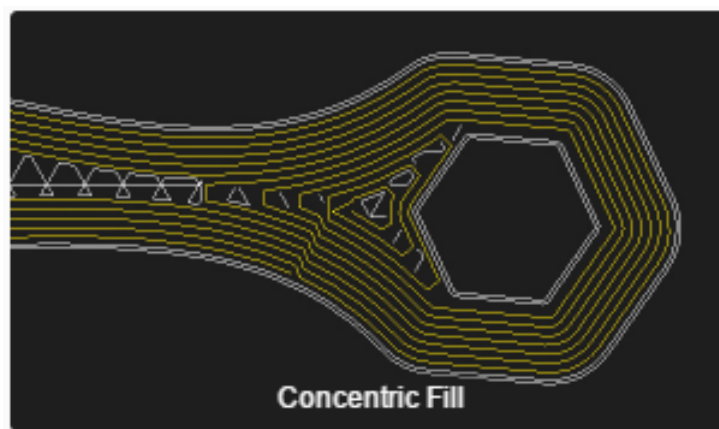


Figure 2.10: Concentric fibre placement as shown by the Eiger[®] software. The yellow lines show the orientation of the fibre filament. The white lines are the wall layers.

Two options are applicable when concentric fibre placement is chosen. The first is about which wall layers to reinforce. Here the user can opt to reinforce only the outer walls, only the inner walls (e.g. walls around internal pin holes), or both inner and outer walls. The second option is about how many layers in total shall be reinforced with fibres. The minimum value is 1. The maximum value is equal to the maximum amount of layers in the sample, minus the number of floor and ceiling layers.

The final standard choice in option 5, is how many concentric fibre rings have to be used. The minimum is one, the maximum depends on the geometry of the part. When the user fills in a number that is larger than this maximum, Eiger[®] will automatically use the maximum value possible.

In case of isotropic fibre placement, the fibres in a layer are placed in a single direction as can be seen in fig. 2.11

It has to be noted that, when choosing for isotropic fibre fill, an additional option becomes available which is not shown in fig. 2.9. This option is to set the orientation of the fibre filaments, with respect to the chosen x-axis of the part, in degrees. Besides this, the user also

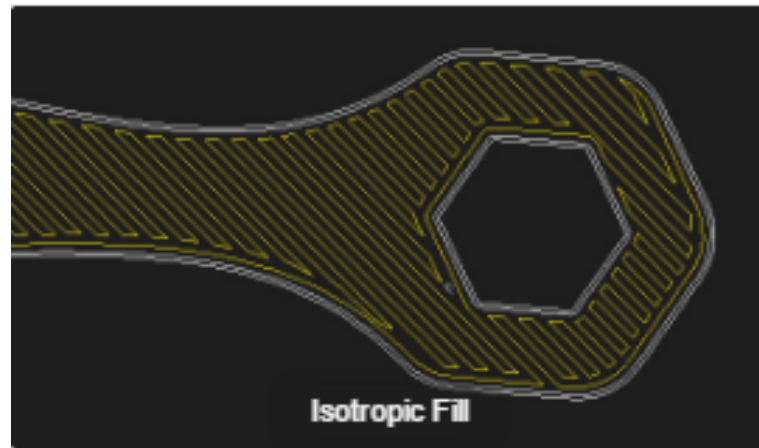


Figure 2.11: Isotropic fibre placement as shown by the Eiger[®] software. The yellow lines show the orientation of the fibre filament. The white lines are the wall layers.

has to specify the number of concentric rings that are to be used. The isotropic fibres will be placed inside of the concentric fibre rings. To illustrate this, fig. 2.12 shows a square with isotropic fibre fill (yellow). In this case, it was chosen to use a value of 10 for the concentric fibre rings (blue).

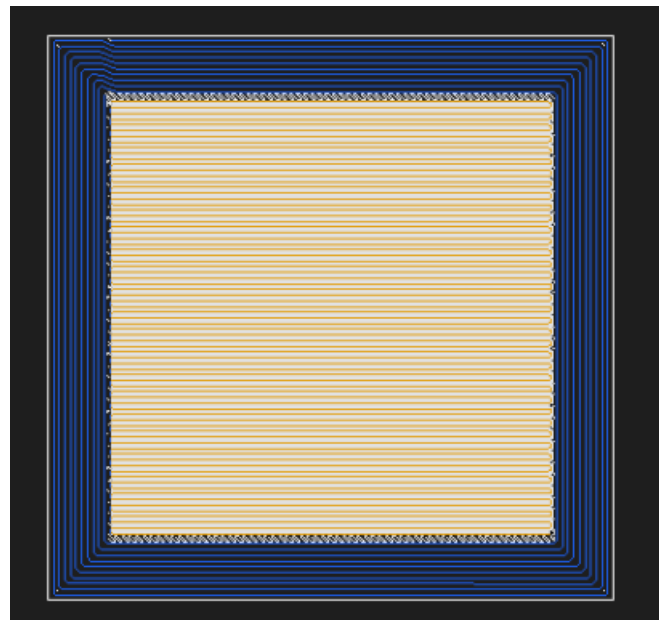


Figure 2.12: Square sample with isotropic fibre fill and 10 concentric fibre rings. The fibre filament is shown in blue. It can be seen that the concentric rings reinforce the walls, the isotropic fibre filament is placed inside the area surrounded by the concentric rings.

Advanced parameters

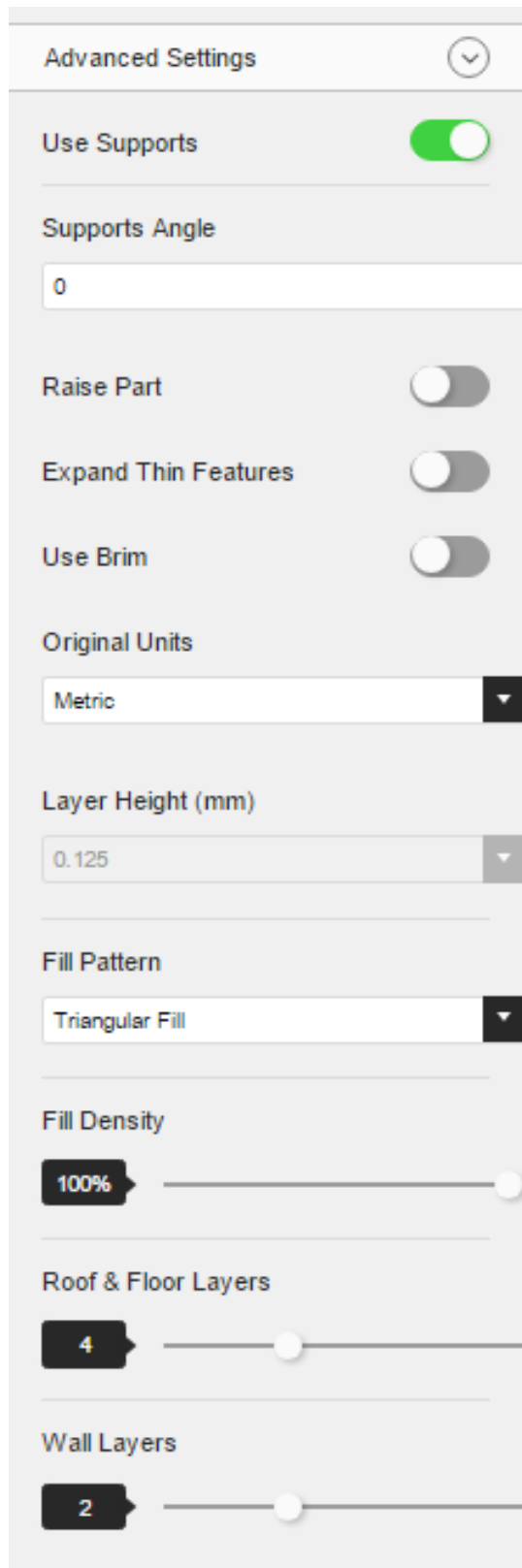


Figure 2.13: Advanced settings in the Eiger[®] software program.

Fig. 2.13 shows the advanced settings in the Eiger[®] software program. The advanced settings are regarding the matrix material only.

The first 2 options are regarding supports. If there are any overhangs in the part, it is recommended to use supports. In order to save print time and material, it can be opted to place the supports under an angle. The part can also be raised, to place it completely on 20 layers of supports. This is only recommended if the user designed supports are too small or not sturdy enough.

The next two options are "Expand Thin Features" and "Use Brim". The expand thin features is used when thin parts in the design are too thin to be printed. This feature does slightly oversize these areas. The brim is useful when a part has little contact with the print bed and the brims are used for holding a part in place during printing.

The last 4 options in fig. 2.13 are about the matrix fill pattern. Any non-reinforced parts that are not part of floor, ceiling, and wall layers will be filled as selected here. There are three options for fill patterns. These are:

- Triangular Fill
- Hexagonal Fill
- Rectangular Fill

The floor and ceiling layers are always filled isotropically, which means that the layers are completely filled under alternating angles of 45° and -45° . Hexagonal, rectangular, and triangular fill patterns mean that the nylon areas are filled with hexagonal, rectangular, and triangular shaped patterns respectively. A triangular fill pattern is visible in fig. 2.14.

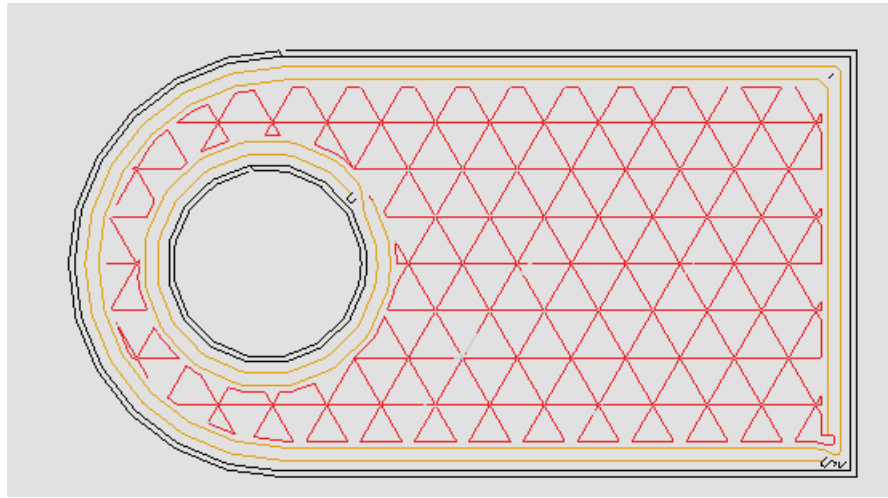


Figure 2.14: Hinge sample created in Eiger[®]. The black lines are the wall layers, the yellow lines are the carbon fibre filaments. The red triangles in the center of the part are made of nylon and represent the triangular fill pattern.

The last three settings shown in fig. 2.13 are fill density, number of roof and floor layers and the number of wall layers. The number of these layers is rather straightforward and it has been pointed out before that there must be at least 1 layer for all of these. The maximum number of wall layers is 4, the maximum for floor and ceiling layers is 10.

The fill density is about how dense the triangular, hexagonal or rectangular fill pattern is. The Eiger[®] program recommends 50% fill density to save print time and material usage. Higher density increases both the mechanical properties as well as the print time and material usage. The differences between 0 %, 50 % and 100 % fill density for a triangular fill pattern is shown in fig. 2.15.

2.4. Determining printing process via test print

The simple square specimen, shown in fig. 2.7, used for testing the printers, concentric fibre placement was chosen. With concentric fill, the printing of fibre filaments starts on the outside and moves inwards during the deposition of the filament. Fig. 2.16 shows several stages in the printing process of the square specimen. The finished product is shown in fig. 2.17.

There are, however, certain discontinuities visible after printing. One of these discontinuities is also visible in fig. 2.17 and is encircled in red. When the printer finishes a layer, the fibre is cut. If the fibre is too long, the fibre will end up in the next layer and might obstruct the deposition of fibre material at that specific location. In the worst case scenario, it might obstruct the print head movement and cause complete failure of the part. This is why the fibre bundle is cut before the required length is reached.

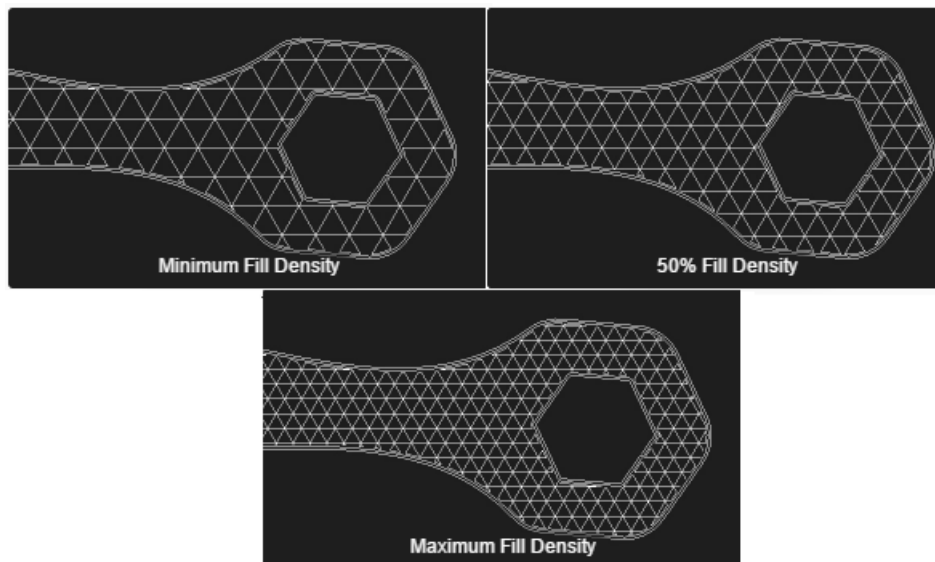


Figure 2.15: Triangular filled components showing different percentages of fill density. Minimum fill density (0 %), 50 % fill density and Maximum fill density (100 %).

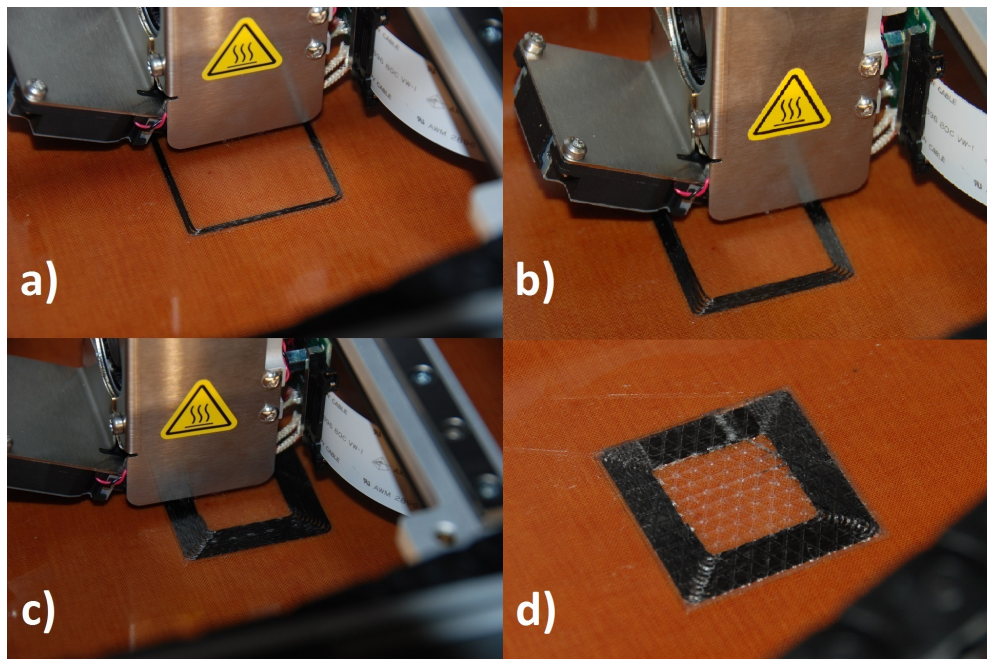


Figure 2.16: Stages of the printing process. a) After printing 2 carbon fibre concentric rings. b) After printing 4 concentric rings. c) After 8 concentric rings d) Completed layer.

The discontinuity shown in fig. 2.17, however, exists also because the fibre bundle does not immediately adhere to the subsequent layer and the print head sometimes starts moving before the adhering starts. The discontinuity in the case of the test sample was 14 mm long. It is possible to program the printer where to start printing the fibre filament, so the location of the discontinuity can be controlled. This is done in the Eiger[®] program, but as of yet there is no universal setting for this and it has to be repeated for each individual layer. Another type of discontinuity in the concentric fibre fill can be found at the point where the fibres are going to start the subsequent concentric ring. Here a small discontinuity occurs

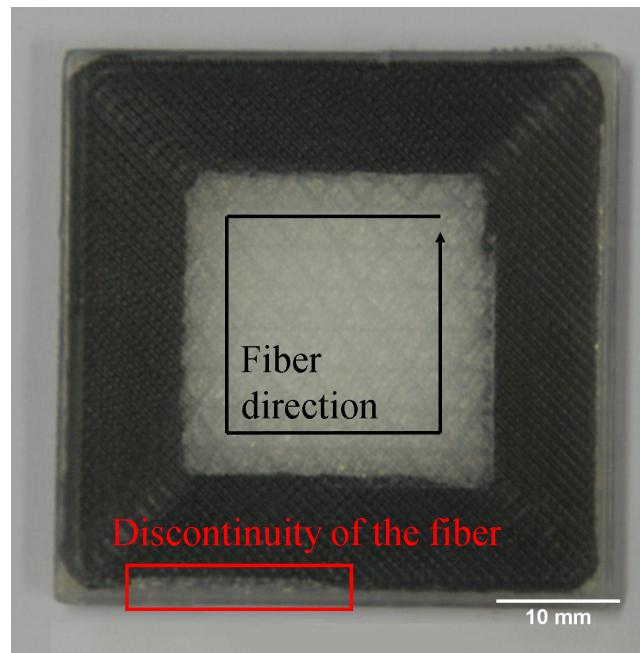


Figure 2.17: Finished test sample used to test the 3D printer. An occurring discontinuity is encircled in red.

that is under 45° of the main fibre direction, which equals the movement made by the print head to deposit the next concentric ring.

In a previous paper by the author^[8] tensile test specimens with these discontinuities were tested together with tensile test specimens that did have their discontinuities moved to areas that were not subjected to any stress. It turned out that the tensile strength, in case of a crucial discontinuity, is roughly 33 % lower.

2.5. Printer limitations

Even though some of the shortcomings of the MarkForged[®] 3D printers have already been addressed indirectly in the previous sections, they will be further elaborated here. Starting with the printing process itself.

First of all there are the dimensional restrictions to the sample. Apart from the maximum size, there also is a minimum size in case the sample has to be reinforced with fibres. This minimum size depends on the type of fibre orientation but is equal to 612 *mm* of fibre and is referred to as the one square inch rule. This 612 *mm* is the distance between the fibre cutter and the print head nozzle of the MarkOne[®]. Areas smaller than one square inch cannot be reinforced with fibres. The Mark Two[®] has the cutter placed very close to the print head, solving this problem.

A second disadvantage is that there is no temperature control of the print head, making it impossible to heat to higher temperatures than 265°C . This automatically means that the printer will be unable to use matrix materials with a melting temperature higher than this value, like PEEK (343°C). Also materials with a lower melting temperature will cause problems for the Mark Two[®] printed parts, limiting this printer to a very limited amount of

materials.

This disadvantage also holds for the types of fibre filaments used. MarkForged[®] supplies fibre bundles specifically created for their printers, however these fibre bundles also have shortcomings. The first is the low fibre volume fraction of 34.5%. The remainder is a polymer resin that melts in the print head and ensures that the fibres will adhere to the previous layer. Even though this concept allows for adherence of the fibre bundle, it also creates lower mechanical strength than when a fibre bundle of higher fibre volume fraction would have been used. It is, however, unknown how well the MarkForged[®] printers will handle other filaments with higher fibre volume percentages.

Another limitation is related to the software. Even though it is an adequate tool for slicing the .stl-file and calculating where to implement the fibres, there are a few shortcomings. One of which is that the program cannot export new files. It can only export the .stl-file the user has imported. It would be less time consuming when Eiger[®] could, once the fibres have been placed, export the file to a finite element analysis software package for calculations. Furthermore, there is no option in the Eiger[®] software to partially fill a layer with fibres. The fibres will either be in the whole of the layer, or not in the layer at all and are either placed concentric or isotropic. Besides this, there is no option to choose which walls to reinforce with the concentric fill. The user can now choose for all inner, all outer, or all walls. But this can be problematic for products with reinforced pin-holes when weight reduction is key and areas in the center of the part do not need to be reinforced.

Last but not least is the small discontinuity in the printed fibre as was shown in fig. 2.17. Even though the option to choose where a fibre layer begins exists in Eiger[®], there will always be a small discontinuity, which can severely effect the mechanical properties of the samples. In case of unidirectional specimens with six layers of carbon fibres, a discontinuity located in the middle of the sample could reduce the tensile strength by as much as one third^[8]. Moreover, there is no general function to make all fibre layers start at the same place. To achieve this, the user must manually change the fibre filament print starting point per layer, which becomes very time consuming for parts with many layers.

A promising development to note, is that in 2016 a new company in Russia, called Anisoprint[®], has started producing FDM based 3D printers with continuous fibres. This means that MarkForged[®] no longer has the monopoly in this field. Hopefully this will lead to cheaper printers and prints, as well as an improvement in quality of the parts.

3

Mechanical Test Samples and Test Set-ups



While, as described in chapter 2, a square sample was printed in order to obtain more information about the printing process itself, this chapter focusses on the samples printed for mechanical testing. First the printer and materials used will be discussed briefly. After this, the samples for mechanical testing will be presented. These samples will be processed into test coupons, on which some geometrical calculations are performed to determine the void percentage in the coupons. After the geometrical calculations, the mechanical tests will be discussed.

3.1. Printer settings

As was stated before, the prints created for the mechanical tests, as well as the structural aerospace part, were printed by the Mark Two[®] printer. Even though the printer settings were generally explained in the previous chapter, the exact settings that were used will be stated here.

As materials, the nylon filament was used as a matrix material and the carbon fibre filament was used as reinforcements. As for standard settings, the scale was kept as 1, and the part was rotated to fit the print bed and that the layers would be build in the height of the part. The fibre fill type was chosen to be concentric fibre fill, with only outer walls reinforced and 14 concentric fibre rings. In total the part consists of 16 layers, of which 8 are reinforced. The advanced settings were all left to the default settings. The default settings are no support, not raising the part and to not use brims nor have the thin features expanded. The layer height is 0.125 mm but this value cannot be changed by the user after a certain fibre filament is chosen. As a fill pattern, the triangular fill was chosen, with a 50 % fill density. Finally, the number of floor, wall, and ceiling layers was set to 4, 2, and 4 respectively.

Even though being very important printing parameters, the printing temperature as well as the print head velocity are not named in the standard or advanced settings. These settings are predetermined by the software and the user is unable to change these. The extrusion temperature is 265 °C, whereas the exact print head velocity depends on the material printed and is roughly 10 mm/s for nylon. For carbon fibre filament the value is less, but was not determined exactly nor was it found in the literature.

3.2. The Samples

Mechanical testing of a material is conducted in order to obtain material properties, with which a product can be designed accordingly. Several mechanical tests were performed, which are the ASTM D3039-14^[62] tensile test, the ASTM D790-03^[63] 3-point bending test, and the EN2850^[64] compression test. The coupons for these mechanical tests would be cut from the sample printed with the previously discussed settings. It was chosen to create the samples in such a way that all three types of coupons could be obtained from a single sample. In total 5 samples were printed, which were sawn into 15 coupons, 5 tensile, 5 bending, and 5 compression. Fig. 3.1 shows one of the printed samples.



Figure 3.1: A completed sample by the Mark Two[®]. The fibre bundles are placed concentric so that these are unidirectional in the long parts of the sample.

The sample shown in fig. 3.1 has a total length of 280 mm and a total width of 35 mm with a gap of 250 mm by 5 mm in the middle. From this sample three coupons, that have lengths of 250, 200 and 50 mm for bending, tensile and compression test coupons respectively, are extracted as indicated in fig. 3.2. The sample is cut over all three red lines in order to obtain the three different coupons. After the sawing process the brims were ground off and the coupons were ready to be tested.

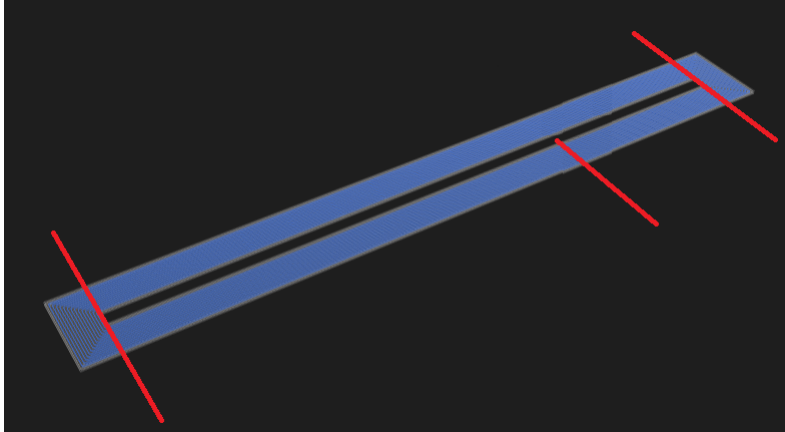


Figure 3.2: Schematic drawing of where the printed sample would be sawed.

After the mechanical tests were performed, the area where failure occurred was cut from the coupons and embedded under vacuum into a Struers® Epofix fluorescent resin. After curing, the resin was ground up to P4000 and polished up to 1 μm . The resin was chosen to be fluorescent in order to detect a better contrast between the matrix rich areas, voids, and delaminations. Fig. 3.3 shows one of the samples after the grinding and polishing processes.



Figure 3.3: Sample after being ground and polished up to 1 μm .

3.3. Geometrical calculations on the samples

Several calculations on the geometry as well as on the amount of fibre and matrix volumes were performed. These calculations help determine the mechanical properties of the composite material, which are to be implemented in the simulations at a later stage. Only the calculation of the tensile coupons are described here. The geometrical data given by Eiger[®] is shown in table 3.1

Table 3.1: Geometrical and volumetric data of ASTM D3039-14 sample given by the Eiger[®] software

	Units	Value
Length (L)	<i>mm</i>	280
Width (W)	<i>mm</i>	35
Thickness (t)	<i>mm</i>	2
Fibre volume	<i>mm</i> ³	$7.19 * 10^3$
Nylon volume	<i>mm</i> ³	$10.33 * 10^3$

When checking these values, it turns out these are not accurate, since the total volume of the sample should be 17.1 cm^3 according to eq. 3.1, whereas the nylon and fibre volume from table 3.1 added together are 17.52 cm^3 .

$$V_{total} = L * W * t - 250 * 5 * 2 = 17.1 * 10^3 \text{ mm}^3 \quad (3.1)$$

Here V_{total} is the total volume of the printed sample in mm^3 and L , W and t are the length, width and thickness of the specimen in mm respectively. A possible explanation for this might be that the Eiger[®] calculates the cut-out part (shown in fig. 3.1) as being filled with nylon. If assuming the sample has no cut-out section, the total volume is $19.6 * 10^3 \text{ mm}^3$ giving a total fill percentage of 89.39%, which is possible assuming a void volume of 10.61%.

Due to the fact that Eiger[®] supplied material volumes is not correct, calculations on the geometry and volume were conducted. Fig. 3.4 shows a schematic representation of the cross-section of the coupons.

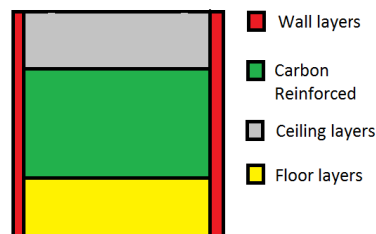


Figure 3.4: Sketch of the cross-section of an ASTM D3039-14 sample printed by the Mark One[®]. The different areas represent different types of layers, these are: floor layers (yellow), ceiling layers (grey), wall layers (red) and CF reinforced layers (green).

Based on fig. 3.4 the volumes of each of the layers will be calculated by using the values from table 3.2. First the total volume of the sample was calculated, after which the volumes of the separate areas (walls, floor/ceiling layers, fibre filament) were determined. For this

calculation a tensile coupon is taken. The values of the other coupons can also be calculated in the same way, since only their lengths differ.

The total volume of a tensile coupon is:

$$V_{total} = L * W * t, \quad (3.2)$$

The total volume of the wall layers (the red area in fig. 3.4) can be calculated by:

$$V_{wall-layer} = L * t_{layer} * W_{swl} * n_{wall-layer} * 2, \quad (3.3)$$

where $V_{wall-layer}$ is the total volume occupied by the nylon wall layers in one layer in mm^3 , t_{layer} is the thickness of one printed layer in mm , W_{swl} is the width of a single wall layer in mm , and $n_{wall-layer}$ is the number of wall layers specified in the Eiger[®] software program. The value is multiplied by two because there are in total two walls in these coupons. The volume of the floor layers is the same as that of the ceiling layers and can be calculated by:

$$V_{FC} = (W - 2 * n_{wall-layer} * W_{swl}) * L * n_{fc} * t_{layer}, \quad (3.4)$$

where V_{FC} is the volume of the floor or ceiling layer in mm^3 , and n_{fc} is the number of floor or ceiling layers as chosen in the Eiger[®] software. Finally, the volume of the carbon fibres is calculated as shown in eq. 3.5.

$$V_{fibres} = W_{fibre} * n_{concentric} * n_{fibre} * t_{layer} * L, \quad (3.5)$$

where V_{fibres} is the total volume occupied by fibres in mm^3 , W_{fibre} is the width of one printed fibre bundle in mm , $n_{concentric}$ is the number of concentric fibre rings as specified in the Eiger[®] program, and n_{fibre} is the number of fibre reinforced layers in the specimen. Values used in eq. 3.2 - 3.5 are displayed in table 3.2.

With the use of these equations it is concluded that theoretically the volume percentage of fibre filament equals 41% in the whole specimen. Where each individual reinforced layer has 82% fibre filament volume. This indicates that, when the $V_{wall-layer}$ of a single printed layer is added to this, 92.67% of each carbon fibre reinforced layer is filled with material. Roughly 7.33% is void. However, as stated in section 2.5, each fibre filament bundle only has 34.5% of its total volume filled with carbon fibres. So the actual fibre volume percentage, V_f , of a sample is 14.15%. Please be noted that to come to this conclusion it has been assumed that the floor-, wall-, and ceiling layers are 100% filled with nylon and no voids occur in those parts.

Table 3.2: Values of parameters used in eqs. 3.2 - 3.5

Parameter	Unit	Value	Parameter	Unit	Value
L	mm	200	W	mm	15
t	mm	2	t_{layer}	mm	0.125
W_{swl}	mm	0.4	$n_{wall-layer}$	-	2
n_{fc}	-	4	W_{fibre}	mm	0.879
$n_{concentric}$	-	14	n_{fibre}	-	8

It has to be noted that all the above calculations have been performed without taking any temperature effects into consideration. The thermal expansion coefficient of a nylon-6 material was found to be 85 mm/mmK . When considering a temperature difference of $240 \text{ }^\circ\text{C}$ between the extrusion temperature and the room temperature, the dimensions of the part will change if not compensated for by the Eiger[®] software. This compensation can be e.g. to over-dimension the part to compensate for the shrinking. The difference in these dimensions, assuming there is no compensation, is listed in table 3.3.

Table 3.3: Comparison between the dimensions of a design and the dimensions considering thermal effects.

	Design dimensions [mm]	Printed dimensions [mm]	Difference [mm]
Length	200	195.92	- 4.08
Width	15	14.694	- 0.306
Thickness	2	1.959	- 0.041

When comparing the total volumes of the design with and without thermal effects, there is a shrinkage of 6 %. However, this value is not exact, since the 14.15 % fibre volume is not effected equally much as the nylon is by the temperature, but a shrinkage of at least 5 % has to be accounted for. The voids, that are in the sample, will also shrink, but how much is uncertain.

3.4. Mechanical tests

The experiments were performed according to the standards of ASTM D3039-14 for tensile, ASTM EN2850 for compression, and D790-03 for bending . All tests were performed at room temperature and all load cells have been calibrated.

Tensile test

The tensile test was performed on the Instron[®] 5900R machine. The initial test set-up is shown in fig. 3.5. When testing in tensile, a coupon can get tabs attached to both ends. Tabs are small rectangular pieces of material that will act as a protective layer against the clamping force, so that this force does not damage the coupon. It was chosen to not use tabs, due to a rather large amount of nylon surrounding the fibres, which was sufficient to prevent any clamping damage to the fibre reinforced layers. The hydraulic pressure, however, was reduced to 50% in order to not crush the coupons, and was equal to 6.9 MPa (1000 psi). The temperature was 20.2° C with a relative humidity of 41.9 %. The force on the coupon was exerted by having the top clamps displace upwards with a velocity of 2 mm/min . All tests were continued until final failure occurred.

Compression test

The compression coupons were also tested on the same machine as the tensile tests. An image, showing the coupon clamped in the machine is shown in fig. 3.6. Since the coupons were too small to adequately fill the clamps, two support pieces of each 40 mm long were placed in the clamps to ensure the coupons would stay in place. The downward velocity of the upper clamp was 1 mm/min and the tests were performed at an average temperature of 22.5° C and a relative humidity of 55.8 %.



Figure 3.5: Initial test set-up of the ASTM D3039-14 tensile tests on the Instron[®] 5900R tensile test machine. The coupon is placed between the two clamps and an extensometer was applied.

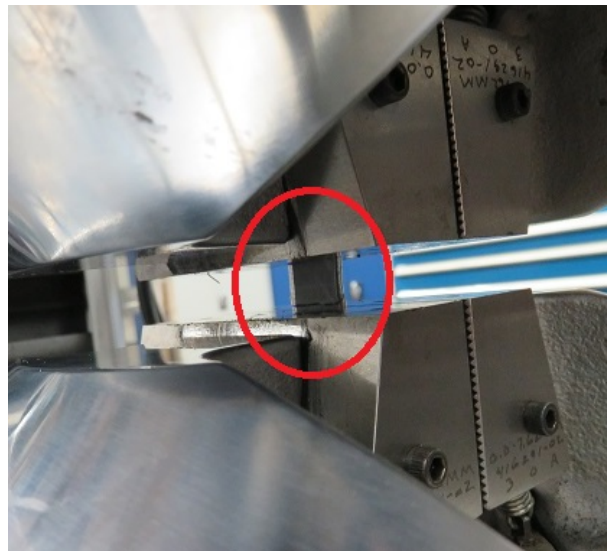


Figure 3.6: The test set-up of the compression test EN2850. The sample is encircled in red and is clamped in between the two hydraulic presses.

Bending test

The three point bending tests were also performed on the same machine as the tensile and compression tests, which was the Instron[®] 5900R. Fig. 3.7 shows the initial test set-up of the three point bending test.

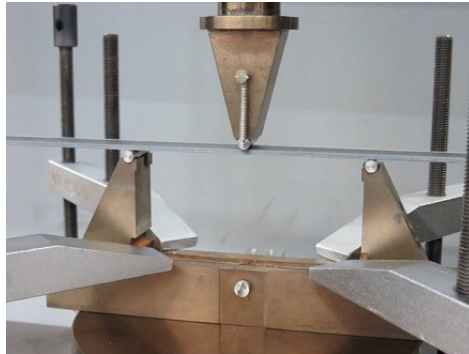
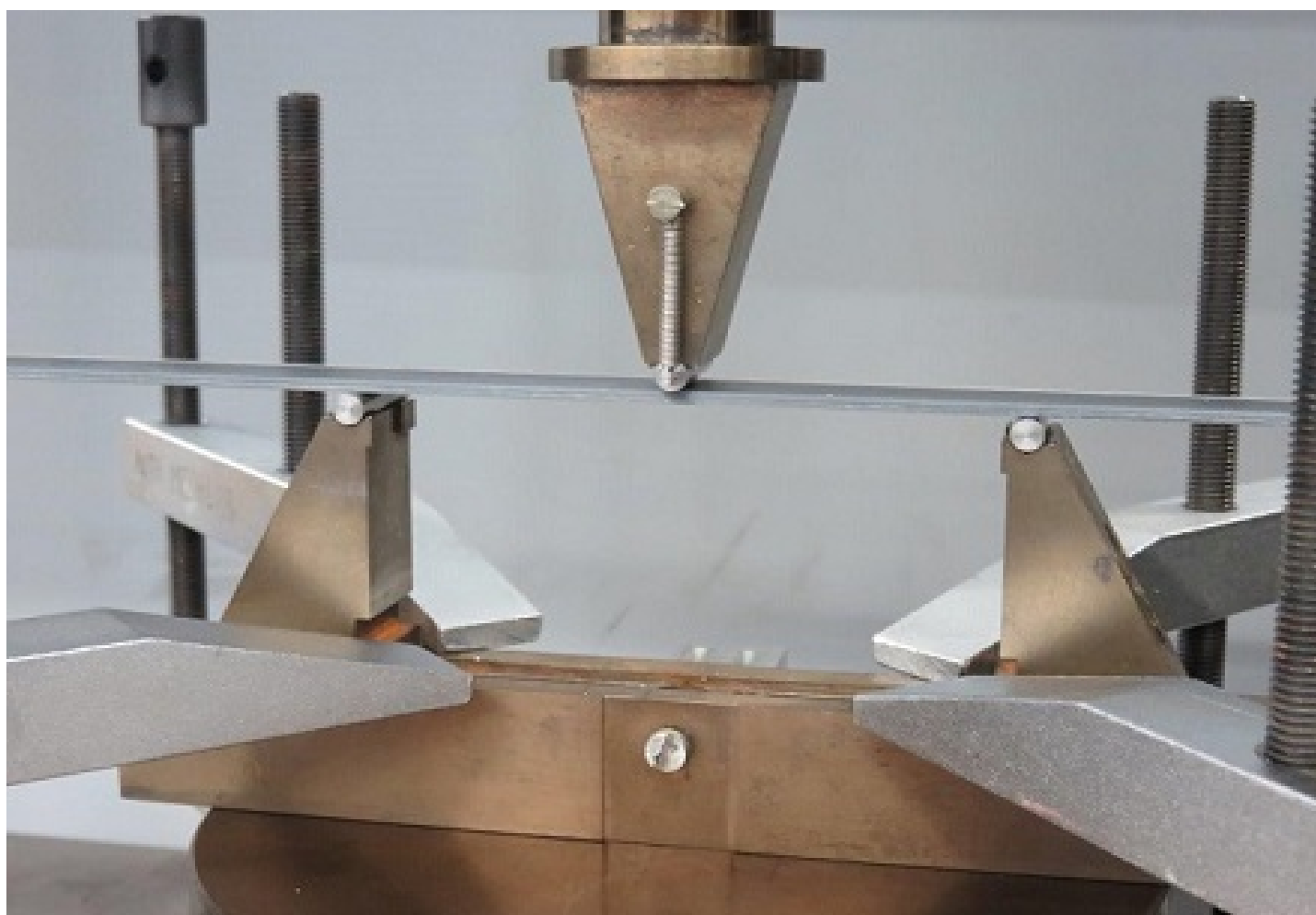


Figure 3.7: Initial test set-up of the ASTM D790-03 three point bending tests.

The tests were performed under 20.7° C and a relative humidity of 39 %. The span width between the two supports is 100 *mm* and the downward displacement of the center pin is 8 *mm/min*. These tests were continued until failure occurred.

4

Results and Discussion



This chapter will elaborate on the obtained results from the mechanical tests discussed in chapter 3. First a summary of the results obtained in chapter 2 will be given. After this, the obtained results will be presented. Finally, these results will be discussed in relationship with the microscopic results of the tested samples. A tensile test on the fibre bundles alone was also performed, the results can be found in appendix B. All these results will be discussed at the end of this chapter with assisting images of the micro structure of the coupons.

4.1. Initial results

The results listed in this section were presented in chapter 2 and include the trial and error experiments performed in order to test the limits of the Mark Two[®] printer.

- **Minimum/maximum number of nylon layers.** The Eiger[®] software program does not allow the part to start or end with a fibre filament reinforced layer. Walls layers are also mandatory. The minimum of nylon floor and ceiling layers is 1, the maximum is 10. For wall layers the minimum is 1 and the maximum is 4.
- **Discontinuities.** Since, for concentric fibre fill, the fibre filament starts on the outside, traces the contours of the sample, and then moves inwards. Small discontinuities in the fibre filament occur at the points where the inward movement is programmed. Another, larger, discontinuity is at the beginning of the fibre filament deposition. This discontinuity is created because the print head starts moving while the fibre filament might not have attached to the previous layer yet. These discontinuities can decrease the tensile strength of a coupon by approximately 33%.^[8]
- **Carbon filament fibre fill percentage.** As was shown in fig. 4.1 the carbon fibre bundle does only consist of 34.5% fibres^[8]. The other 65.5% is a polymer resin that will make sure the fibre filament adheres to the previous layer.
- **Coupon fibre fill percentage.** As discussed in chapter 3, the total percentage of the tensile test coupon, based on geometrical calculations, is approximately 14.2%.

4.2. Fibre bundle inspection

When the material properties supplied by MarkForged[®] were checked (tables 2.2 and 2.3), it turned out that no data on the actual fibre bundles was supplied. In order to understand the fibre bundle material better a HiROX[®] Digital Microscope KH-1300 was used to study the microstructure of a fibre filament bundle. The obtained image is presented in fig. 4.1.^[8] The white circular dots in fig. 4.1 are the carbon fibres, whereas the remainder is a special polymer coating. The task of this coating is to ensure that the fibres adhere to subsequent layers and to one another.

The exact composition of the coating was not presented by MarkForged[®], but is essential to know to exactly determining the material properties. For this a fibre filament bundle was investigated by Secondary Electron Microscopy (SEM). First the fibre bundle was checked by a Keyence VHX-100 microscope to detect if the sample had to undergo any further preparations before entering the SEM. A 3D image was created and is shown in fig. 4.2.

From fig. 4.2 it can be concluded that there are relatively flat surfaces available on which the SEM could be used. A backscatter electron mode was used to determine the composition of the matrix material. The electrons were generated with 15 *kV* and the working distance was set to 10 *mm*. The compositional analysis is shown in fig. 4.3 and table 4.1.

Due to the high amount of carbon and oxygen in the composition it could be assumed that the resin was a polymer. It was also known that the resin became very viscous at 265 °C.

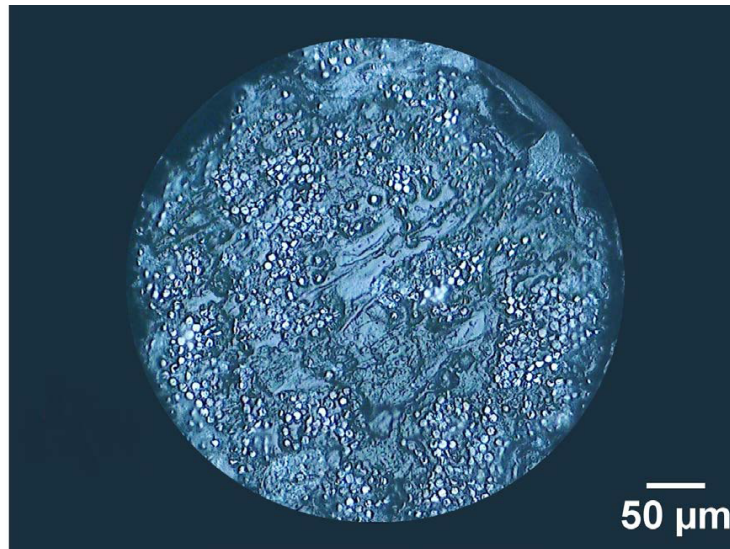


Figure 4.1: Picture taken by the HiROX[®] digital microscope KH-1300 at 700x magnification. A single bundle of MarkForged[®] Carbon Fibre Filament is shown. The white circular dots are the carbon fibres.

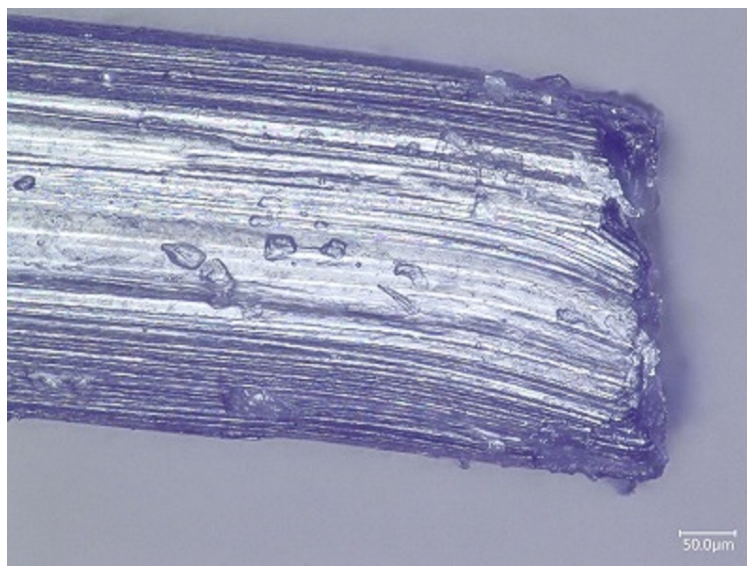


Figure 4.2: 3D image obtained by a Keyence VHX-100 microscope. The small particles on the fibre bundle are dust particles.

Table 4.1: Elemental composition of fibre bundle resin material.

Element	K	O	C	N	Na	S	Cl
Fraction	2.61	22.59	59.37	4.57	4.77	0.91	5.19

The exact polymer, however, could not be determined by this data alone and for future simulations it was assumed that this resin was nylon.

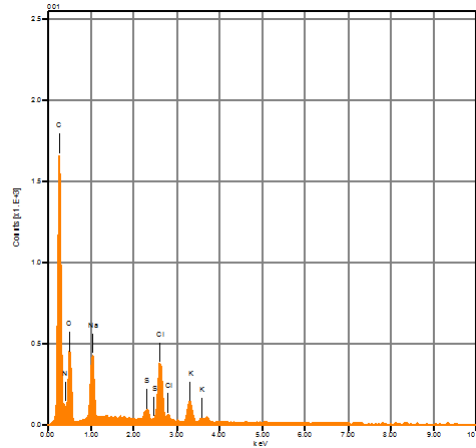


Figure 4.3: Graph showing the elemental counts vs KeV measured by backscatter electrons in the SEM. Only the resin material in the carbon fibre bundle was measured.

4.3. Tensile test results

In total 5 coupons were tested. These 5 coupons are labelled T1 till T5 and have dimensions as listed in table 4.2 measured by callipers and micrometers with accuracies of $\pm 0.01 \text{ mm}$ and $\pm 0.001 \text{ mm}$ for width and thickness respectively. The dimensional values displayed in table 4.2 are the average values of three measurements, performed on different locations on the coupons.

Table 4.2: Dimensions and mechanical test results of the tensile test coupons.

	Average Width [mm]	Average Thickness [mm]	Max. Load [kN]	Ultimate Tensile Strength [MPa]	Young's Modulus [GPa]
T1	14.66	2.14	12.0	382	29.7
T2	14.71	2.03	13.1	438	30.8
T3	14.71	2.12	12.6	403	30.0
T4	14.68	2.17	12.9	46	28.8
T5	14.66	2.13	12.9	415	29.9
Mean	14.68	2.12	12.7	409	29.8
Standard Deviation	0.03	0.04	0.44	20.35	0.73
Coefficient of variation	0.17 %	1.89 %	3.45 %	4.98 %	2.46 %

All the tensile test results were used to generate stress-strain graphs, which are combined in fig.4.4. The stress-strain curves of every tensile test coupon individually can be found in Appendix A1.

It was observed that all 5 coupons failed near the clamps with lateral cracks. The T1, T2 and T3 coupon failed at the top clamp, whereas the T4 and T5 coupons failed at the bottom clamp. Fig. 4.5 shows a tensile test coupon failed with a lateral crack at the top clamp.

From fig. 4.4 and table 4.2 it can be concluded that the scatter of the results is relatively

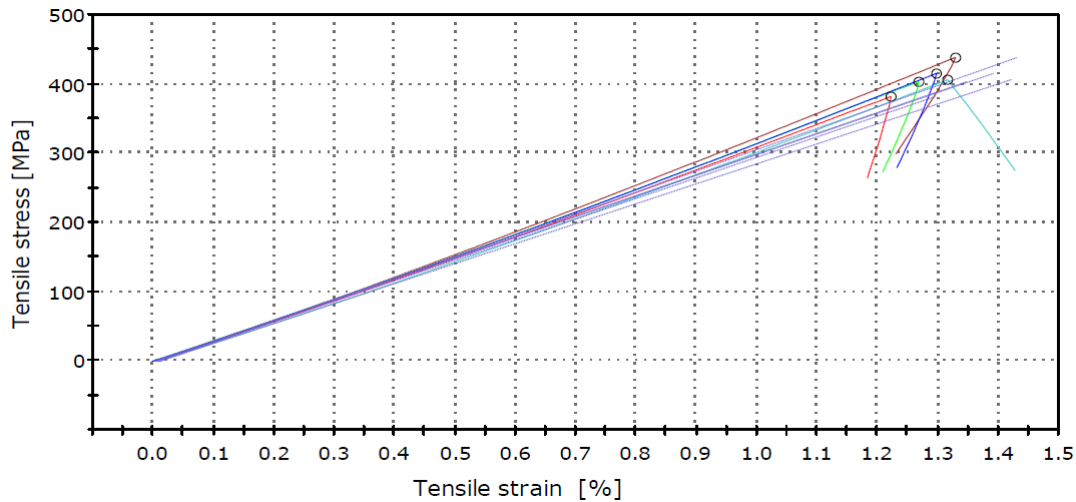


Figure 4.4: Stress-strain graph of the tensile test coupons T1 till T5. The circle indicates the point of failure. It can be observed that the failure is sudden and brittle.

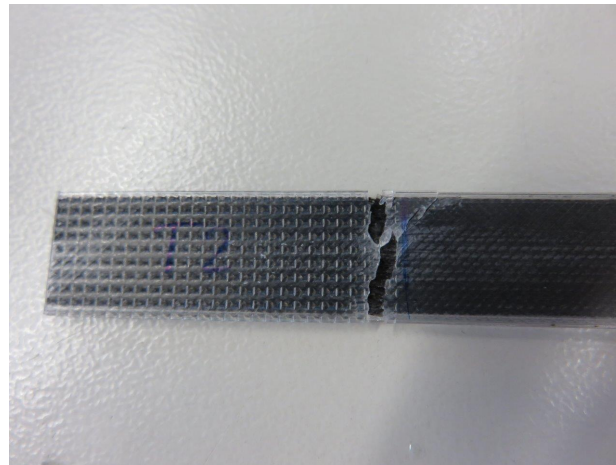


Figure 4.5: Failed tensile test coupon after being loaded in tensile. The specimen failed with a lateral crack at the top grip (LAT). The dents in the nylon at the end are due to the hydraulic pressure of the clamps.

small, even though there is a dimensional inaccuracy in the thickness as well as the width of the samples. The coefficient of variation in table 4.2 shows that the ultimate tensile stress has a scatter of at approximately 5 % whereas the young's modulus has a scatter of less than 2.5 %. Another important fact deduced from fig. 4.4 is that the test results are linear.

4.4. Compression test results

The results of the measurements and the compression tests are shown in table 4.3. Just as with the tensile dimensions, the compression dimensions also have a certain inaccuracy. The data obtained from the compression tests was used to create a stress-strain curve, which is shown in fig. 4.6. The stress-strain curves of the individual compression coupons can be found in Appendix A2.

From fig. 4.6 it was seen that the peak stress occurred at approximately 0.15 mm extension.

Table 4.3: Average width and thickness of the compression coupons, together with the measured test results.

	Average Width [mm]	Average Thickness [mm]	Maximum Load [kN]	Stress at Max. Load [MPa]
C1	14.83	2.07	3.18	104
C2	14.73	2.05	3.29	109
C3	14.74	2.07	3.31	109
C4	14.73	2.06	3.65	120
C5	14.88	2.00	3.24	109
Mean	14.78	2.05	3.33	110
Standard Deviation	0.07	0.02	0.18	6.17
Coefficient of variation	0.46 %	0.97 %	5.48 %	5.61 %

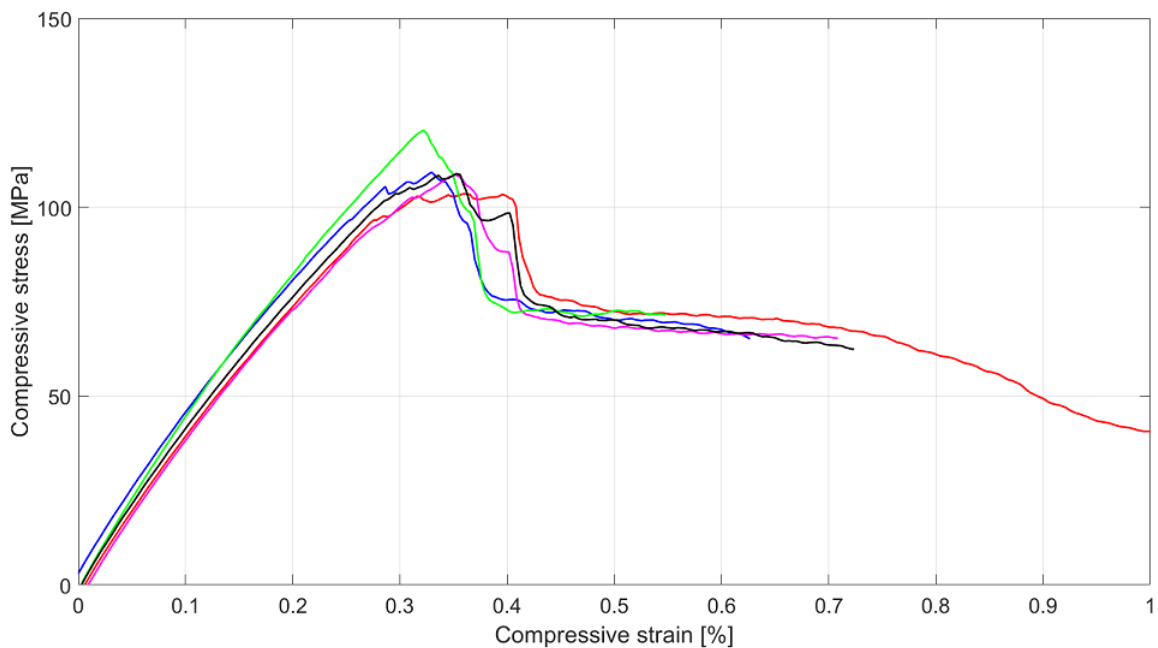


Figure 4.6: Stress-strain graph created with the data from the bending test coupons.

Here the coupon becomes unstable under the load until the the full fibre kinking occurred at roughly 0.2 *mm* compressive extension. When taking a closer look at the failed compressive coupons, it was observed that all coupons failed due to fibre kinking. It is important to note that the kinking of the fibres, and the resulting shear of the matrix, begins at both wall layers of the coupon and moves inwards. This is slightly visible in fig. 4.7, but will be better visible in the microscopic images in this chapter's discussion.

4.5. Three point bending test results

The coupons for the three point bending test have also been measured in the same way as the tensile and compressive coupons and the dimensions as well as test results are shown in

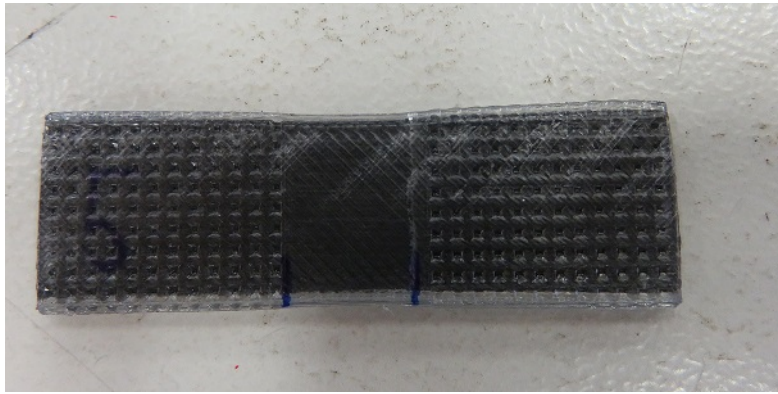


Figure 4.7: Compressive coupon after testing. The failure area is visible and failure starts from the edges and moved inwards.

table 4.4. The first three point bending test was not set-up correctly and no data acquisition was possible.

Table 4.4: Dimensions of the bending test coupons. The test values of the B1 coupon are missing due to incorrect test settings.

	Average Width [mm]	Average Thickness [mm]	Maximum corrected load [N]	Flexural Strength [MPa]	Flexural Modulus [MPa]
B1	14.71	2.14	-	-	-
B2	14.64	2.10	66.9	153	7480
B3	14.70	2.12	63.5	142	6890
B4	14.65	2.04	61.2	147	7520
B5	14.72	2.14	60.0	134	6770
Mean	14.67	2.11	62.9	144	7160
Standard Deviation	0.05	0.03	4	8.11	388.99
Coefficient of variation	0.27 %	1.90 %	6.36 %	5.63 %	5.43 %

Fig. 4.8 shows the resulting stress-strain graphs of the three point bending tests. The stress-strain curves of the individual bending tests can be found in Appendix A3.

It can be seen in fig. 4.8 that one plot (the cyan one), differs from the other three. This is because the two support rollers shifted away, just before the coupon failed completely. All four plots show roughly the same behaviour. First the stress-strain curve is linear, after which the stress-strain curve bends until final failure occurred. Fig. 4.9 shows the 5 bending coupons after their respective three point bending tests.

When taking a closer look at the possible failure modes for three point bending samples, two main modes can occur. One is the failure by tensile stresses in the layers below the neutral line, the other is failure due to compressive stresses in the layers above the neutral line. By inspecting the samples, it was concluded that both these modes occur in the coupons, but the tensile mode was the dominant failure mode, as will be more clearly visible in the microscopic images in this chapter's discussion.

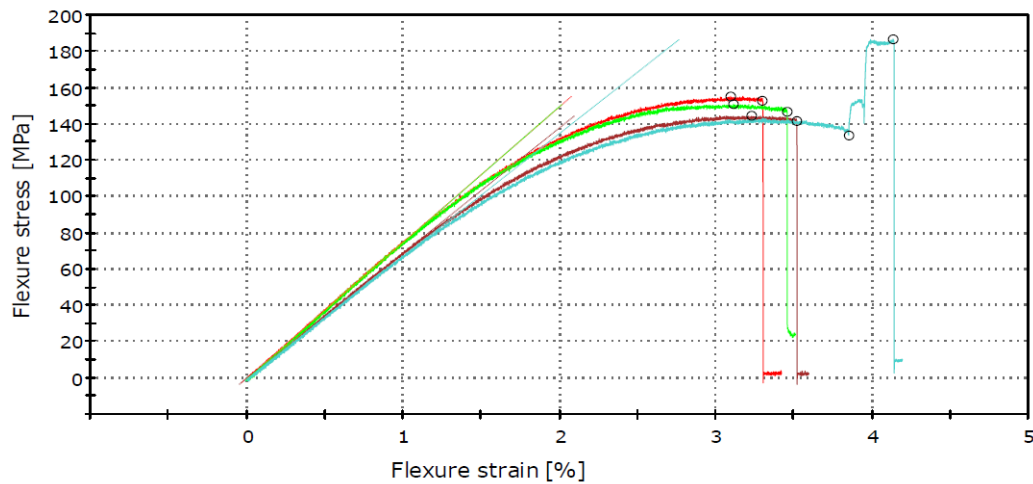


Figure 4.8: Stress-strain graph created with the data from the bending test coupons. The jumps in the cyan line of the B5 coupon was caused by the jumping away of the lower support rollers.

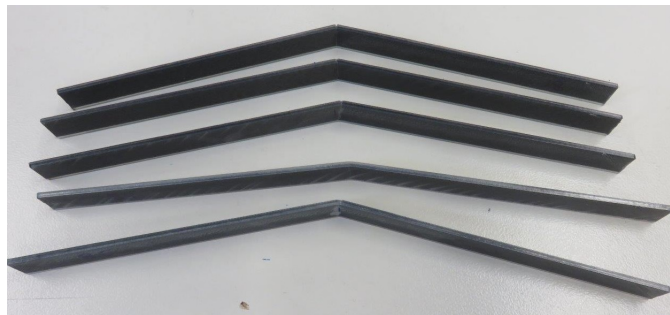


Figure 4.9: All five bending coupons after their respective tests. It can be observed that not all samples failed at the same point, as indicated by the kink angles in the samples.

4.6. Discussion of results and microscopic images

In this section the results obtained with the mechanical tests will be further analysed and discussed. Images of the micro structure of some of the tested coupons will be used to explain the material detail in more detail. The microscopic images were taken in two planes, the x-y plane and the y-z plane. Here the x-direction is the direction of the fibres, where the y-direction is the width of the coupons and the z-direction is the height. The images were taken at a depth of 5 mm in the x-y plane and at a depth of 1 mm in the y-z plane. In the microscopic images the white areas are carbon fibres, the light grey area is the fluorescent epoxy, the darker gray area is the nylon matrix material and the black parts are the void areas.

4.6.1. Tensile test discussion

Fig. 4.10 shows the T1 tensile test coupon in the x-z plane. It was observed that the clamped area is on the right side of the fracture, since the nylon top and floor layers are showing a wavy pattern, which is consistent with the hydraulic clamps used on this coupon. Since there is still some nylon visible present between the area where the clamps were and the

fibre reinforcements, it could be concluded that tabs were indeed not needed. The void areas are shown in black and it can be seen that they are both inside the fibre reinforced layers as well as in the nylon layers. The assumption made in chapter 3 about no voids existing in the nylon proves to be incorrect.

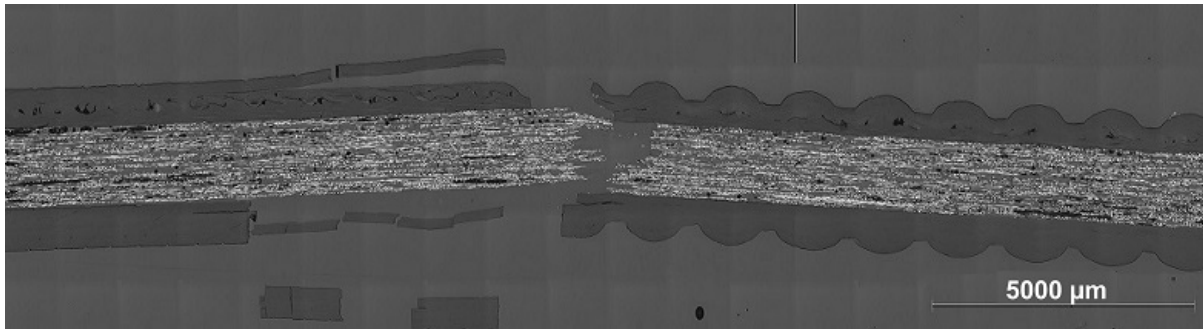


Figure 4.10: Complete image of the T1 tensile test coupon taken in the x-z plane.

Fig. 4.12 shows a close up of the fracture of a tensile test coupon. Some interesting features are visible. First of all, a delamination can be seen in the nylon layers, which can be a result of the failure of the sample, which releases all the stored elastic energy. This release of elastic energy resulted in compressive damage at the opposite site of the coupon, which is shown in fig. 4.11.

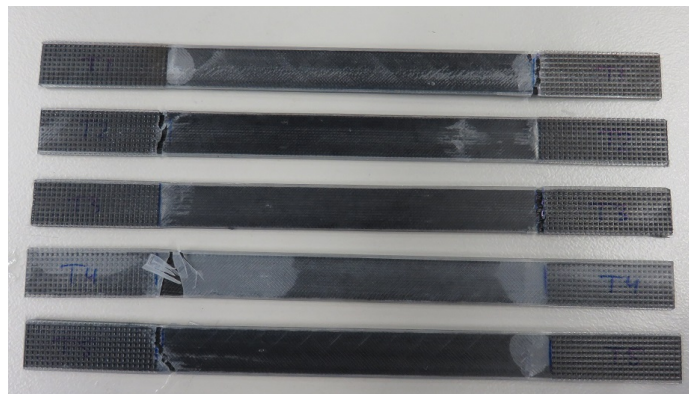


Figure 4.11: Tensile test coupons after failure. Besides the main tensile failures, other compressive failures were observed at the opposite end of the samples.

A second observation to note is that, even though the tensile test results show a linear elastic behaviour based on from the stress-strain curve, the fracture area seems to miss fibres. When reconstructing both fracture parts it would appear they do not fit. One reason for this is that at the point of final fracture, the fibres that were still carrying load fractured at multiple places, where parts of the fibres launch away during the fracture. When looking closely at fig. 4.12, small white fibre particles can be observed floating around in the resin.

A third point to address is that it is unsure whether the voids are inter-laminar or intra-laminar, since it is very difficult to tell where one fibre reinforced layer ends and a next one begins. A fourth interesting fact to note, which is clearly visible in fig. 4.13, is that the fibres are not 100 % unidirectional, but exhibit a slight wave pattern. Finally, fig. 4.13 also indicates that several voids in the coupon are relatively deep. The exact depth could not be determined.

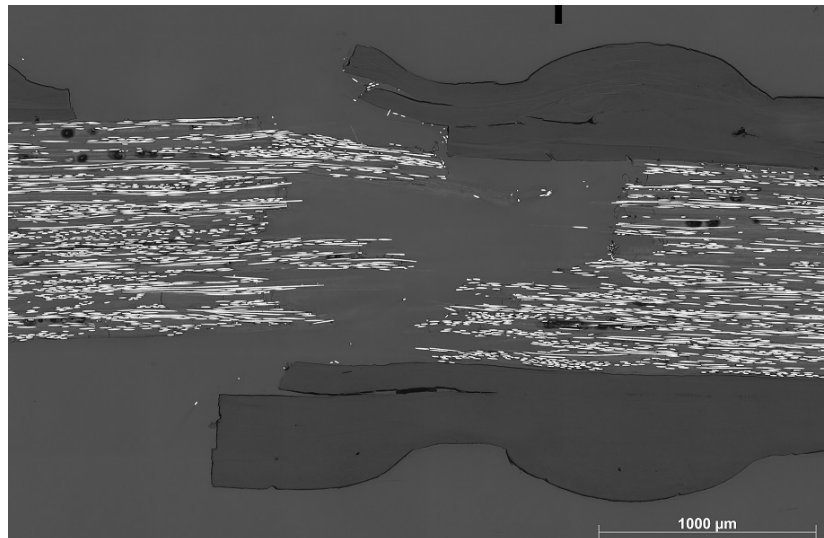


Figure 4.12: The tensile failure area of the T1 tensile test coupon.

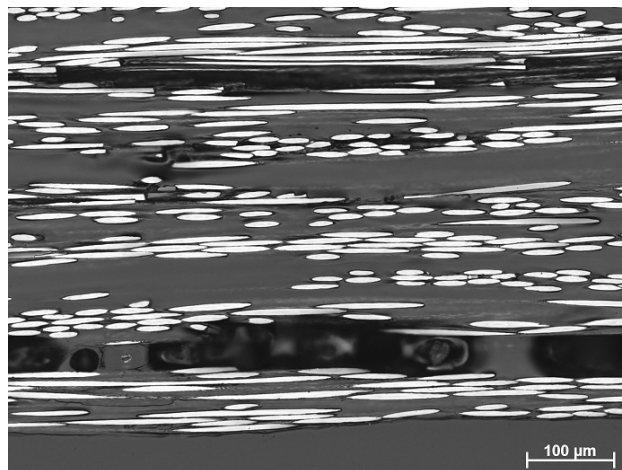


Figure 4.13: One of the many voids in the T1 tensile test coupon. It can be seen that this void is in between two layers and spans into the y-direction.

The linear result seen in fig. 4.4 could be clarified since almost all the load is carried by the fibres. Since the fibres are almost fully unidirectional, they do not have to be aligned by the tensile force, which otherwise would show a non-linearity at the start of the stress-strain curve. The reason why the coupons all failed near one of the clamps, was thought to be due to the clamping force exerting additional stresses to the material. These additional shear stresses make for a more complex stress situation just below the clamped area, which will be the area where the coupons were most likely to fail. If the sample will fail at the top or bottom clamp did not show a consistent trend. It is thought to be related to the amount and the location of void areas. If more void area is present at the top clamp, then the coupon is most likely to fail there.

When comparing the tensile test results obtained in this research with the data supplied by the MarkForged[®] company, several mismatches can be observed. A comparison between both results is visible in table 4.5.

Table 4.5: Comparison between tensile test data on carbon fibre reinforced composite material supplied by the MarkForged[®] company^[12] and the tensile test data obtained in this study.

Property	Carbon CFF	T1-T5 printed coupons
Tensile Strength [MPa]	700	409
Tensile Modulus [GPa]	54	29.8
Tensile Strain at Break [%]	1.5	1.3

From table 4.5 it can be observed that the carbon CFF prints created by MarkForged[®] are the mechanically superior ones, however in their datasheet it is not mentioned how many floor, wall, and ceiling layers are used when printing the coupons. Only the dimensions of the coupons are mentioned, which for tensile are 12.7 mm in width and 1.25 mm in height, equalling 10 printed layers. If the recommended settings of 4 floor, 4 ceiling, and 2 wall layers were used the fibre volume percentage, as calculated in chapter 3 would be 5.73 % only. When applying the rule of mixtures for the upper limit, a maximum possible tensile modulus of 14.1 GPa, assuming no voids exists in the material, can be reached. If the number of floor, ceiling, and wall layers was set to 1 each, then a maximum possible tensile modulus of 57.8 GPa is possible, due to a 24.84 % fibre volume fraction. From these calculations it was concluded that MarkForged[®] did not use the Eiger[®] recommended settings.

The tensile modulus of 54 GPa is only 6.57 % lower than the theoretical limit of 57.8 GPa. This is roughly half of what was discovered from the current research, where the tensile modulus (29.8 GPa) is 11.9% lower than the theoretical limit (33.35 GPa).

One of the reasons for this can be that MarkForged[®] had their parts tested, immediately after printing, thus not allowing moisture a lot of time to enter the nylon material. In this research, the parts were printed by a third party and there were several days between the printing and testing, allowing for more moisture to enter the coupons. Jia *et al.*^[65] discovered that moisture absorption in nylon-6 lowers the tensile strength, tensile modulus as well as the glass transition temperature significantly. A moisture content of 0.74 % already lowers the glass transition temperature to room temperature.

A second reason is the location of voids and the amounts of voids in the specimens. Since only 5 coupons were tested in both researches, the effect that the void distribution has is not negligible. Were more coupons tested, e.g. 50, then the effects of the void distribution and void amounts would be averaged out.

4.6.2. Compression test discussion

Fig. 4.14 shows the x-y plane of a compression coupon. An important result visible in fig. 4.14 is the failure mode.

In general, three failure modes exist for compression tests, which are micro-buckling, fibre kinking, and transverse tensile rupture. Micro-buckling is the buckling of the fibres in the matrix and has two different modes, extension and shear. In the extension mode, the fibres buckle out of sync and look like alternating sine and cosine waves. In the shear mode, all fibres buckle in the exact same way, looking like stacked sine waves.

Fibre kinking is a highly localized form of fibre buckling and occurs after the micro-buckling

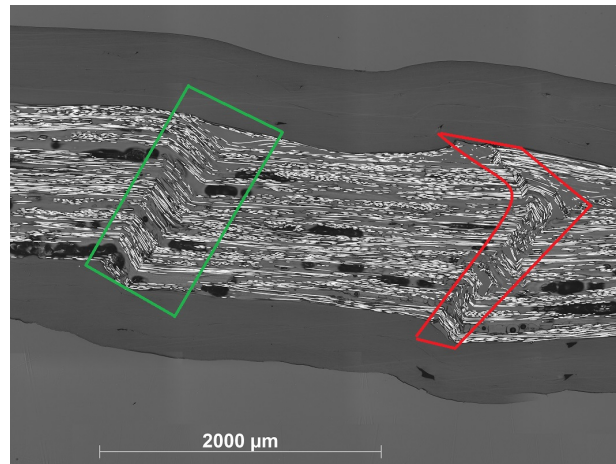


Figure 4.14: Failure of the compressive specimen in the x-y plane. The left kinked area is shown in green, the right kinked area in red.

has already started developing. Usually there are two or more areas where fibre kinking occurs, and the area between these is plastically deformed.

Transverse tensile rupture is a rupture in the fibre direction and occurs due to large Poisson strains inside the material. Since in fig. 4.14 shows two areas with highly localized fibre buckling, the failure mode here was assumed to be fibre kinking.

When taking a closer look at both the buckled areas, it was observed that in the left area all fibres buckled in shear mode, whereas in the right area this is not the case. Here most of the fibres are buckled in shear mode, meaning all the fibres buckle in the same direction. In the red area of fig. 4.14, a few fibres buckled in extension mode, meaning they buckle in the opposite direction of the fibres next to them. Another interesting fact is that the right buckled area is arc shaped whereas the left buckled area is more or less rectangular. These shapes are encircled in fig. 4.14 in red and green respectively.

A reason why this might have happened is because the few fibres that buckled in extension mode did not have the space to buckle in shear mode. The already in shear mode buckled fibres took up a lot of space, resulting in buckling in shear mode would have costed the material more energy. These fibres thus buckled in extension mode to reduce the energy of the material.

When taking a look at fig. 4.15, which is the x-z plane of compressive coupon, the compression fracture in a single CFRP layer can be seen. Here several things can be observed, with the most obvious being that the fibre failures began at two different locations near the wall layers and moved inwards. A second result is that there is a gap as well as void area existent in between the two wall layers on the top of the image, again proving that the assumption made previously was incorrect.

A close up of the fractured fibres can be observed in fig. 4.16. This close up was taken from fig. 4.15 and is encircled in green. Here it was observed that the fibres bend and buckled due to the compressive force and finally fractured. It looks as if most of the broken fibres ended up almost perpendicular to their original orientation, but this might have been caused by the grinding and polishing processes.

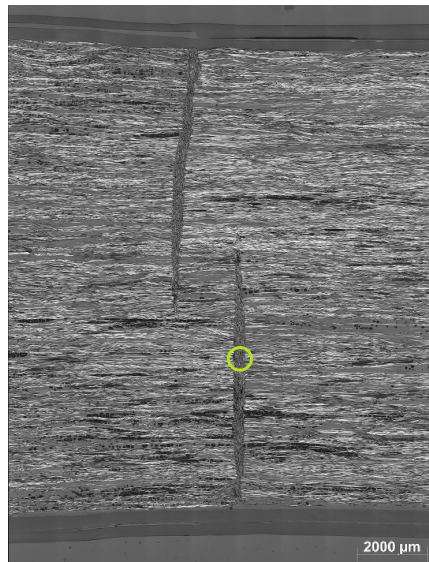


Figure 4.15: Microscopic view of a compression test coupon in the x-y plane. The green circle indicated the location of fig. 4.16.

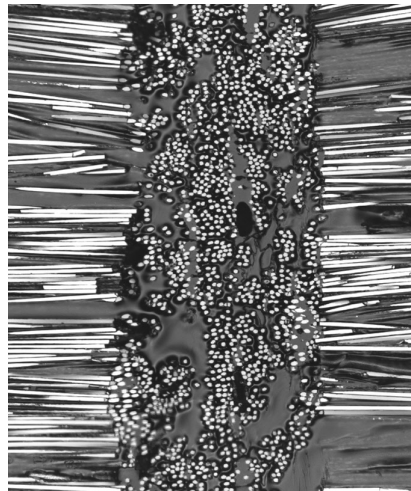


Figure 4.16: Zoomed in view of the failed area in the x-y plane. It can be seen that the fibres kinked into one single direction and finally breaking.

Another interesting observation made from fig. 4.14 was that the void areas seem to be wider in the compression coupon compared to the tensile coupon. This suggests that the voids are increased in size when a coupon is loaded under compression, compared to when loaded in tensile. Due to this increasing void volume, the coupons will fail more easily in compression than in tensile.

When comparing the results from the compression test with these microscopic images, several conclusions can be made about the compression test results. One of the reasons why the stress-strain curves of the compression test become unstable around a compressive displacement of 0.3 mm until finally failing around a displacement of 0.4 mm is because in this part the fibres are buckling, while the matrix material does not give the fibres enough room to buckle. When the matrix is deformed enough for all fibres to buckle, the

coupon fails in compression.

This also indicates why the compressive strength of the coupons is a lot lower than the tensile strength of the tensile coupons. In tension the fibres carry all the load, meaning the tensile results are fibre dominated. In compression, the fibres are much more dependant on the matrix material to keep them from failing, resulting in the compressive strength being a more matrix dominated property than a fibre dominated property.

Furthermore, any voids near the fibres (fig. 4.13) will have more impact under compression than under tensile loads, since under compression it already allows a fibre an extra degree of freedom to buckle.

4.6.3. Bending test discussion

For the bending coupons, fig. 4.17 shows an overview picture of the B1 bending coupon. It was observed that the coupon failed in tensile, due to a fracture having developed from the bottom, which is where the tensile stress is at its highest. This fracture can be seen more clearly in fig. 4.18.

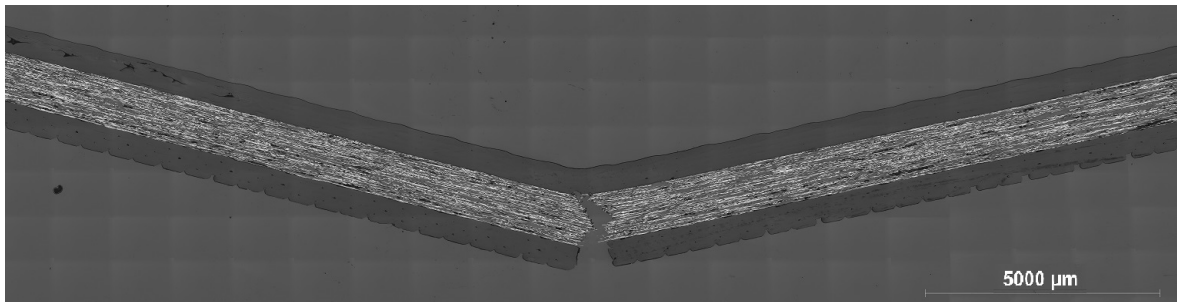


Figure 4.17: Microscopic image of the B1 three point bending test coupon.

It was interesting to observe that, even though the three point bending coupons have not been clamped in any way, the nylon layer still shows irregularities on microscopic level. These irregularities are the result of a discontinuous deposition or a too high cooling rate, not allowing the material to flow the appropriate amount.

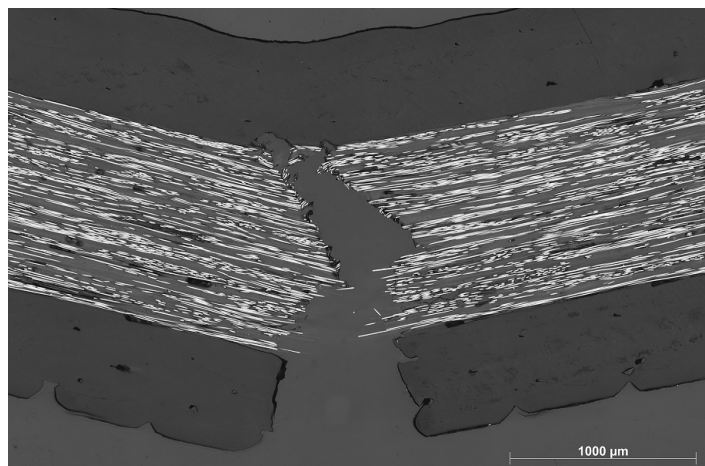


Figure 4.18: Failed area of the B1 sample - zoomed in view.

When comparing the tensile fracture image with the bending fracture image, it can be observed that the tensile fracture is very brittle, while the bending failure seems more ductile. By imagining reconstruction of the two parts of fig. fig. 4.18, it seems that the bending coupon will have a perfect fit when re-attached, whereas this was not the case for the tensile coupon. Reasons for this can be that parts of the fibres were completely shattered by the elastic energy released during the fracture of the tensile coupons, but that there was limited elastic energy stored in the fibres in the bending coupon.

That less elastic energy was stored in the sample was observed when comparing the stress-strain graphs of the tensile and bending mechanical tests with one another. For the tensile coupons the elastic strain is at 1.2 % when final failure occurs. For the bending coupons, the elastic strain stops at roughly a 1.5 % flexural strain, however, this is the strain in the outermost layers, which are not the fibre reinforced layers. The fibre reinforced layers are in the center of the sample and carry at maximum 0.75 % flexural strain, resulting in less elastic energy stored in the fibres.

Another observation was that the flexural strength and tensile strength are roughly 160 *MPa* and 410 *MPa* respectively. For a perfectly isotropic material, the tensile strength and flexural strength should be equal.

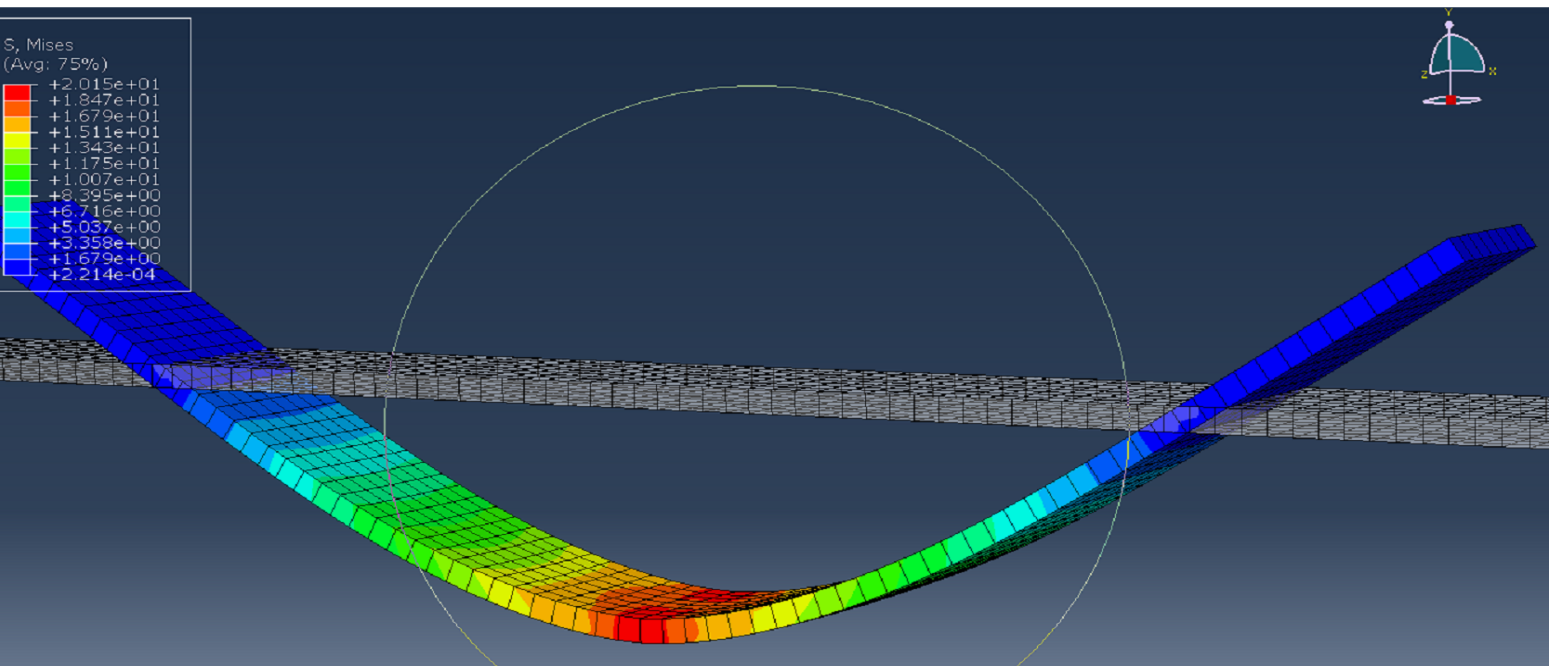
Since the material is a composite, this rule does not apply, since the outer layers are made of nylon, which is not the ideal material for carrying the highest loads. For a very stiff bending specimen, the fibre reinforcements should be on the outside and the nylon in the center to create a sandwich panel construction.

A second reason why the tensile and flexural strengths are different is that, in contrary to a tensile coupon, the location of the voids in a bending coupon have a larger impact. In a tensile coupon, the load is more or less equally divided over the cross-section, where in a bending coupon the stresses are the highest the further away one moves from the central line of the sample. So the voids located on the outside have a larger impact than voids located in the center of the coupon.

Another problem is that the carbon fibres are brittle when the forces are perpendicular to the fibres. The fibres will carry most of the flexural stress, but will fail prematurely due to the bending moment. The point where the fibres start to fail is the point where the bending stress-strain graph is no longer linear. When the remaining fibres can no longer carry the tensile load, the coupon fails.

5

The Abaqus/CAE® Models



Numerical models were constructed in Abaqus/CAE® to predict the mechanical behaviour of the coupons created for this research. The experimental data obtained in chapter 4 was used to validate the accuracy of the models. First Abaqus® will be briefly discussed. Second, the assumptions, used for creating the models, will be presented as well as the input values for the different models. Third, a nylon model was created, which was later extended to a carbon fibre reinforced model. Finally a short comparison between the simulation results and the mechanical test results will be displayed.

5.1. The Abaqus® environment

Abaqus/CAE® is a powerful software tool for simulating various engineering problems involving e.g. vibrations, thermal effects, and impact loading. The program requires a few steps to be completed to successfully simulate a model. These steps are:

- Creating one or more parts

- Supplying material data
- Create an assembly
- Define steps for the simulation
- Assign interactions between parts
- Define loads and boundary conditions
- Assign a mesh
- Create a job file

These steps will be briefly described and discussed. The simulation file of the nylon sample will be used to explain the above steps. Most of the information provided by each of these steps has been obtained from the abaqus® manual.^[66]

5.1.1. Creating parts

The user is free to choose to create the parts in abaqus® itself, or to import the .CAD images from another 3D CAD software package. Each part can be of a different element type and each type has its own code. The most used element types are: S4R, C3D8R, B31, M3D4R, and C3D4. These codes stand for the family of the part, the number of nodes, and the type of integration. For example, S4R is a **S**hell **4**-nodes **R**educed integration and B31 stands for **B**eam **3**-D **1**st order interpolation. When creating a part, the user initially chooses between 2D and 3D elements, after which the choice is made between shell, solid, wire, or point shapes.

For the coupons used in this research, a solid C3D8 element was chosen, which stands for **C**ontinuum **3D 8** Nodes full integration. Continuum shell elements would have been faster to compute, but do not support through thickness stresses as solid elements do.

An important fact to note is how the chosen element type affects the accuracy of the model, as well as the time it takes to compute. This is schematically shown in fig. 5.1





Element type	Relative CPU time	Relative Cost per Increment per Element
 CAX4R	1.0	1.0
 CAX6M	1.2	2.91
 C3D8R	11.5	1.86
 C3D10M	22.5	5.83

Figure 5.1: comparison of computation time for specific elements in abaqus®.^[7]

An important optimization here is to select the appropriate element that has the best trade-off between accuracy of the model and CPU time. Fig. 5.1 shows that the CPU time increases by a factor 10 when a 3D element is chosen (C3D8R) compared to a 2D element type (CAX6M).

5.1.2. Supplying material data

The next step is supplying material data and assigning it to the designed part. The material data consists of elastic, plastic and failure data. In the nylon model, the elastic data consists of the Young's modulus and the Poisson's ratio of nylon assuming an isotropic material. One can also opt for an orthorhombic material, or to provide individual engineering constants. The plasticity data has to be obtained from test data. However, the data obtained from tests is the engineering stress and engineering strain which first has to be converted to the true stress and true strain via the following equations:

$$\epsilon_0 = \ln(1 + \epsilon) \quad (5.1)$$

$$\sigma_0 = \sigma * (1 + \epsilon) \quad (5.2)$$

,where σ_0 and ϵ_0 are the true stress and true strain respectively, and σ and ϵ are the engineering stress and engineering strain respectively. This plastic data does not yet model the damage. The failure data has to be individually supplied and can be done through various methods depending on the type of material used. In the case of the nylon sample, damage for ductile materials was used. The data that needs to be supplied depends on the type of failure model chosen.

Finally, the material data has to be assigned to the desired parts or sections of parts. For the nylon model, the nylon data was assigned to the entire part. The elastic data was isotropic with a young's modulus of 940 *MPa* and a poisson's ratio of 0.3. The plastic data was obtained from the nylon tensile test data.^[8] The material data used for the coupon simulations will be listed in the specific section.

5.1.3. Creating assembly and assigning interactions

Even when the model only consists of one part, an assembly of parts has to be created. In the assembly all the individual parts of the model are combined. If the model consists of multiple parts interactions have to be implemented between these parts. These interactions are e.g. contact forces, welds, and fluid contacts. In the case of the nylon model, only one part needs to be modelled, resulting in no interactions necessary. In case of the fibre reinforced sample, the fibres will have to be embedded in the matrix via the embed interaction option.

5.1.4. Define steps, boundary conditions and loads

Besides the initial step, in which the model initialization takes place, at least one additional step has to be created to be able to perform a simulation. The additional step(s) determine simulation time, defined by the number of step increments, as well as size of the increments. finally, the boundary conditions and loads are to be defined.

The boundary conditions can apply to the initial step, however loads require to start at one of the additionally defined steps. In the case of the nylon model, the boundary conditions applied are resembling the two clamps restricting movement of the bottom area in x-, y-, and z-directions, and of the top area in y-, and z-direction. Here the x-direction is the longitudinal direction, where y and z are the transverse directions. The loads applied are

both the clamping forces simulated as pressures, as well as the tensile load which has been chosen to be modelled as a displacement of 2 mm/min .

5.1.5. Assigning a mesh and creating the job

The final steps to create a model are to apply a mesh and to create a job. The creation of the job is straightforward, creating a file for the abaqus® environment to use to write results. Which results are written to the output file has to be defined manually. Possible outputs are von Mises stresses, Linear Elastic strains, and rotational transformations.

The defining of the mesh is a very important step, since the mesh type and its size determine the outcome and the time to complete a simulation significantly. If no mesh was used, the number of points would be infinite, which would require an infinite amount of equations to solve. Finite Element Analysis (FEA) uses meshes to make the number of required equations finite. Due to meshing, the number of points will become finite, resulting in a finite number of equations that need to be solved. In abaqus®, there are three types of mesh element types available. These are:

- Hexahedron shaped mesh
- Wedge shaped mesh
- Tetrahedron shaped mesh

Note that here the word element is used to describe the small volumes that the part is divided in, as can be seen on the image at the beginning of this chapter.

Which meshing element to use depends on the geometry of the part. The hexahedron mesh is the standard meshing option in abaqus®, but will not be able to cover complex geometries. For these, wedge or tetrahedron meshes are better suited. A hexahedron mesh has the highest accuracy of these mesh types, due to having 8 vertices, 12 edges and is bounded by 6 faces. The computation time compared to the others is however, slightly higher. Due to the higher accuracy and the increase in computational time was negligible, the hexahedron mesh was applied to the nylon tensile model.

Once the mesh is applied, the meshing controls can be assigned, where the options about types of integration and element deletion can be set. The types of integration are full and reduced. The reduced integration only uses 1 integration point per mesh element instead of the 4 integration points used with full integration. This makes the full integration more accurate, but also more computationally expensive.

The element deletion option can be used when simulating a model that includes damage creation and propagation. When an element is damaged to a point that it can no longer carry any load, it will be removed from the simulation. The negative effect of element deletion is that by deleting these element, energy gets removed from the system. This is very important for impact analyses and is one of the reasons why these types of simulations are sometimes under-predicting the actual mechanical performance. In the models constructed for this research, the element deletion is not used, due to the added inaccuracy to the models. The nylon model does still have the plastic data enabled, whereas for the composite samples this data has been left out. It is of course more accurate to simulate with the data, but the simulations would become too time consuming.

5.2. The nylon sample

As a first stage a nylon model was created that would represent the nylon coupons tested by van der Klift et al.^[8]. The stress-strain curve of a tested nylon sample is shown in fig. 5.2.

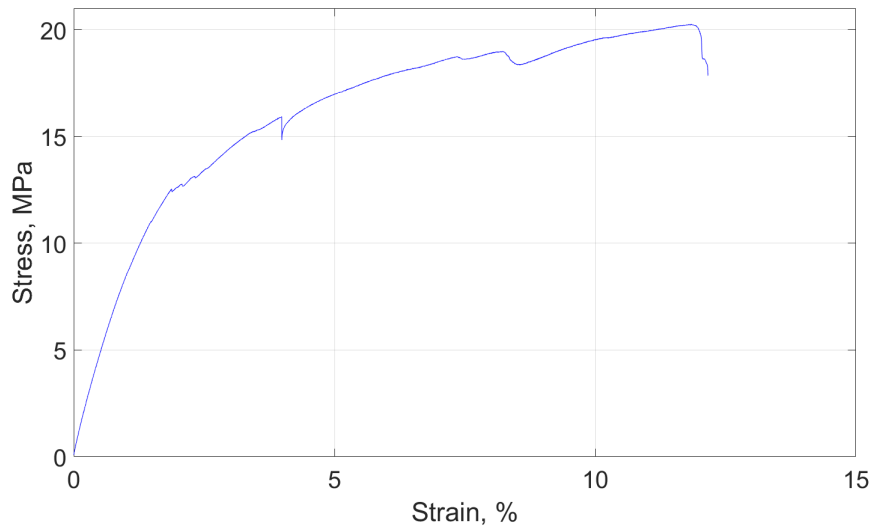


Figure 5.2: Stress-strain curve of a nylon coupon tested in tensile.^[8] The inconsistencies in the curve can be ignored and are related to the machine malfunctioning.

The data, used to generate this plot with, was used to determine the elastic and plastic response of the material and implement this in the abaqus[®] software. The elastic material properties entered were: A young's modulus of 940 MPa and a poisson's ratio of 0.3. The plastic data was obtained by subtracting the elastic stress and elastic strain from the total stress and total strain. The plastic behaviour occurred at a tensile stress of roughly 12 MPa . The nylon model simulated a tensile test with as input a displacement of the top clamp of 2 mm/min until reaching the failure strain at roughly 12 %. Fig. 5.3 shows the results of three the same models which all have different mesh sizes. Even though the models look different in size, this is not the case and all models have equal dimensions.

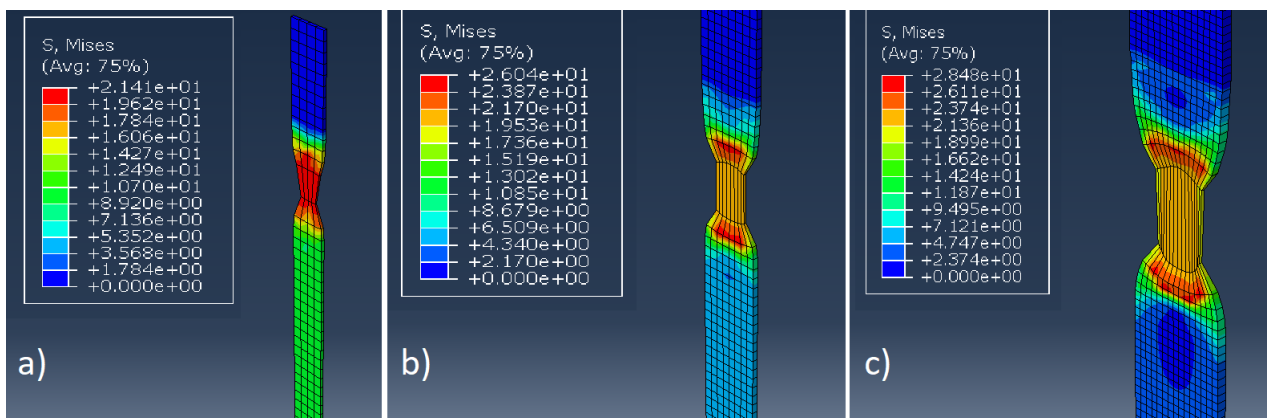


Figure 5.3: Three models with different mesh sizes. a) 4 mm per mesh element, b) 2 mm per mesh element, and c) 1 mm per mesh element.

When comparing fig. 5.3 a, b, and c with the graph from fig. 5.2 it can be seen that the model

with the 4 mm per mesh element has a maximum stress of 21.4 MPa which comes the closest to the stress-strain curve data where the max is roughly 20 MPa. The finer mesh sizes give equal results, but do show increased stresses at certain locations that reach 26 MPa in case of the 2 mm per mesh element and 28.5 MPa in case of the 1 mm per mesh element models.

The 4 mm per mesh element model does, however, not depict the plastic behaviour well enough, whereas the other two models show a significantly different plastic deformation. Also in terms of computation time, the 4 mm and the 2 mm mesh size models did not differ very much, whereas the 1 mm mesh size model took almost twice as long as the other ones.

5.3. Simulating the coupons

To upgrade the nylon model to a composite model, the fibre bundles have to be added. In abaqus® this can be done in various ways. The first method is to model the fibre bundles individually as separate beam elements and embedding these in the nylon matrix material. This is a very accurate method, but is very computationally expensive especially for bending models due to the more complex fibre loads and displacements.

A second method is to model the reinforced bundles as one composite material and treat this as an embedded solid. Even though this technique is inaccurate, it at least is possible to perform simulations within a short period of time.

A third option is to model the whole part as a composite lay-up and not treat the nylon as a homogeneous material. Although this is more accurate than the second option in terms of the nylon material, it only proves to be handy for simple geometries and a small number of layers. More complex shapes, or parts with a lot of layers, will take a lot of time and effort to model and simulate in this way. Because of all the above named reasons it was chosen to model the nylon as a homogeneous solid (as was also done in the nylon models) and model the carbon fibre bundles as a CFRTP solid, embedded in the matrix.

In order to simplify the models, several assumptions were made. The assumptions made for the models are:

- 1 Nylon is modelled as isotropic material
- 2 Carbon Fibre bundles are modelled as orthotropic solid
- 3 Voids are assumed to be only in the carbon fibre reinforced layers
- 4 Voids are assumed to be equally distributed over the sample.
- 5 Perfect adhesion between layers
- 6 CFRP material properties 4x lower in compression model than in the other models

Already in the discussion of chapter 4 it was proven that three of these assumptions, namely the numbers 3, 4 and 5, are incorrect. These assumptions were still implemented in the

Table 5.1: Carbon fibre material values used as input for abaqus[®] simulations.

Matrix property	D1111	D1122	D1133	D2222	D2233	D3333	D1212	D1313	D2323
Value [MPa]	30089.6	0.4830	0.4830	1233.6	0.4830	1233.6	557.8	557.8	858.1

models in order to not make them too complex and computationally expensive.

As a mesh size the 2 mm per mesh element were used due to increased accuracy of the models. The 2 mm mesh size models have a whole element in the thickness direction of the samples, increasing accuracy when compared to the 4 mm per mesh element models. The 1 mm mesh size models proved to be more computationally expensive. An exception had to be made for the bending simulation, which was performed on the student edition of abaqus[®]. This edition can only simulate up to 1000 nodes.

Since the results of the mechanical tensile test showed that the carbon fibre reinforced nylon coupons behaved linearly (see fig. 4.4), it was opted to only model elastic data into the model. The nylon was once again modelled with a young's modulus of 940 MPa and a poisson's ratio of 0.3. The orthotropic material data of the carbon fibre reinforced areas is displayed in table 5.1. The voids were modelled by reducing the values of the stiffness matrix by the percentage of the total void area, which in chapter 3 was calculated to be 7.33%. The deduction has already been applied to the values from table 5.1. The D1212, D1313 and D2323 values, which are the shear moduli, could not be determined algebraically and were assumed to be a function of the tensile modulus and the Poisson's ratio.

The coupons consist of 16 layers each, of which the top and bottom four are made of nylon. Besides these floor and ceiling layers, there are also 0.8 mm thick wall layers on both sides of the sample. The center 8 layers were given the carbon fibre properties. Fig. 5.4 is a schematic image of the cross-section including material assignments.

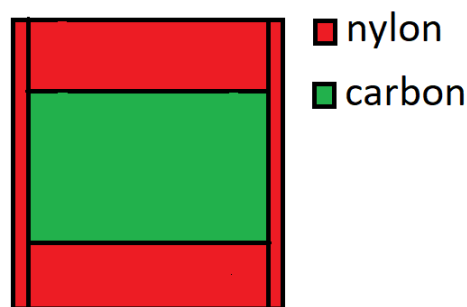


Figure 5.4: Sketch of the cross-section of a modelled coupon. The different areas represent different types of layers, these are: nylon (red) and carbon fibre reinforced (green).

The results of the tensile, compression, and bending coupon simulations are shown in figs. 5.5, 5.6, and 5.7 respectively. The tensile and compression simulations show only one of the carbon fibre reinforced layers, whereas the bending simulation figure shows the entire simulated model. In all cases the whole model was simulated. Again all the simulations have the displacement as input and are stopped when the displacement reaches the value where failure occurred in the mechanical tests. The displacement input values are 2 mm/min for

the tensile simulation, 1 mm/min for the compression simulation, and 8 mm/min for the bending simulation.

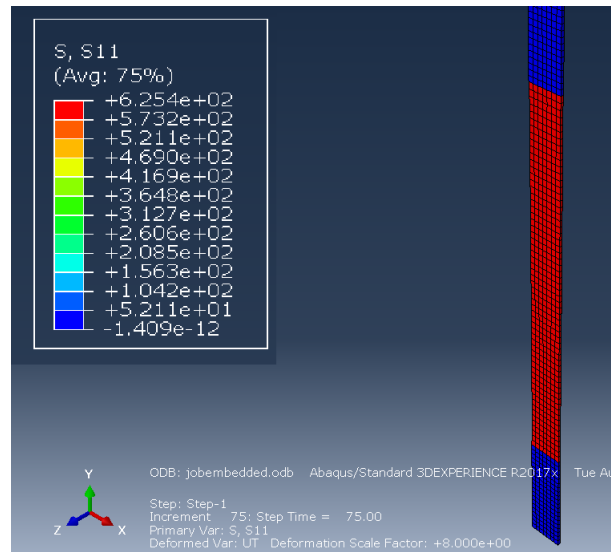


Figure 5.5: Simulation results of the tensile coupon in abaqus®. The maximum stresses observed are 625 MPa

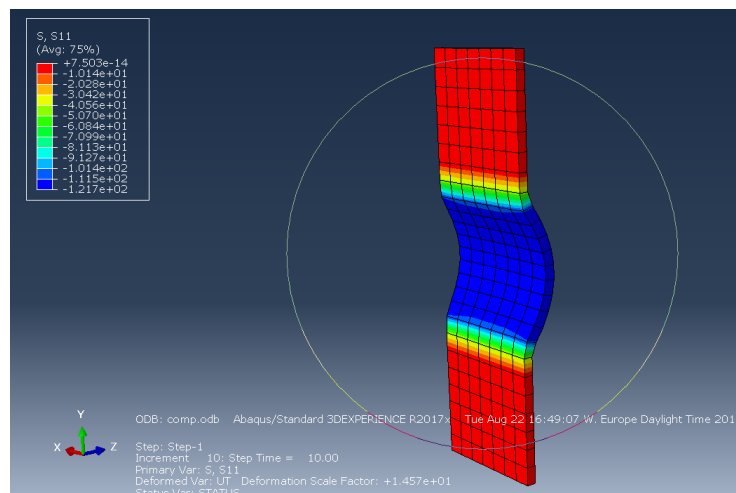


Figure 5.6: Simulation result of the compression coupon in abaqus®, showing a maximum compressive stress of 122 MPa .

When comparing the simulation results to the test results, mismatches are found. The results of the mechanical tests and the simulation results are shown in table 5.2 together with the mismatch found between the two. It was observed that the compressive model came close to the actual mechanical results. The tensile simulation is over-estimating the maximum by roughly 53 %. The bending model is very far off from the mechanical results, but comes close to the actual tensile result of 409 MPa .

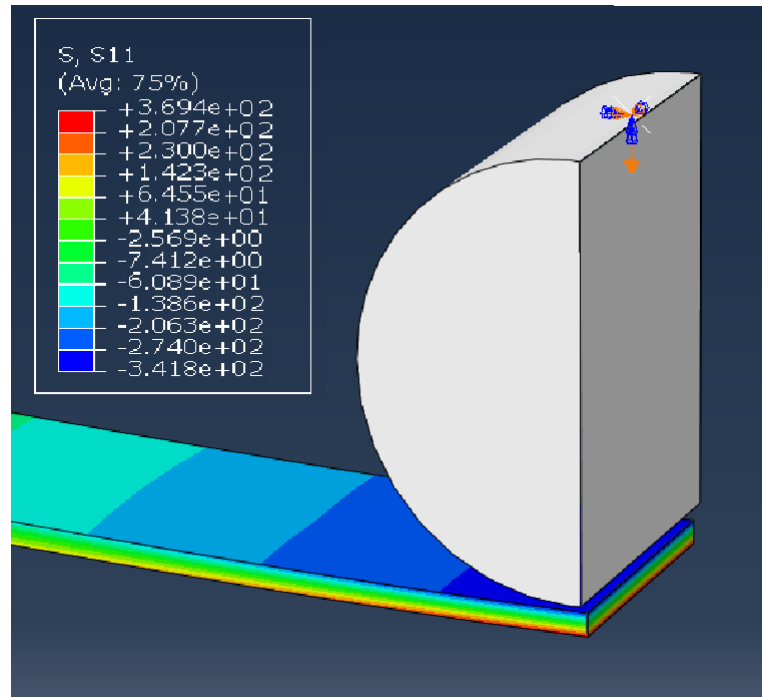


Figure 5.7: Simulation result of the bending coupon in abaqus[®]. Maximum stress observed was a tensile stress of 370 MPa.

Table 5.2: Comparison between mechanical and simulation results.

	Mechanical Result [MPa]	Simulation Result [MPa]	Mismatch [%]
Tensile	409	625	52.8
Compression	110	122	10.9
Bending	144	370	156.9

6

Designing the aircraft part



This chapter will discuss the design and test phase of the aircraft part. First the designs as well as simulations on these designs will be shown, after which the final part is displayed. This part will then be tested to see if the part is indeed as strong as the simulations say it is.

6.1. Designing aircraft parts

By using Abaqus and Eiger[®] an aircraft part was designed to determine if it is possible to 3D print functional aerospace parts. Two parts were selected to look at. The first part is a torque link for a helicopter. The second part is a chair bracket used in air plane passenger chairs. Both parts are designed by first making a 3D drawing in Abaqus, after which the .stl-file is exported to Eiger[®] to see if the desired fibre placement can be achieved. Then the part will be simulated in Abaqus to test if the stresses are within the limits of the material. For these simulations, the results from chapter 4 and chapter 5 will be used for validation.

6.1.1. The Torque Link

A torque link is a typical example of a part with complex stresses and was thought to be an ideal feasibility test for the MarkForged[®] 3D printer. A first design is shown in fig. 6.1 which is a close replica to the design used in a previous paper from the Dutch Aerospace Center, where a composite torque link was designed by making use of the resin transfer moulding (RTM) technique.^[9]

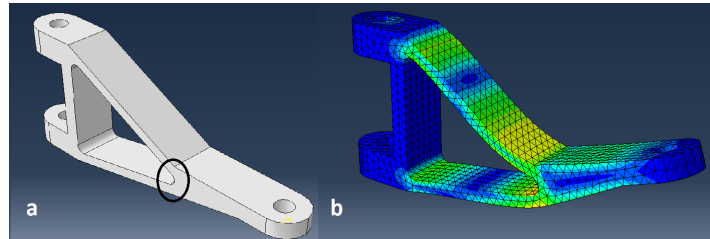


Figure 6.1: Abaqus model of nylon torque link as designed by the NLR^[9]. Figure a shows the unloaded state, figure b shows the stresses when an upward load is placed on the hole on the right. The brighter yellow the colour, the higher the stresses.

The main issue with this design is that the fibres will never be in the ideal directions for both principal stresses, because the two areas where the highest loads are, are not in a single plane (see part b of fig. 6.1). The only way to be able to print this part with continuous fibres in the optimal directions, is by printing the part sideways. This does create another problem, which is delamination due to high stresses in the encircled area in part a of fig. 6.1. To avoid the delaminations and still be able to lay fibres in the critical areas, it was chosen to create the torque link out of two separate parts. One bottom and one top part, which are shown in fig. 6.2.

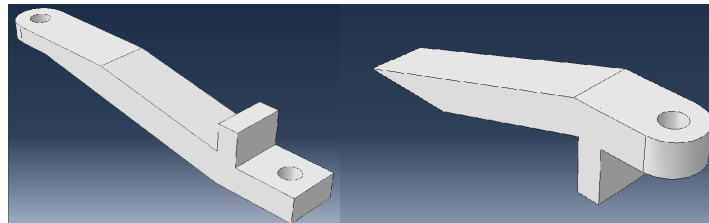


Figure 6.2: The NLR torque link model^[9] consisting of two components. Fig. a shows the bottom part, fig. b shows the top part.

When printing both of these parts under a different angle, the optimal fibre direction can be obtained. The two parts can be mechanically or chemically bonded in many different ways, where glueing would be the most preferable option. An issue in this case are the limitations of the Eiger[®] software program. It is required to have at least 1 layer of nylon at the top and bottom of each part, which means the glue will be between two nylon layers, which will form a relatively weak area in the part.

Because of these reasons it was concluded that it is yet too early for this technique to be able to successfully print a torque link with continuous unidirectional fibres. Another, more geometrically simple part had to be chosen, which was the chair bracket.

6.1.2. The Chair bracket

A chair bracket, shown in fig. 6.3, is originally made from aluminium and has as task to support the back frame of the chair. In total two of these parts exist in a single chair. The dimensions of the part are 190 by 70 by 5 *mm* in length, width and thickness respectively.

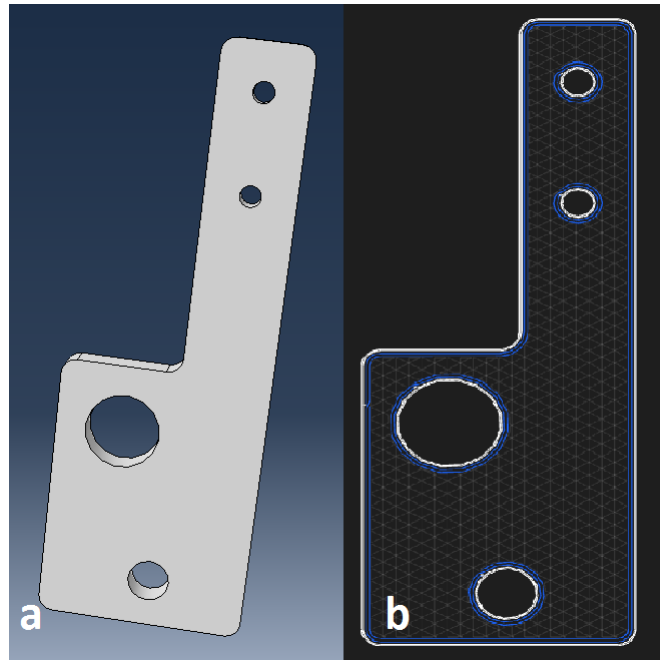


Figure 6.3: a) The chair bracket design made in Abaqus. The back frame is attached to the two small holes. The other holes are for fixing the chair bracket to the rest of the chair. b) shows the same part in the Eiger[®] software with the fibres in blue.

The frame of the back of the chair is mounted on the two smaller holes and the bracket should be able to hold the back frame in place and transfer all the loads without failing. In order to achieve this, five concentric fibre rings were placed both the outer and inner walls. The outer wall reinforcements were to give the part the mechanical properties it needs to carry the load, the inner walls (the holes) are reinforced to prevent hole tear-out. The way the fibres are placed is shown in fig. 6.3 b. This extended part where the chair of the back is mounted on is 100 *mm* long and 30 *mm* wide.

Design One

When simulating this specific chair bracket with a design load of 1500*N* at the top of the back panel, which amounts to 750*N* carried per bracket, the results, shown in fig. 6.4 showed that the bracket would fail in both tensile and compression. This is due to the maximum loads in tensile and compression exceeding the 409*MPa* and -110 *MPa* respectively, with the main issue being the compressive load of -322.9 *MPa*. However, the simulations performed in chapter 5 showed that the tensile simulation results are 53 % higher than the mechanical test results, and that the compression simulation results were 11 % higher than the mechanical test results. When compensating for this, the tensile and compression stresses in fig. 6.4 become 327.5 *MPa* and 290.9 *MPa* respectively, only resulting in compressive failure.

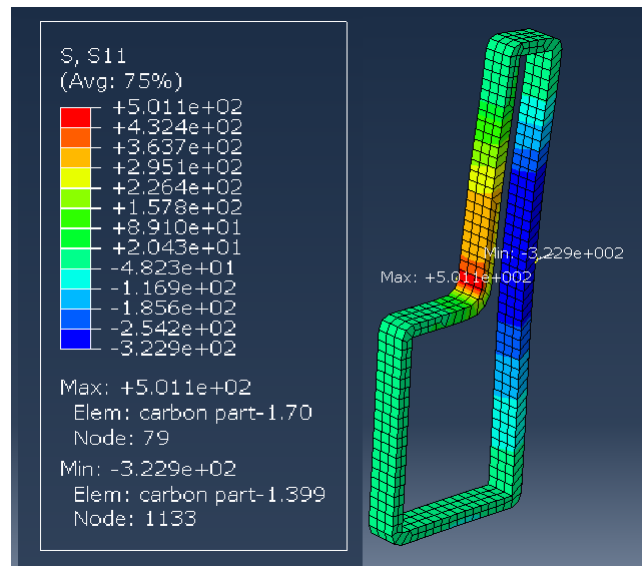


Figure 6.4: Abaqus simulation result of the original chair bracket design tested with a 750 N load per bracket applied to the top of the back panel of the seat. It can be seen that especially the compressive load is a factor 3 too high.

The stresses on the inner reinforcements were also checked and it was observed, with a more primitive model shown in fig. 6.5, that these stresses are well below the stresses in the outer reinforced ring. For this reason, the inner reinforcements were still included in the simulations, but are not shown in future results.

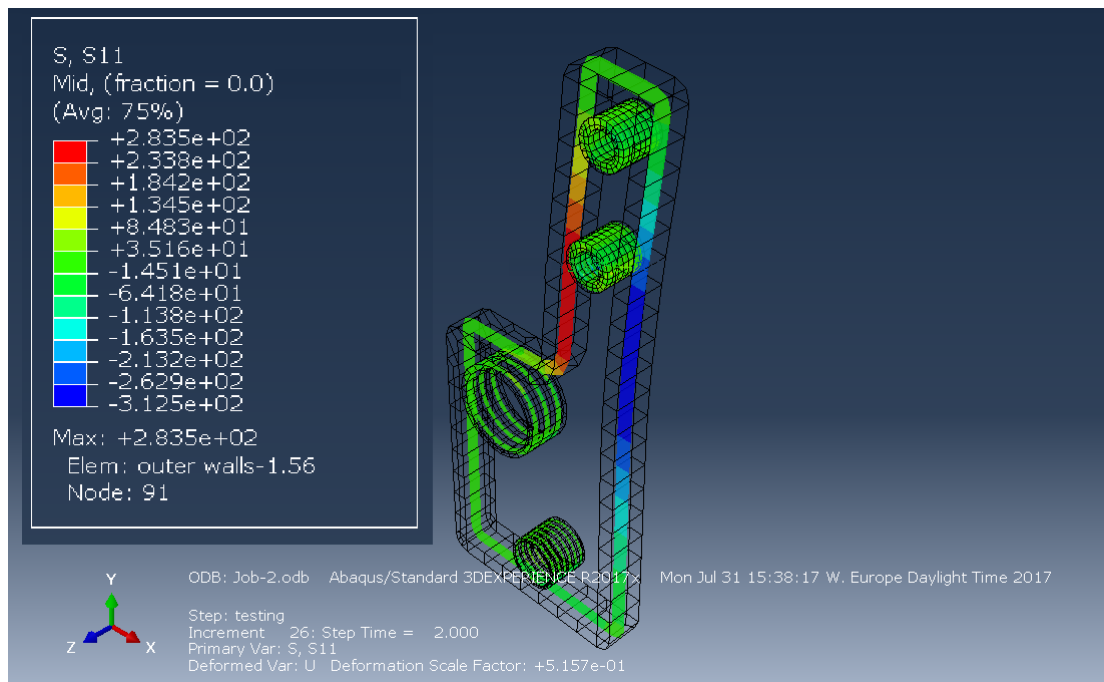


Figure 6.5: Abaqus simulation result of a primitive model showing where the stresses are located. The highest tensile and compressive stresses are located in the outer reinforced ring.

Another design limit was the price being at maximum 250 Euro. This part is just below that limit, with a cost of 232.58 Euro. This means that adding any more material will make it go

over the cost limit. Since the chair bracket is not a critical part, it is possible to remove the safety factor. Doing so, the resulting compressive stress would still be -145.5 MPa , which is roughly 35.5 MPa too much. Other designs had thus to be implemented. For these other designs the figures will show the uncorrected stress values, while the compression values will already be corrected in accordance with the results obtained in chapter 5.

6.1.3. Other designs for the Chair

In total three other designs were created. These designs were all created without any focus on topology optimization, since that is outside of the scope of this research.

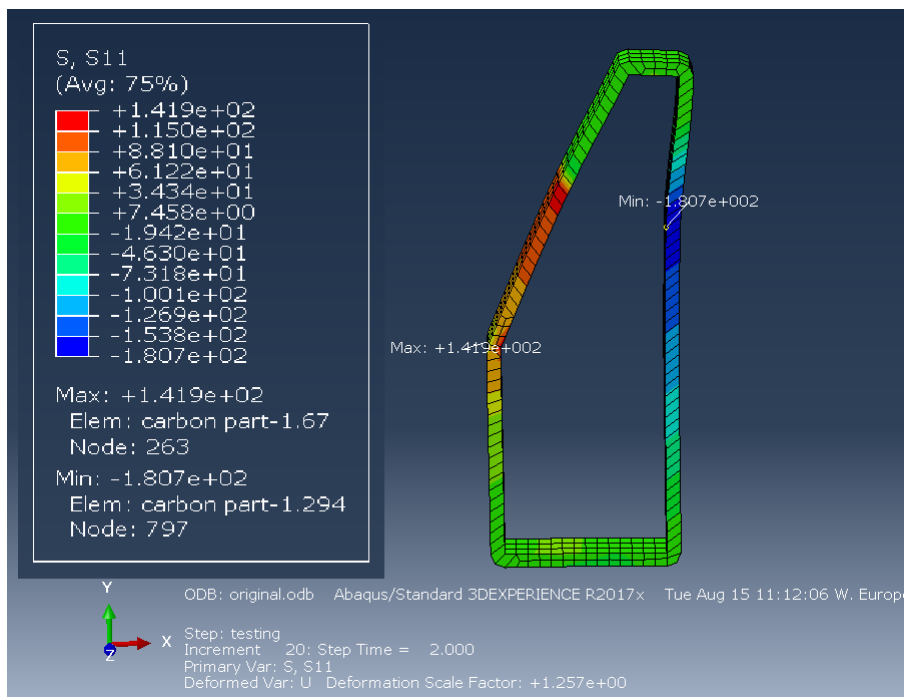


Figure 6.6: Design 2 of the composite chair link. The dimensions are still the same, but the geometry has changed. The minimum stress is reduced to -162.8 MPa , but the costs went up to 400 Euro.

Design 2

Fig. 6.6, was fully focussed on reducing the compressive stress by increasing the width of the area where the moment is the largest. This reduced the compressive stress to -162.8 MPa , but the costs rose to 400 Euro due to more material being used. Also, since the geometry changed, the chair bracket no longer fits inside of the chair frame and has to be mounted on the outside of the chair frame.

Design 3

To try and reduce the costs, regions that do not carry any loads, like the bottom left corner, were removed as is shown in fig. 6.7. Also a small stroke of material was removed from the right side. The costs dropped to 360 Euro, but the compressive stress increased to -173.9 MPa .

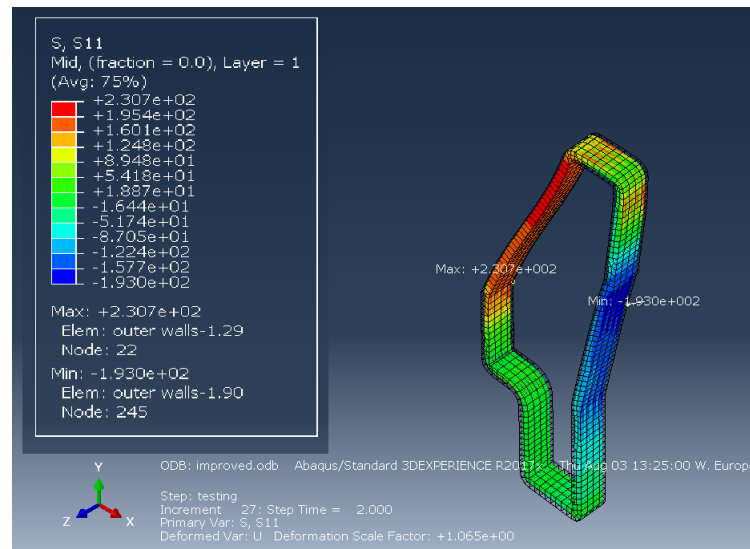


Figure 6.7: Design 3 decreased the costs to 360 Euro but the compressive load rose to -158 MPa .

Design 4

Design number 4 was created to decrease the amount of material used as well as lowering the compressive stress. The result of this is shown in fig. 6.8 with a maximum compressive load of -145.9 MPa and a price of 340 Euro.

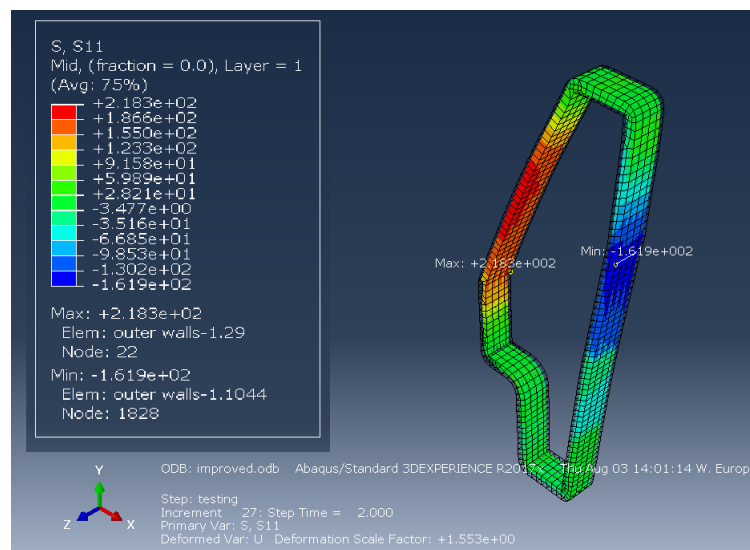


Figure 6.8: With the third redesign, the compressive load dropped to -145.9 MPa The costs however, were 340 Euro.

Since the costs are a hard constraint, it was chosen to remove the safety factor in order to be able to lower the force acting on the chair frame to 750 N in total, which equals a load of 76.43 kg pressing against the back of the chair, which can be seen as the force that a slight obese male adult would exert. The removal of the safety factor is allowed since the part is a non-crucial component of an aircraft. The failure of this part is not desirable, but will not cause the air plane to malfunction.

With this load, the amount of reinforcements could be changed. It was chosen to leave the part the same thickness as in design number 4, shown in fig. 6.8, which equals 120 layers, of which at maximum 112 can be reinforced. It was chosen to reinforce 60 layers, 30 layers on the bottom of the part and 30 layers on the top of the part. This type of reinforcement would be adequate to support the load according to the simulation results. The printed part is shown in fig. 6.9.



Figure 6.9: Final part as printed by the Mark Two[®]. It can be seen that the bottom 30 and top 30 layers are reinforced. The costs of this part are 248 Euro.

The costs of this part also fell under the 250 Euro, though attempts were made to lower the costs even more by removing material in the center, that is not of any structural importance. However, it was discovered that the Eiger[®] software automatically reinforces the newly created inner walls, raising the costs again. Sadly there is no option in Eiger[®] available to manually select which walls to reinforce.

6.2. Testing the chair part

In order to test the chair bracket, it first had to be mounted to a stiff surface, after which an arm, acting as the chair frame, had to be attached. The test set-up on which an aircraft chair frame was tested was used for this research, but had to be slightly modified in order to fit the chair bracket on.

A part of a chair frame that was still available was used so that it was not needed to manufacture a new arm on which the load had to be applied. This chair frame part is not completely straight, so will induce a slight moment when the load is applied. This moment is not present when the chair frame is mounted on both brackets, since it will be cancelled out. The torsion moment that was created during the test amounted to 22.5 Nm and is relatively small when compared to the bending moment of 251 Nm . Fig. 6.10 shows the test set-up.

Two bolts were used to mount the chair bracket to a steel plate, which in turn is mounted to the frame of the set-up with four bolts. The arm was connected to the chair bracket by two bolts. It turned out that one of the holes of the chair bracket did not completely align with the holes in the arm, which might have been caused by the MarkForged[®] 3D Printer. Because of this, smaller bolts had to be used in order to fit the arm onto the chair bracket.



Figure 6.10: Test set-up for testing the 3D printed chair bracket. The bracket is mounted to a steel plate by two bolts. The metal part at the end of the arm is used to hang the load on.

One of these smaller M4 bolts was at a slight angle in order to fit.

The load was applied by hanging a pendulum at the end of the arm, on which weights would be placed. Since a static load of 375 N was required, a total of 38.21 kg had to be used. The pendulum in combination with the metal grip used to attach the pendulum to the arm combined to 1088 grams . Since the smallest weights available were of the order of 2.5 kg a total mass of 37.5 kg was used to load the chair bracket. Fig. 6.11 shows the complete mechanism without any additional weights attached. The bracket is loaded under 10.68 N . A wooden board was placed under the pendulum to prevent the floor from being damaged in case of sudden failure of the bracket.



Figure 6.11: Complete test set-up. The weights can be stacked on the pendulum in order to increase the load on the bracket. A wooden board is placed under the pendulum to prevent any damage to the floor in case of failure.

The weights were added in steps of 2.5 kg and there would be a one minute pause before increasing the load again. After every step a picture was taken to clearly see the changes.

It was immediately observed that the displacement of the load was larger than expected. From an almost zero displacement at 2.5 kg to almost 20 cm under a load of 37.5 kg. Even though the displacement was disturbing, the part showed that it could hold a load of at least 375 N, as is shown in fig. 6.12.

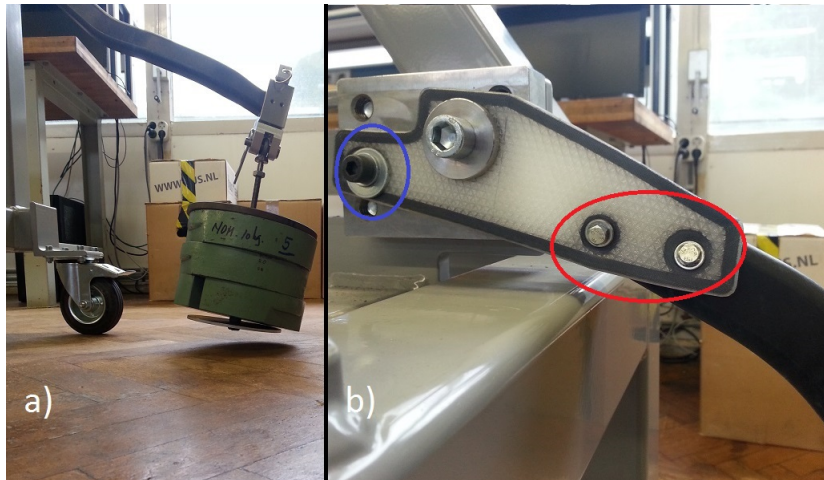


Figure 6.12: Final stage of the test. (a) A total load of 37.5 kg hanging from the pendulum. (b) The bracket under a load of 375 N. The arm is no longer in a straight position.

Fig. 6.12 part b) already shows the main issue being the two M4 bolts (encircled in red) that are supposed to hold the chair frame in place, as well as the smaller bolt (encircled in blue) that should stabilize the chair bracket in horizontal position. One of the issues, as mentioned before, is the misalignment of the holes. The damage done to the holes of the bracket is visible in fig. 6.13. Here it can be seen that the wall layer at the top of the second hole (encircled in red) is severely damaged by the M4 bolt.

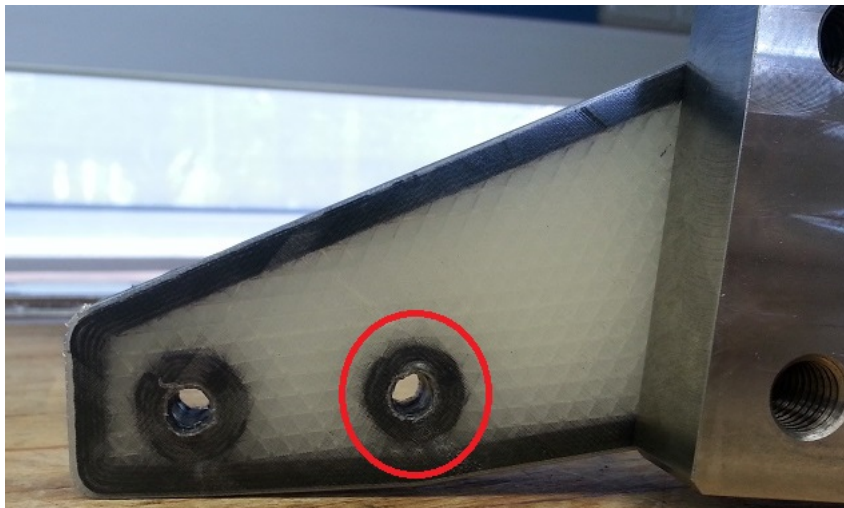


Figure 6.13: 3D printed chair bracket after testing. The bracket is still attached to the steel plate, but the damage to the pin holes (encircled in red) is clearly visible.

7

Discussion

In this chapter all the results obtained in the chapters 2 till 6 will be further analysed and discussed. Since there was already a partial discussion at the end of chapter 4 regarding the mechanical tests and the results of these, the mechanical test results will not be discussed in much detail here. Throughout this chapter recommendations for future research into this specific topic or into closely related topics will be mentioned. The final conclusion will be presented in chapter 8.

7.1. The printer

The MarkForged[®] 3D printers were the first commercial 3D printers that were able to print with continuous fibres. Because of this there are of course several flaws that have to be worked out of the system, but the Mark Two[®] shows a lot of promising features.

The printer is very easily installed and is almost immediately ready to use. The printer can print with various materials, which are also easily installed. The software is cloud based and can be accessed from any computer, so prints can be started even when the user is away from the printer. The printer maintenance is also very user friendly, so can the print head be dismounted for cleaning and repairs in case needed.

However, there are some disadvantages to this printer as well, which are mostly software related. First of all, the Eiger[®] cloud based software is not open-source. This reduces the possibilities of the printer, since users are unable to tweak the software to improve the printer, nor can the code be read in order to understand the printing process better. Certain data that can be obtained from the code are e.g. the distance between fibre filament bundles, and what the exact material deposition speeds are. This information can both help the design process, as well as help understanding the printing process better.

Second, the software has some key features that are missing. One of these features is to be able to choose not to reinforce the entire layer, but only parts of it e.g. only the area to the right of the red line in the part from figure 7.1. Furthermore, this feature becomes important in case of designing parts with holes for bolts that also have additional holes with the purpose to save material, as shown in fig. 7.1. Here the pin-holes require reinforcements, but the gap (encircled in green) does not. The Eiger[®] does, however, not make this possible.

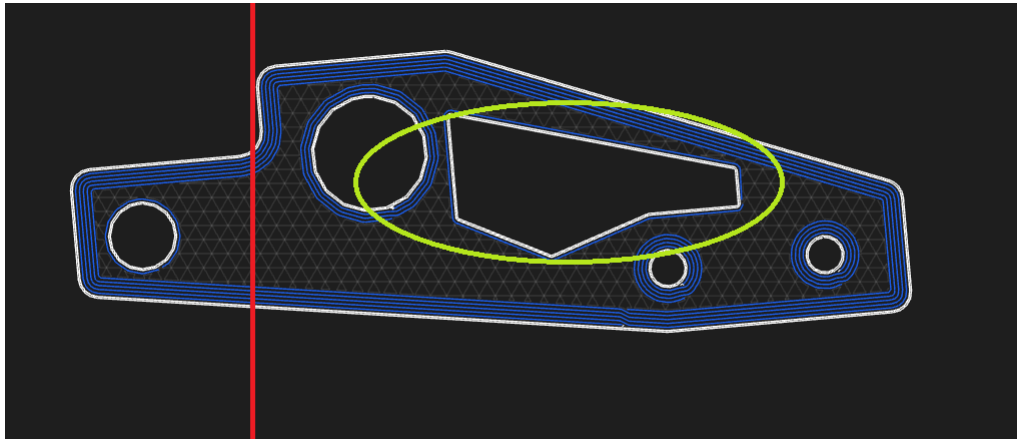


Figure 7.1: Part designed that needs to have only the outer walls and the holes for the pin connections to be reinforced. Sadly Eiger[®] will also reinforce the other gap, which was created in order to save material, weight, and costs.

Furthermore, there is no option to change the print head speed or to control the temperature. This means that the MarkForged[®] 3D printers are unable to print with other materials than the ones supplied by the company. This proves frustrating when higher strengths are required, considering the volume percentage of the carbon fibre filament from MarkForged[®] is only 34.5 %. The inability to work with other materials is also true if one wants to use other matrix materials, like PEEK, ABS or PLA. Polylactic-acid (PLA) and Acrylonitrile Butadiene Styrene (ABS) are the two most famous polymers used for matrix materials in many 3D printers, whereas Polyether Ether Ketone (PEEK) is a polymer that can maintain its mechanical properties at elevated temperatures, due to having a glass transition temperature at 240 °C.^[67] This makes PEEK a very interesting polymer for higher temperature applications.

Another disadvantage is the amount of discontinuities occurring from the deposition of the fibres. As was shown in fig. 2.17 a large discontinuity in the fibre layers was observed, which occurred due to the print head moving before the fibre filament had fully adhered. These discontinuities can be moved to an unloaded area in order to avoid premature failure, but this must be done layer by layer and will be very time consuming for parts with a high number of reinforced layers. Of course there are also designs in which this is not possible at all, resulting in a loss of tensile strength that can be as high as 33 %.^[8] This discontinuity is a lot smaller for the Mark Two[®] but is still existing in the parts.

Moreover, the technology that is used (FDM), also incorporates a lot of discontinuities in the part in terms of voids, which are visible in the microscopic images obtained in chapter 4.

Finally, a difference in dimensions was observed when comparing the dimensions of the printed coupons with the data from the Eiger[®] software. These dimensional inaccuracies were most likely caused by the thermal expansion of the matrix material, but these should have been accounted for by the company.

Now that the advantages and disadvantages of the Mark Two[®] are clear, it is useful to note how the printer actually prints. It has been stated before that a print can never start nor

end with a fibre reinforced layer. During the printing of a reinforced layer, the nylon wall layers are printed first. Note that the printer can not print with both nozzles at the same time. Either the printer prints matrix or fibre material. When printing the fibre filament, concentric rings are printed first, starting at the outer wall layers and moving inwards. In case isotropic fibre fill is selected, outer and inner concentric fibre rings are deposited before the isotropic fibres are deposited. Finally the printer fills up the non-reinforced parts of the layer with nylon, which can be either triangular fill, hexagonal fill, or rectangular fill. The printing of supports is performed just after the the wall layers are deposited.

Improving printer limitations

It was found that most of the limitations of the printer are software related, thus improving the software should be priority number one. It is not necessary to make the software open source, but at least the designers should be allowed to have more freedom in designing parts. This includes a temperature and velocity control, so that more types of matrix and fibre materials can be used by the printer. An interesting topic for future research would be to use a different printing head velocity and extruding temperature to see if this decreases the amount of void area in the samples, thus resulting in higher part quality.

Another way to improve the quality of the printed parts is by heating the print bed to an elevated temperature. By increasing the print bed temperature, the part is annealed during the printing, reducing the residual stresses in the material that might have been caused by e.g. warping. Right now the warping is countered by the stiffness of the fibres, but it still imposes residual stresses. The heating of the part might also reduce the total void area due to allowing the fibre filament resin material more time to flow into the voids before solidifying.

Alternatively, the parts can also be annealed in an oven post-printing in order to improve the mechanical properties due to reducing the residual stresses. This post-printing annealing will thus both increase the costs as well as the production time of the parts.

The annealing processes should be performed at temperatures higher than the glass transition temperature, but below the melting temperature. A study on annealing isotropic nylon-6,6^[68] concluded that for dry nylon-6,6 annealing temperatures up to 150°C increased the tensile strength and modulus with annealing time, where the most significant changes were observed between 60°C and 100°C. At temperatures above 200°C the annealing process has a negative effect with time due to chain degradation.

Fig. 7.2 shows the tensile modulus versus the temperature of a semi-crystalline polymer, like nylon.

Here T_g is the glass transition temperature and T_m indicates the melting temperature. For nylon-6 the glass transition temperature is approximately 60°C^[10, 69] which is in accordance with the results obtained by Babatope *et al.*^[68] Above the glass transition temperature, nylon becomes a soft, ductile solid with a high strain to failure rate. When the temperature is increased, the secondary bonding forces diminish due to molecular movement and it becomes possible that adjacent chains can move when applying a stress.

The melting temperature of nylon is approximately 255°C. At this point the nylon becomes a liquid and the young's modulus drops rapidly as can be observed from fig. 7.2. Annealing

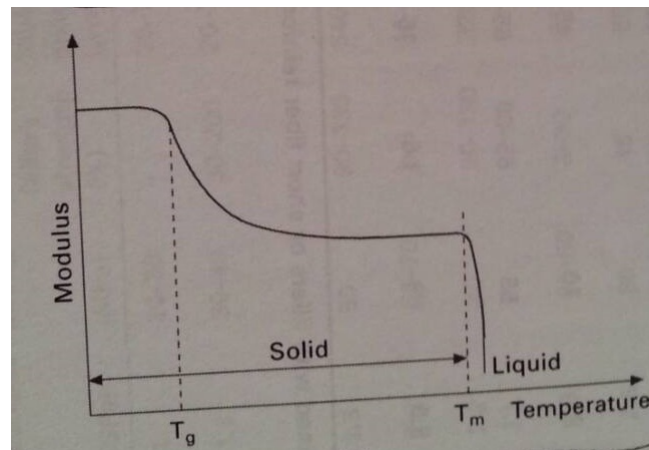


Figure 7.2: The tensile modulus versus temperature of a semi-crystalline polymer.^[10]

temperatures close to this value, as also indicated by Babatope *et al.*^[68] will lead to decreasing the mechanical properties with time.

An interesting topic for future research is to discover which form of annealing has the most optimal results for the parts created by the MarkForged[®] 3D printers. Is printing on a print bed with an elevated temperature the most optimal, or is annealing post-printing more desirable? Also, it is important to know what the most optimal annealing temperatures are and how long the parts have to be annealed.

7.2. Models

When comparing the models with the results obtained from the tensile, compression, and bending mechanical tests it is noted that none of the results match exactly. The tensile model results are roughly a factor 1.53 too high, the bending model result is a factor 2.56 off, while the compression model is only a factor 1.12 off of the actual mechanical test result. The scatter in these values is quite high and it can only be assumed that the simplifications made had a higher impact on the tensile and bending models than on the compression model. As explained in chapter 5 these simplifications were:

- 1 Nylon is modelled as isotropic material
- 2 Carbon Fibre bundles are modelled as orthotropic solid
- 3 Voids are assumed to be only in the carbon fibre reinforced layers
- 4 Voids are assumed to be equally distributed over the sample.
- 5 Perfect adhesion between layers
- 6 CFRP material properties 4x lower in compression model than in the other models.

The compression and tensile models are exactly the same except for the type of loading and the CFRP material data supplied, which is 4 times lower for the compression model. There are several reasons why the results of the tensile simulation are more over-estimated than those of the compression simulation. First of all, as was mentioned in chapter 5, the

material shear moduli G_{12} , G_{13} , and G_{23} have been assumed to be a function of the Young's modulus and poisson's ratio and have not actually been determined by mechanical tests, resulting in higher inaccuracies.

Second, it was already concluded in chapter 4 that several of the assumptions were incorrect, since the microscopic images showed that there are voids in the nylon and that there is no perfect adhesion between the layers due to the existence of these voids. Still these assumptions have been implemented to create a more simple, though more inaccurate model.

Third, the mesh size is another important factor why the simulation results are different from the mechanical test results. The finer the mesh size, the higher the accuracy. In a paper from Dutt^[70] it was found that increasing the mesh size leads to an increase in error of the stresses, but not so much to an error in displacements. The simulated stress seemed to decrease for increasing mesh sizes, which was also shown from fig. 5.3. This would, however, indicate that increasing the mesh size would lead to more accurate results in the case of the simulations performed during this thesis, which contradicts with the literature. The other errors thus have such a large effect that the error in mesh size is overshadowed.

Finally, only elastic material data was supplied and no damage or plastic data was supplied. This does simplify the simulation but increases the overall error.

All in all, these models are far from accurate and correct, but they only serve as benchmarks for designing the chair bracket.

7.3. Comparison of materials

Even though the mechanical properties of this specific carbon fibre reinforced nylon are known to a certain degree, it is interesting to see how the material compares to other materials. First the material will be compared to Aluminium 6061-T6. Then the material will be compared to polyamide-6 (nylon-6) in order to determine how much the mechanical properties have changed. Finally, the composite material will be compared to another unidirectional carbon fibre reinforced composite from the previous paper of the author.^[8]

7.3.1. Aluminium 6061-T6

An interesting topic is to compare the printed material properties with those of aluminium 6061-T6. The MarkForged[®] website stated that printed parts have a higher strength-to-weight ratio than 6061-T6 aluminium. In order to confirm this, the material data of 6061-T6 aluminium is displayed in table 7.1, together with the data obtained for tensile coupons in this research.

As was observed from table 7.1 the aluminium 6061-T6 has a higher tensile modulus than coupons created in this research, however the tensile strength is lower. When comparing the specific moduli and strengths it can be seen that the statement by MarkForged[®] is indeed correct, since the specific strength of the coupons is more than double that of aluminium 6061-T6.

Of course it has to be noted that if the ratio of fibre reinforced layers to nylon layers is increased, the specific modulus would also be equal or higher to that of aluminium 6061-T6. But this is only true for tensile loads in the direction of the fibres. When the force is transverse to the fibres, the specific strength and stiffness of the aluminium 6061-T6 are higher,

Table 7.1: Comparison between material properties of Aluminium 6061-T6 and the printed composite material

	Aluminium 6061-T6	Printed Tensile Coupon
Tensile Modulus [GPa]	68.9	29.8
Tensile Strength [MPa]	310	409
Density [kg/m ³]	2700	1420
Specific Modulus [Nm/kg]	$25.52 * 10^6$	$20.99 * 10^6$
Specific Strength [Nm/kg]	$114.8 * 10^3$	$288.0 * 10^3$

since it is an isotropic material.

So the statement made on the MarkForged[®] website is correct, but not in all cases. Two important factors are that the tensile load must be in the direction of the fibres and that there must be enough reinforced layers in the printed part.

7.3.2. Polyamide-6

When comparing the mechanical properties of nylon, supplied by MarkForged[®] with those of the 14.15 % carbon fibre reinforced nylon coupons created for this research, it can be concluded that the addition of carbon fibres does enhance the mechanical properties significantly. An overview of this is shown in table 7.2.

Table 7.2: Comparison between the mechanical properties of nylon^[12] and the 14.15% carbon fibre reinforced nylon.

Property	Nylon	CFRP Coupon
Tensile Stress at Break [MPa]	54	409
Tensile Modulus [GPa]	0.94	29.8
Tensile Strain at Break [%]	260	1.3
Flexural Strength at Break [MPa]	32	144
Flexural Modulus [GPa]	0.84	7.2
Flexural Strain at Break [%]	n/a	3.2

First of all, MarkForged[®] did not conduct compression experiments on the nylon material. The data on compressive strength of polyamide 6 varies a lot and ranges from 46 *MPa* to 103 *MPa*.^[71, 72] Because of this, no accurate statement on the improvement in compressive strength can be made besides that reinforcing has a positive effect since the compressive strength of the coupons used for this research was 110 *MPa*.

Furthermore, it can be concluded that the tensile stress, tensile modulus, flexural strength and the flexural modulus rise because of the addition of carbon fibres. This does, however, come at a cost. The strain is reduced, and the mass of the coupon increases slightly from 1.15 *g/cm³* to 1.21 *g/cm³*.

7.3.3. comparing to previous research

In previous research^[8] the Mark One[®] was used to print unidirectionally carbon fibre reinforced tensile test coupons with 6 out of 10 layers reinforced with carbon fibre filament. These specimens will be referred to as 6CF specimens.

When checking the tensile test results of these 6CF specimens, the strain varies roughly between 1.3% and 2.0%. The ultimate tensile strength at failure varies between 405 *MPa* and 520 *MPa* and has an average of 464 *MPa* and a median of 461 *MPa*. The maximum scatter from the median is 12.8% which was compared to the data provided from Maekawa *et al.*^[57] who found that the scatter in unidirectional composites was 10.8%. One of the reasons given for the 10.8% scatter in the data was that the fibres were not entirely unidirectional. This same reason was adopted by van der Klift *et al.*^[8], but with the addition that the grinding of the coupons led to higher dimensional inaccuracies and thus a higher scatter in the data.

When comparing this data with the data obtained in this research, several interesting facts were noted. First of all it was indeed correct that the fibres are not entirely unidirectional, but exhibit a slight wave pattern as was visible in fig. 4.13. When looking at the tensile test results it was observed that the median is at 406 *MPa* and that the maximum in the data scattering was only 7.3%. This would lead to assume that the grinding process of the samples in the previous research^[8] has caused an additional 5.5% in scatter.

The 7.3% scatter in tensile stress might be inaccurate due to the relatively low amount of coupons tested. Part of this scatter is due to the fibres not being fully unidirectional, but the main reason are the amount of voids, the adhesion between layers, and the inaccuracies in the dimensions and the measurement of the dimensions.

The mechanical data of the 6CF and the coupons printed in this research is displayed in table 7.3. When checking which of the two samples is closer to the upper limit of the rule of mixtures, it turned out that the 6CF coupons were 14.8% off and the coupons from this research are 11.9% off, with their upper limits being 41.90 *GPa* and 33.35 *GPa* for the 6CF and the tensile test coupons respectively.

Table 7.3: Comparison between the mechanical properties of 6CF specimens^[8] and the 14.15% carbon fibre reinforced tensile test coupons.

Property	6CF	CFRP Coupon
Volume percentage carbon fibres [%]	17.88	14.15
Tensile Stress at Break [MPa]	464	409
Tensile Modulus [GPa]	35.7	29.8
Tensile Strain at Break [%]	1.7	1.3

That the tensile strength and tensile modulus of the 6CF specimen are higher is to be expected since the volume fraction of carbon fibres is higher, but that the tensile strain at break is also higher is against expectations. One of the reasons that this might have happened is due to slipping in the clamps, making the strain look higher than it actually was. When comparing the two carbon fibre reinforced materials, it can be concluded that although the material printed for this research seems mechanically less favourite, the results

are more accurate than for the 6CF specimens, due to no nylon wall layers being ground away. Were the nylon wall layers to be removed, it should be done with great precision in order to improve the mechanical properties of the material, without increasing the scatter.

7.4. The chair part

When looking at the design process using Eiger[®] and Abaqus, it was obvious that there were several limitations in the freedom the designer has. Several of these have been stated before and the one that limited the designer in this case is the nylon floor-, wall-, and ceiling layer requirements. Besides these, the inability to manually lay fibres resulted in a higher product cost and weight overall. Furthermore, for the purpose of simulating the design, it was impossible to export the design with fibre orientation from Eiger[®] and import it into a finite element analysis software package.

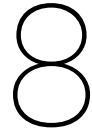
The simulations performed on the designs created in Eiger[®] showed that the part should not fracture when a load of 375 *N* was applied on an arm with a length of 68 *cm*. Also the outer fibre reinforcements were indicated to have the highest stresses in both tensile and in compression.

During the test, it was discovered that the chair bracket indeed could handle the force of at least 375 *N* without fracturing. However, the downward displacement of the endpoint of the arm was almost 20 *cm*. Two reasons for this were discovered. The first was that the printer had not printed the holes at the exact locations, meaning that smaller bolts had to be used in order to mount the part to the test set-up. These smaller bolts had rotational freedoms, allowing them to rotate in such a way that downward displacement of the arm was increased. Moreover, the smaller bolts also have a smaller contact area, thus increasing the stresses in the material locally.

A second reason is that the nylon wall layers covering the holes, gave way to the force exerted on by the bolts, as was shown in fig. 6.13. The fibre reinforcements, that are 0.8 *mm* away from the edge of the pin-holes are capable of withstanding the loads, but the nylon is not. Due to this damage, the bolts eventually got more freedom to move, increasing the displacement of the arm.

Bolts with a perfect fit can reduce both these problems, by reducing the rotational degrees of freedom to one, and by increasing the surface area where the bolt exerts force on, thus lowering the overall stress on the hole.

Of course, the results obtained with this test only show that the chair bracket (assuming that bolts with a perfect fit resolve the two above stated problems) can handle a static load without fracturing. In service, however, the chair bracket will be subjected to not only static, but also dynamic loads. Since this research only focussed on the static load, it will be left to future research to determine the capability of the printed material to withstand dynamic loads without fracturing or even deforming plastically.



Conclusion

When answering the main research question, "Is the composite material with continuous carbon fibres printed by a FDM based 3D printer feasible for structural aerospace applications?", the answer is no.

Since, even though the structural part in this research did not fracture, damage in the form of plastic deformation was observed, which is highly undesirable.

The answer to the main research question is influenced both by the type of printer used, as well as the part that was chosen.

The printer used for this research was the Mark Two[®] from MarkForged[®] and the structural aerospace part chosen was a chair bracket that has as task to transfer the loads from the back seat to the chair. A more complex part, like a helicopter torque link, could not be optimally printed by the printer since the fibres could not be deposited in the directions of all the loads. Several improvements to the printer might make it possible to print more complex parts, with the fibres in the favourable directions. These improvements are mainly software related, like the ability to deposit fibres with a custom orientation, or the ability to change the printing temperature and print head velocity.

All in all the technology is a great improvement in terms of printing composites with continuous fibres. Even though a relatively high amount of void area was discovered in the printed parts, a tensile strength of 409 *MPa* was reached and the printed material has a higher strength to weight ratio than aluminium 6061-T6. The compressive strength was lower than the tensile strength and was found to be 110 *MPa*, mainly because the tensile strength is a fibre dominated property, while the compressive strength is also very matrix dominated and is thus influenced more by the presence of voids.

The flexural strength of the printed material was 144 *MPa*, but a more optimal stacking of nylon and carbon fibre reinforced layers can improve the flexural strength, by having the fibre reinforced layers positioned closer to the bottom and top of the coupon where the tensile and compressive forces are the largest, and having the nylon layers in the centre to create a sandwich structure.

Future research into reducing the void area, by e.g. annealing the parts, or printing on a heated print bed, can increase the mechanical properties even more. Also testing the material in a dynamic nature, or conducting impact tests will give a greater insight in the possibilities for this type of 3D printed unidirectional carbon fibre reinforced composite material.

Bibliography

- [1] custompartnet, “Selective laser sintering (sls).” <http://www.custompartnet.com/wu/selective-laser-sintering>, 2008. [Online; accessed 29-November-2016].
- [2] custompartnet, “Laminated object manufacturing.” <http://www.custompartnet.com/wu/laminated-object-manufacturing>, 2008. [Online; accessed 29-November-2016].
- [3] custompartnet, “3d printing.” <http://www.custompartnet.com/wu/3d-printing>, 2008. [Online; accessed 29-November-2016].
- [4] custompartnet, “Stereolithography.” <http://www.custompartnet.com/wu/stereolithography>, 2008. [Online; accessed 29-November-2016].
- [5] custompartnet, “Fused deposition modeling (fdm).” <http://www.custompartnet.com/wu/fused-deposition-modeling>, 2008. [Online; accessed 29-November-2016].
- [6] Frank Margetan, “modeling cracks and delaminations carbon fiber composites.” <https://www.cnde.iastate.edu/ultrasonics-and-composites/modeling-cracks-and-delaminations-carbon-fiber-composites-frank-margetan>, 2015. [Online; accessed 19-April-2016].
- [7] Abaqus, Inc., “Abaqus lecture 2 - elements.” <http://imechanica.org/files/12-elements.pdf>, 2005. [Online; accessed 26-Jun-2017].
- [8] F. van der Klift, Y. Koga, A. Todoroki, M. Ueda, Y. Hirano, and R. Matsuzaki, “3D printing of continuous carbon fibre reinforced thermo-plastic (CFRTP) tensile test specimens,” *Open Journal of Composite Materials*, vol. 6, pp. 18–27, 2016.
- [9] H. Thuis, “Development of a composite torque link for helicopter landing gear applications,” *Proceedings of the Twelfth International Conference on Composite Materials, Paris-rance, July 5th-9th, 1999*.
- [10] P. Mallick, *Materials, design and manufacturing for lightweight vehicles*. Woodhead Publishing Ltd., 2010.
- [11] Skelton J., “Fused deposition modeling. 3d printers and 3dprinting technologies almanac.” <http://3d-print.blogspot.com/2008/02/fused-deposition-modelling.html>, 2008. [Online; accessed 10-Apr-2017].
- [12] MarkForged, *Mechanical Properties*, 2016.
- [13] Mal-Bac Inc., “history of composites.” <http://www.mar-bal.com/language/en/applications/history-of-composites/>, 2016. [Online; accessed 18-April-2016].

- [14] X. Yan and P. Gu, "A review of rapid prototyping technologies and systems," *Computer-Aided Design*, vol. 28, no. 4, pp. 307–318, 1996.
- [15] ASTM, "F2792-10e1 standard terminology for additive manufacturing technologies.." ASTM International, 2010.
- [16] S. Huang, P. Liu, A. Mokasdar, and L. Hou, "Additive manufacturing and its societal impact: a literature review," *Int J Adv Manf Technol*, vol. 67, pp. 1191 – 1203, 2013.
- [17] Z. W., Y. Liu, J. Deng, Y. Guo, K. Jiang, P. Wang, Z. Yu, and Y. Shen, "Laser intensity effect on mechanical properties of wood-plastic composite parts fabricated by selective laser sintering," *Journal of Thermoplastic Composite Materials*, vol. 26, pp. 125–136, 2013.
- [18] M. Salmi, K.-S. Paloheimo, J. Tuomi, J. Wolff, and A. Mäkitie, "Accuracy of medical models made by additive manufacturing (rapid manufacturing)," *Journal of Cranio-Maxillofacial Surgery*, vol. 41, no. 7, pp. 603 – 609, 2013.
- [19] J. Giannatsis and V. Dedoussis, "Additive fabrication technologies applied to medicine and health care: a review," *The International Journal of Advanced Manufacturing Technology*, vol. 40, no. 1, pp. 116–127, 2009.
- [20] F. Bos, R. Wolfs, Z. Ahmed, and T. Salet, "Additive manufacturing of concrete in construction: potentials and challenges of 3d concrete printing," *Virtual And Physical Prototyping*, vol. 11, no. 3, pp. 209–225, 2016.
- [21] N. Labonnote, A. Rønquist, B. Manum, and P. Rüther, "Additive construction: State-of-the-art, challenges and opportunities," *Automation in Construction*, vol. 72, no. 3, pp. 347 – 366, 2016.
- [22] K. V. Wong and A. Hernandez, "A review of additive manufacturing," *ISRN Mechanical Engineering*, vol. 2012, 2012.
- [23] D. Pham and R. Gault, "A comparison of rapid prototyping technologies," *International Journal of Machine Tools and Manufacture*, vol. 38, pp. 1257 – 1287, 1998.
- [24] Rain Noe, "Production methods: What's the difference between selective laser sintering, direct metal laser sintering, laser melting and lasercusing?." <http://www.core77.com/posts/26457/production-methods-whats-the-difference-between-selective-laser-sintering-direct-m> 2014. [Online; accessed 28-November-2016].
- [25] A. Simchi and H. Pohl, "Direct laser sintering of iron-graphite powder mixture," *Materials Science and Engineering A*, vol. 383, pp. 191 – 200, 2004.
- [26] J.-P. Kruth, B. van der Schueren, J. Bonse, and B. Morren, "Basic powder metallurgical aspects in selective metal powder sintering," *CIRP Annals - Manufacturing Technology*, vol. 45, pp. 183 – 186, 1996.

- [27] O. Scott-Emuakpor, J. Schwartz, T. George, C. Holycross, C. Cross, and J. Slater, "Bending fatigue life characterisation of direct metal laser sintering nickel alloy 718," *FFEMS*, vol. 38, pp. 1105 – 1117, 2015.
- [28] M. Schmidt, D. Pohle, and T. Rechtenwald, "Selective laser sintering of peek," *CIRP Annals - Manufacturing Technology*, vol. 56, pp. 205–208, 2007.
- [29] K. K. B. Hon and T. J. Gill, "Selective laser sintering of sic/polyamide composites," *CIRP Annals - Manufacturing Technology*, vol. 52, pp. 173 – 176, 2003.
- [30] N. Hopkinson, C. E. Majewski, and H. Zarringhalam, "Quantifying the degree of particle melt in selective laser sintering," *CIRP Annals - Manufacturing Technology*, vol. 58, pp. 197 – 200, 2009.
- [31] C. Z. Yan, Y. S. Shi, J. S. Yang, and L. Xu, "Preparation and selective laser sintering of nylon-12-coated aluminum powders," *Journal of Composite Materials*, vol. 43, pp. 1835 – 1851, 2009.
- [32] D. Gu, H. Wang, and G. Zhang, "Selective laser melting additive manufacturing of ti-based nanocomposites: The role of nanopowder," *Metallurgical and Materials Transactions A*, vol. 45, pp. 464 – 476, 2014.
- [33] M. Agarwala, D. Bourell, J. Beaman, H. Marcus, and J. Barlow, "Direct selective laser sintering of metals," *Rapid Prototyping Journal*, vol. 1, pp. 26 – 36, 1995.
- [34] S. Kumar and J.-P. Kruth, "Composites by rapid prototyping technology," *Materials and Design*, vol. 31, pp. 850–856, 2010.
- [35] J.-P. Kruth, M. Leu, and T. Nakagawa, "Progress in additive manufacturing and rapid prototyping," *CIRP Annals - Manufacturing Technologies*, vol. 47, no. 2, pp. 525 – 540, 1998.
- [36] M. Feygin and S. Pak, "Laminated object manufacturing apparatus and method," Mar. 2 1999. US Patent 5,876,550.
- [37] E. Sachs, M. Cima, P. Williams, D. Brancazio, and J. Cornie, "Three dimensional printing: Rapid tooling and prototypes directly from a cad model," *J Engng Ind. Trans. ASME*, vol. 114, pp. 481–488, 1992.
- [38] D. Marks, "3d printing advantages for prototyping applications." <http://www.articlesbase.com/technology-articles/3d-printing-advantages-for-prototyping-applications-1843958.html>, 2010. [Online; accessed 29-November-2016].
- [39] D. Pham and C. Ji, "Design for stereolithography," *Proceedings - Institution of Mechanical Engineers Part C Journal of Mechanical Engineering Science*, vol. 214 part 5, pp. 635 – 640, 2000.
- [40] Stratasy, "Fdm technology." <http://www.stratasys.com/3d-printers/technologies/fdm-technology>, 2016. [Online; accessed 29-November-2016].

- [41] S. Christopherson, "The machine that prototyped itself," *Prototyping Technology International*, pp. 140–143, 1998.
- [42] M. Thymianidis, C. Achillas, D. Tzetzis, and E. Iakovou, "Modern additive manufacturing technologies: An up-to-date synthesis and impact on supply chain design," *Int J Adv Manuf Technol*, vol. 73, pp. 913 – 928, 2014.
- [43] A. Boschetto and L. Bottini, "Accuracy prediction in fudes deposition modeling," *Int J Adv Manuf Technol*, vol. 73, pp. 913 – 928, 2014.
- [44] J. Skelton, "Fused deposition modeling. 3d printers and 3d-printing technologies." <http://3d-print.blogspot.nl/2008/02/fused-deposition-modelling.html>, 2008. [Online; accessed 29-November-2016].
- [45] I. D. Harris, "Additive manufacturing: A transformational advanced manufacturing technology," *ADVANCED MATERIALS & PROCESSES*, vol. 170, pp. 25–29, may 2012.
- [46] B. Berman, "3-D printing: The new industrial revolution," *Business Horizons*, vol. 55, pp. 155–162, 2012.
- [47] F. Rengier, A. Mehndiratta, and H. von Tengg-Kobligk, "3D printing based on imaging data: review of medical applications," *Int J CARS*, vol. 5, pp. 335–341, 2010.
- [48] C. Soutis, "Carbon fiber reinforced plastics in aircraft construction," *Material Science and Engineering A*, vol. 412, pp. 171–176, 2005.
- [49] J. Czyzewski, P. Burzynski, P. Gawel, and J. Meisner, "Rapid prototyping of electrically conductive components using 3d printing technology," *Journal of Materials Processing Technology*, vol. 209, pp. 5281–5285, 2009.
- [50] H. Tekinalp, V. Kunc, G. Velez-Garcia, C. Duty, L. Love, A. Naskar, C. Blue, and S. Ozcan, "Highly oriented carbon fiber-polymer composites via additive manufacturing," *Composites Science and Technology*, vol. 105, pp. 144–150, 2014.
- [51] F. Ning, W. Cong, J. Qiu, J. Wei, and S. Wang, "Additive manufacturing of carbon fiber reinforced thermoplastic composites using fused deposition modeling," *Composites Part B: Engineering*, vol. 80, pp. 369–378, 2015.
- [52] N. Taniguchi, T. Nishiwaki, and H. Kawada, "Tensile strength of unidirectional cfrp laminate under high strain rate," *Adv, Composite Mater.*, vol. 16, pp. 167–180, 2007.
- [53] C. Hsueh, "Young's modulus of unidirectional discontinuous-fibre composites," *Composites Science and Technology*, vol. 60, pp. 2671 – 2680, 2000.
- [54] T. Okabe and N. Takeda, "Size effect on tensile strength of unidirectionalCFRP composites - experiment and simulation," *Composite Science and Technology*, vol. 62, pp. 2053–2064, 2002.
- [55] E. K. Gamsteds and R. Talreja, "Fatigue damage mechanisms in unidirectional carbon-fibre-reinforced plastics," *Journal of Materials Science*, vol. 34, pp. 2535–2546, 1999.

- [56] D. S. Faquhar, F. M. Mutrelle, S. L. Phoenix, and R. L. Smith, "Lifetime statistics for single graphite fibres in creep rupture," *Journal of Material Science Letters*, vol. 24, pp. 2151–2164, 1989.
- [57] Z. Maekawa, H. Hamada, A. Yokoyama, and S. Ishibashi, "Reliability evaluation on mechanical characteristics of cfrp," in *1st Japan Inter. SAMPE Symp.*, pp. 1274–1279, SAMPE, nov 28 - dec 1 1989.
- [58] M. Namiki, M. Ueda, A. Todoroki, Y. Hirano, and R. Matsuzaki, "3D Printing of Continuous Fiber Reinforced Plastic," in *Society of the Advancement of Material and Process Engineering (Seattle)*, p. 6, SAMPE, jun. 2014, jun 2014.
- [59] R. Matsuzaki, M. Ueda, M. Namiki, T.-K. Jeong, H. Asahara, K. Horiguchi, T. Nakamura, A. Todoroki, and Y. Hirano, "Three-dimensional printing of continuous-fiber composites by in-nozzle impregnation," *Scientific Reports*, vol. 6, 2016.
- [60] G. W. Melenka, B. K. O. Cheung, J. S. Schofield, M. R. Dawson, and J. P. Carey, "Evaluation and prediction of the tensile properties of continuous fiber-reinforced 3d printed structures," *Composite Structures*, vol. 153, pp. 866 – 875, 2016.
- [61] Markforged, Inc., "The mark two." <https://markforged.com/mark-two/#specifications>, 2016. [Online; accessed 29-November-2016].
- [62] ASTM D3039–14, "Standard test method for tensile properties of polymer matrix composite materials," 2014. [Online; accessed 24-November-2016].
- [63] ASTM D790–03, "Standard test method for tensile properties of plastics," 2003. [Online; accessed 24-November-2016].
- [64] European Association of Aerospace Industries, "Din en2850," 1997.
- [65] N. Jia, H. Fraenkel, and V. Kagan, "Effects of moisture conditioning methods on mechanical properties of injection molded nylon 6," *Journal of Reinforced Plastics and Composites*, vol. 23, no. 7, pp. 7 – 10, 2004.
- [66] Dassault Systèmes, "Abaqus/cae user's guide." <http://abaqus.software.polimi.it/v6.14/books/usi/default.htm>, 2014. [Online; accessed 26-Jun-2017].
- [67] makeitFrom.com, "Unfilled peek." <https://www.makeitfrom.com/material-properties/Unfilled-PEEK>, 2017. [Online; accessed 13-Oct-2017].
- [68] B. Babatope and D. Isaac, "Annealing of isotropic nylon-6,6," *Polymer*, vol. 33, no. 8, pp. 1664 – 1668, 1990.
- [69] SpecialChem, "Glass transition temperature." <https://omnexus.specialchem.com/polymer-properties/properties/glass-transition-temperature>, 2017. [Online; accessed 21-Oct-2017].
- [70] A. Dutt, "Effect of mesh size on finite element analysis of beam," *SSRG International Journal of Mechanical Engineering*, vol. 2, no. 12, pp. 7 – 10, 2015.

- [71] matbase, "Pa6." <https://www.matbase.com/material-categories/natural-and-synthetic-polymers/thermoplastics/engineering-polymers/material-properties-of-polyamide-6-nylon-6-pa-6.html#properties>, 2017. [Online; accessed 13-Oct-2017].
- [72] Advanced Industrial, "Pa6, unfilled, cast nylon (astm data)." <http://www.cncplastics.com/pdf/Cast%20Nylon%206.pdf>, 2017. [Online; accessed 13-Oct-2017].

Appendix A1

Graphs of the Individual Tensile Tests

In this appendix the graphs of the 5 tensile test coupons will be shown individually. Note that the load is on the x-axis in [kN] and the strain in [%] on the y-axis.

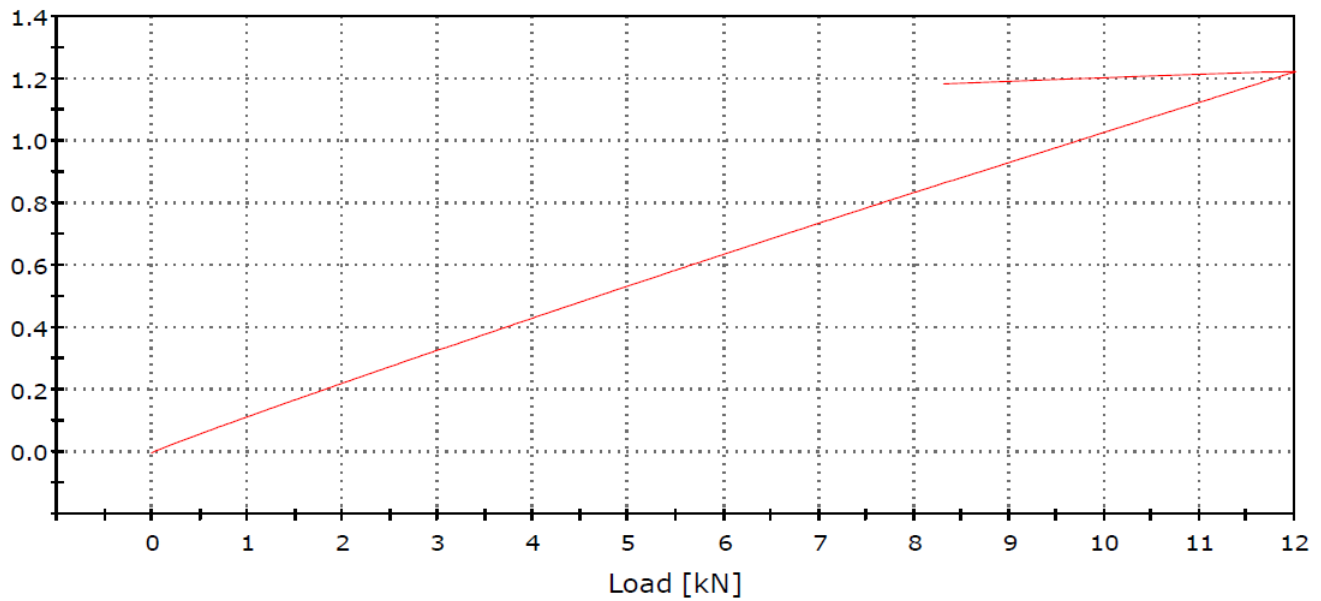


Figure A1.1: Individual stress-strain graph of the T1 coupon

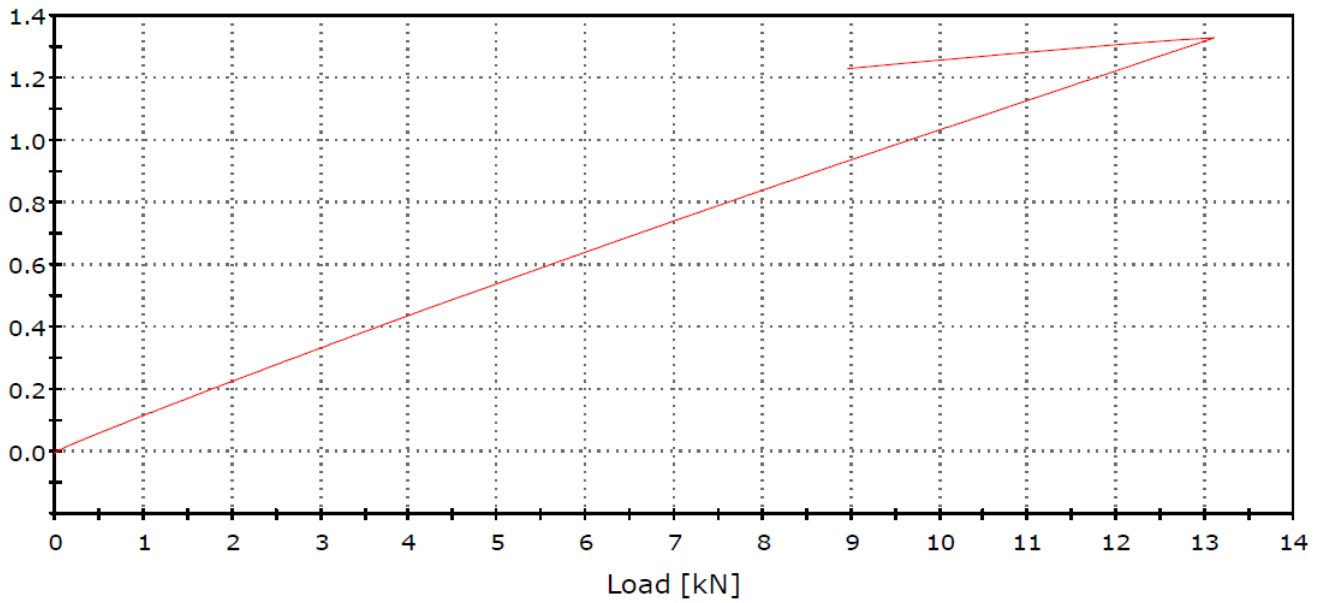


Figure A1.2: Individual stress-strain graph of the T2 coupon

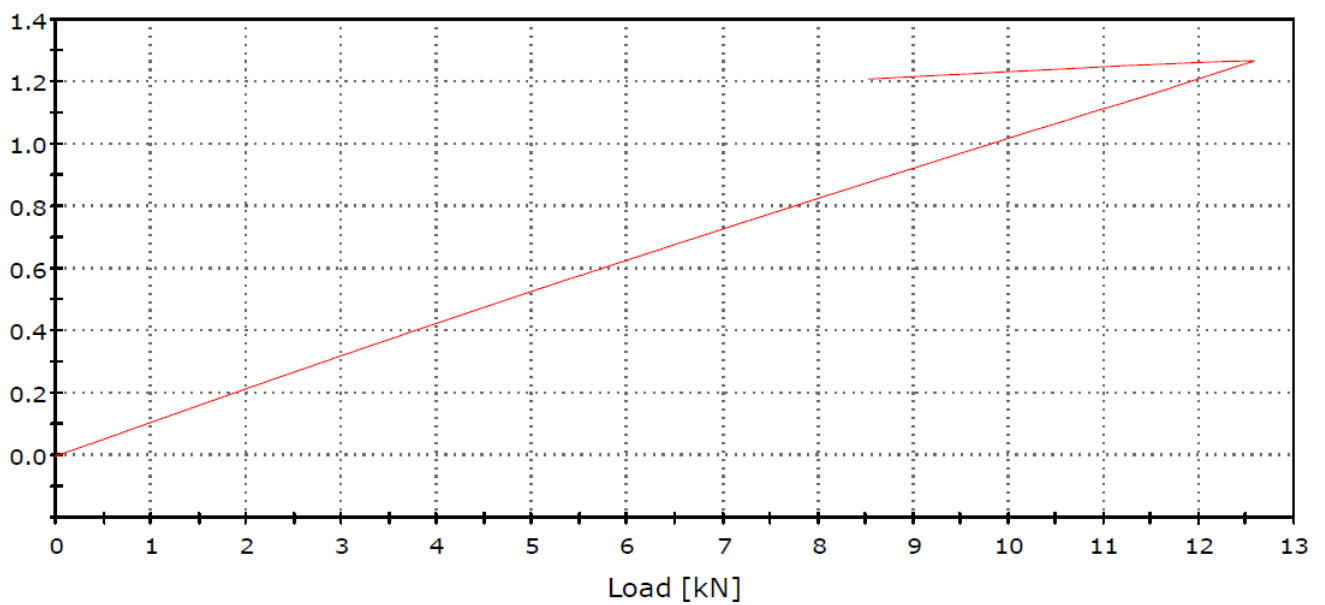


Figure A1.3: Individual stress-strain graph of the T3 coupon

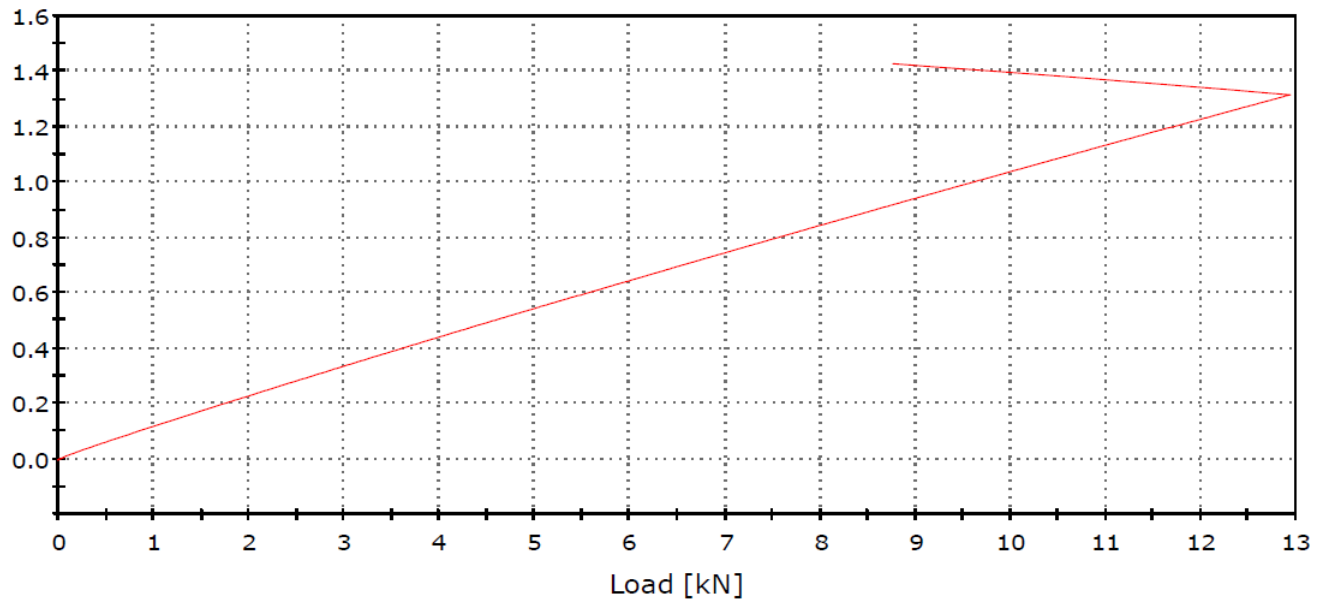


Figure A1.4: Individual stress-strain graph of the T4 coupon

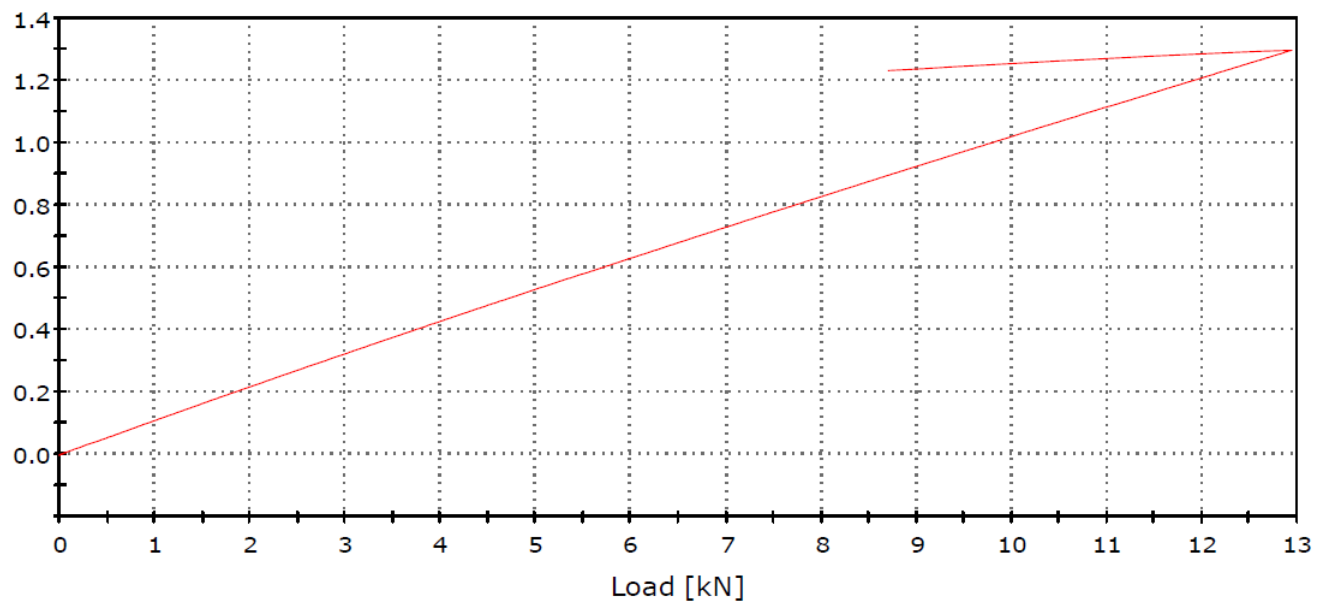


Figure A1.5: Individual stress-strain graph of the T5 coupon

Appendix A2

Graphs of the Individual Compression Tests

In this appendix the graphs of the 5 compression test coupons will be shown individually. Note that the strain is on the x-axis in *mm* and the load in *kN* on the y-axis.

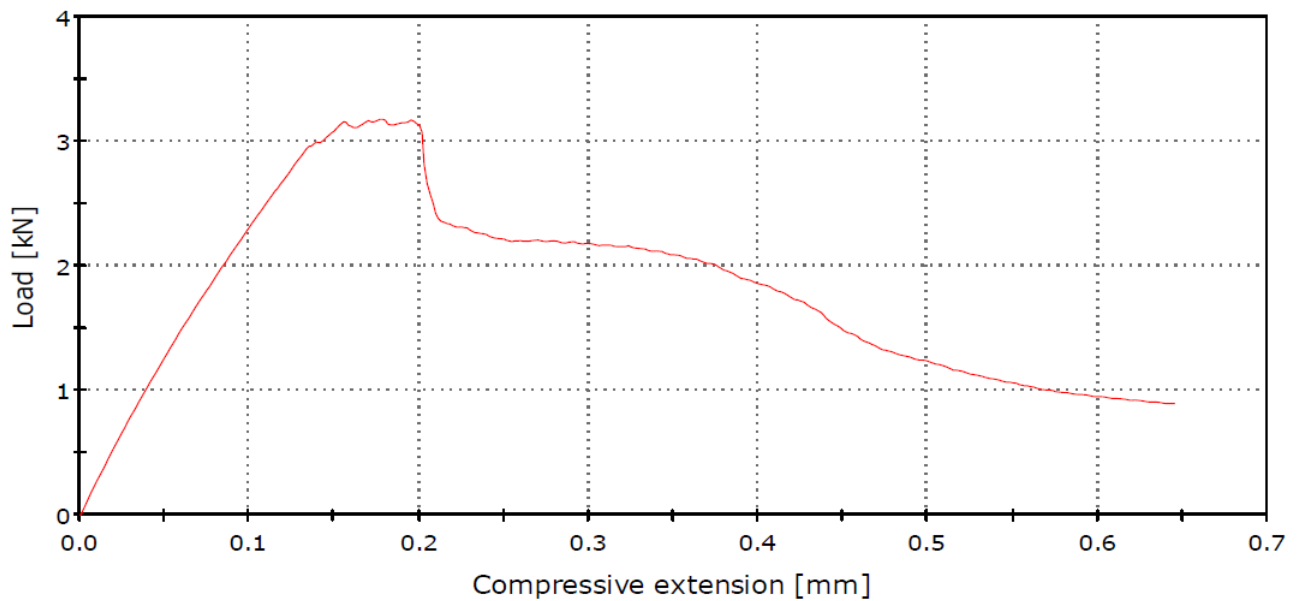


Figure A2.1: Individual stress-strain graph of the C1 coupon

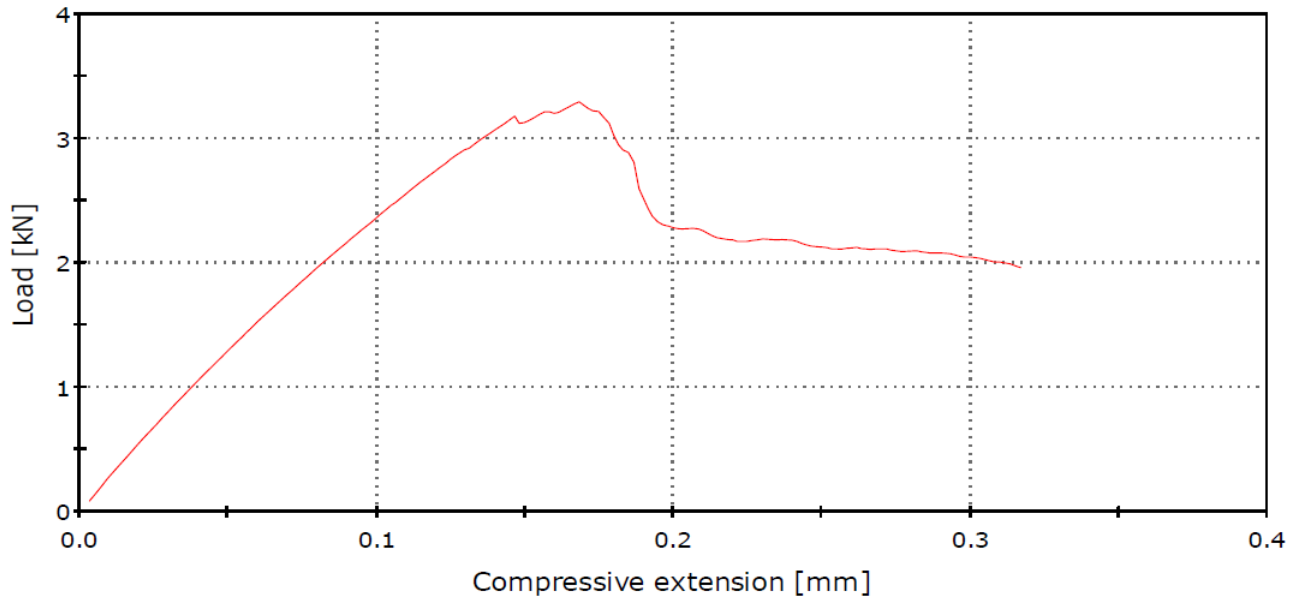


Figure A2.2: Individual stress-strain graph of the C2 coupon

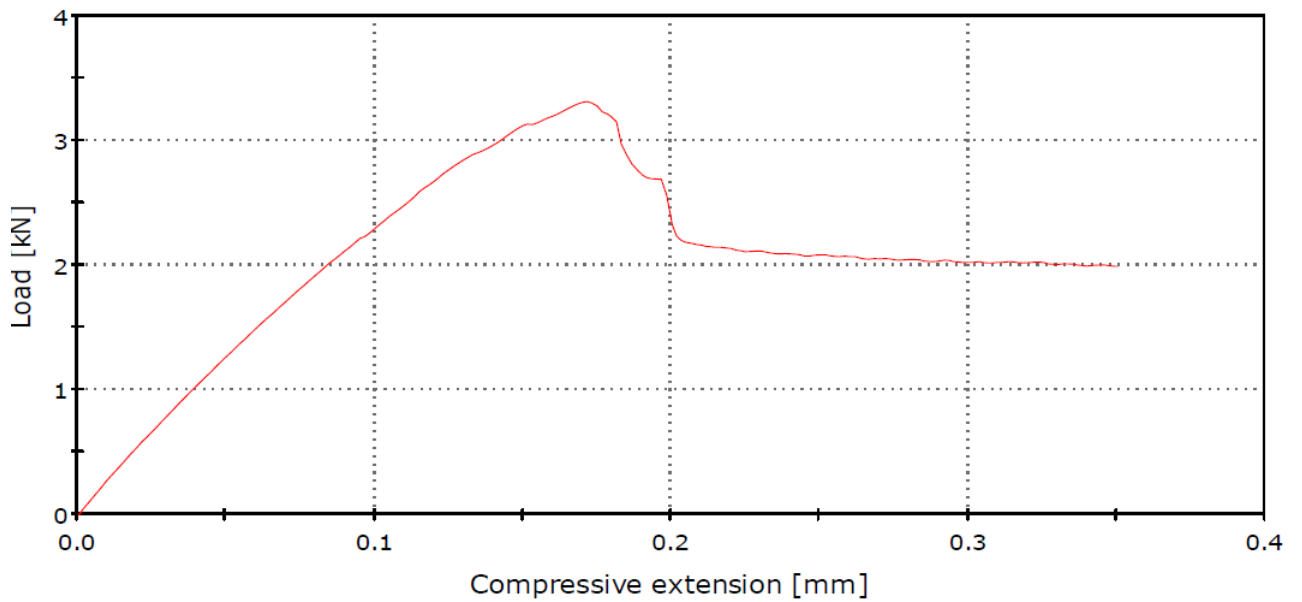


Figure A2.3: Individual stress-strain graph of the C3 coupon

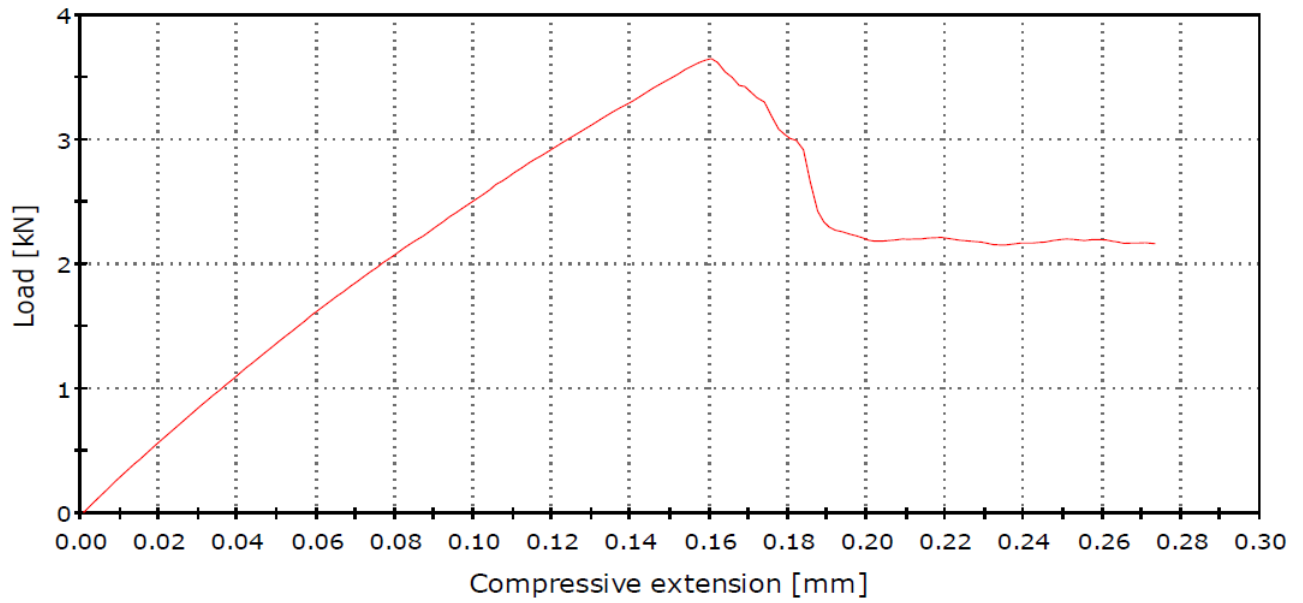


Figure A2.4: Individual stress-strain graph of the C4 coupon

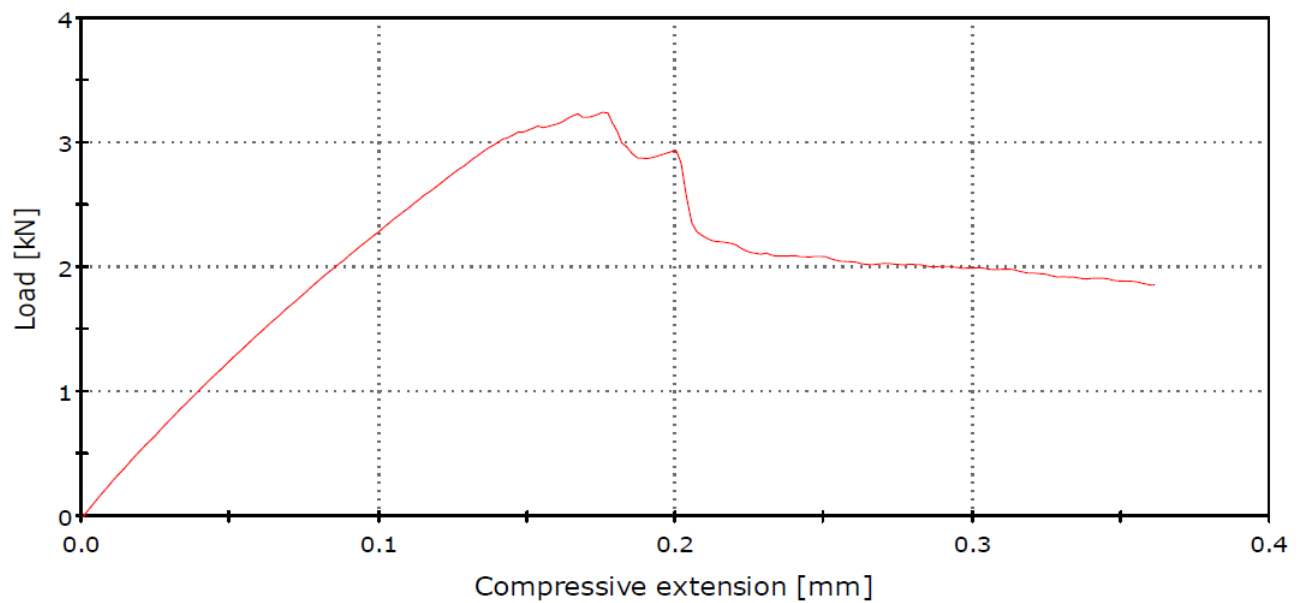


Figure A2.5: Individual stress-strain graph of the C5 coupon

Appendix A3

Graphs of the Individual Bending Tests

In this appendix the 4 graphs of the individual three-point bending tests are shown. Note that because of the failed data acquisition on the B1 coupon, no test data was obtained, and there is thus no B1 graph. Also be aware that the extension in [mm] on the x-axis and the load is on the y-axis in [N].

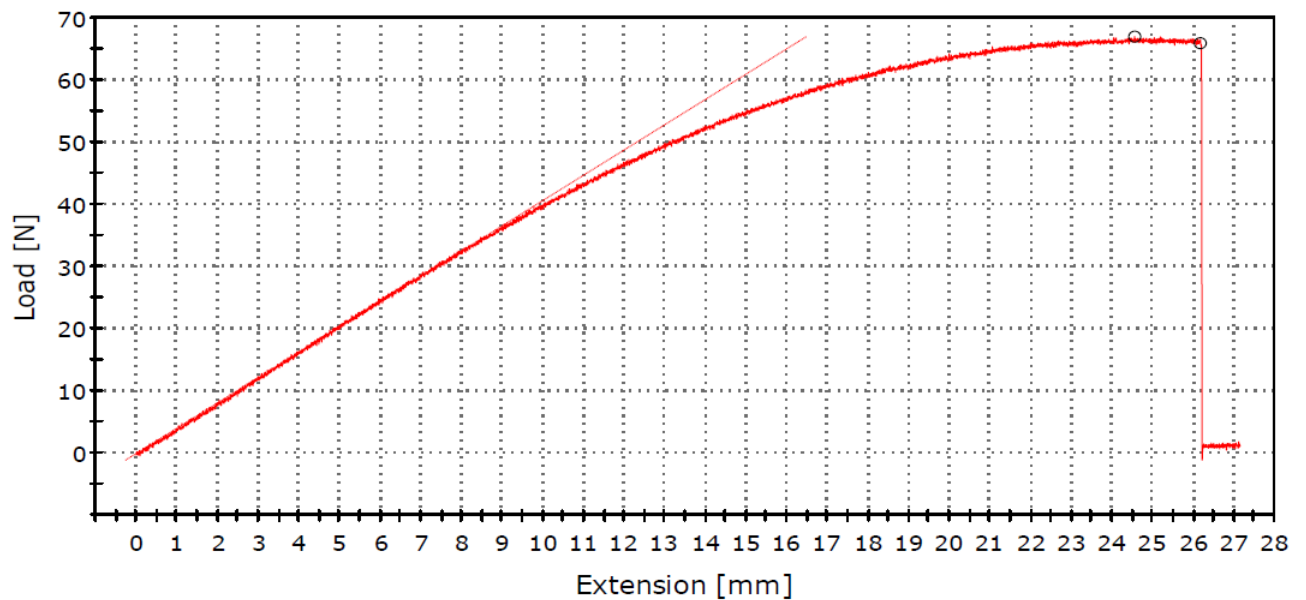


Figure A3.1: Individual stress-strain graph of the B2 coupon

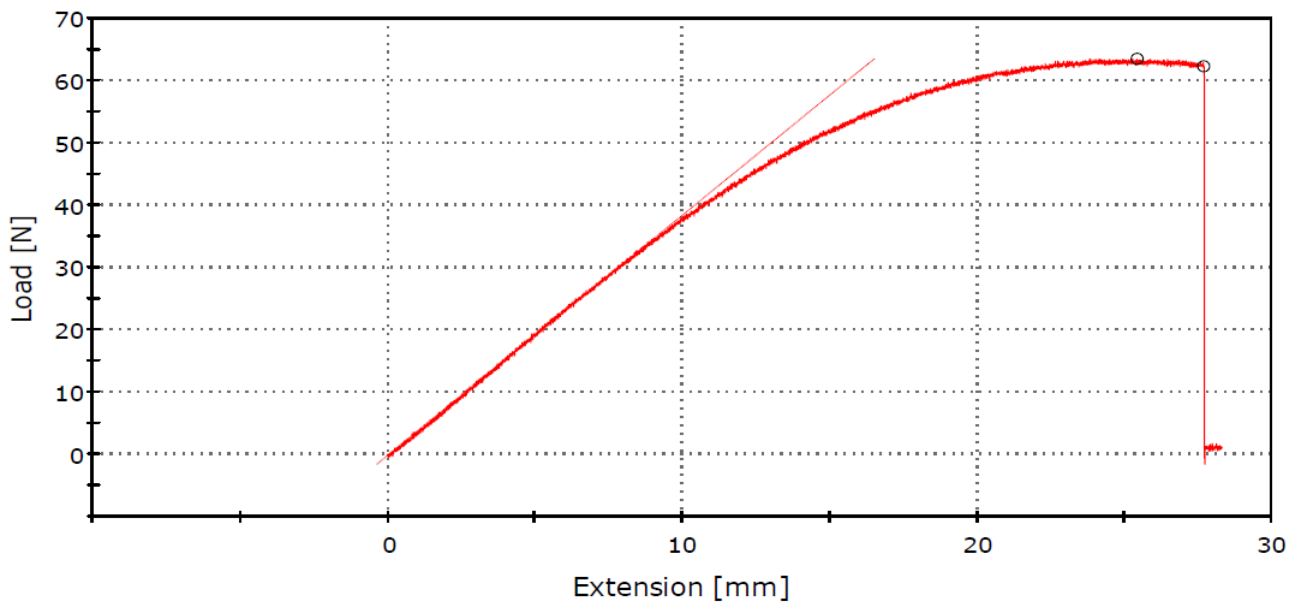


Figure A3.2: Individual stress-strain graph of the B3 coupon

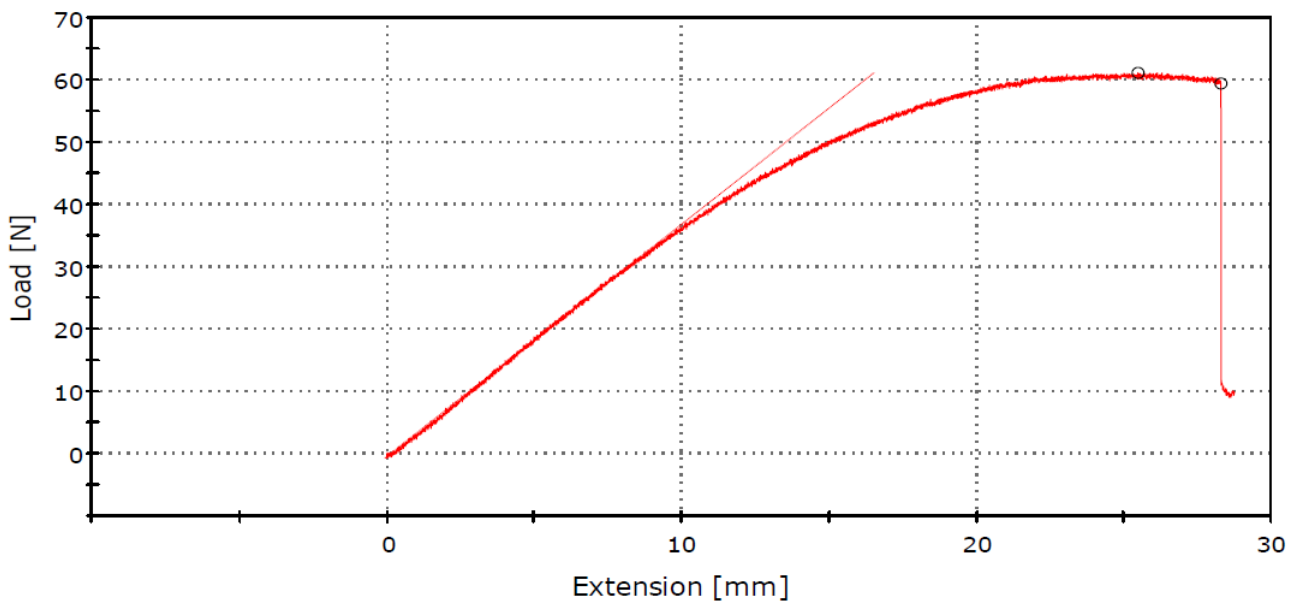


Figure A3.3: Individual stress-strain graph of the B4 coupon

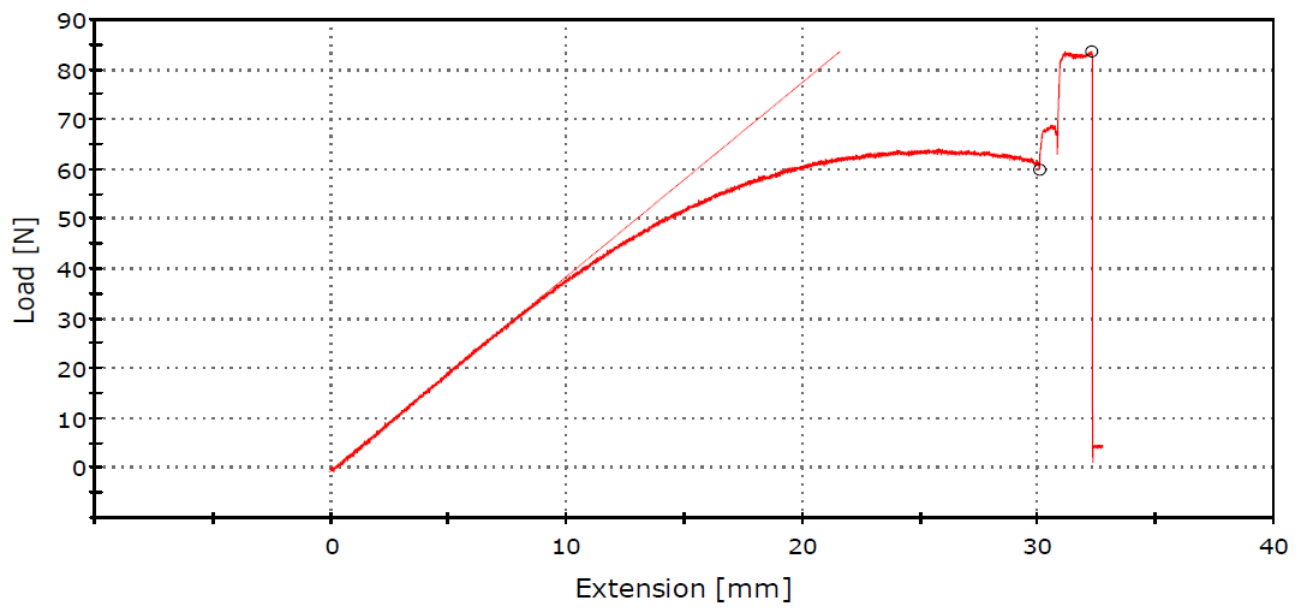


Figure A3.4: Individual stress-strain graph of the B5 coupon

Appendix B

Fibre bundle tensile test

To determine the properties of the fibres, a few micro tensile tests were performed on the carbon fibre filament bundles. These tests work just as a tensile test, but then with everything scaled down.

In total four carbon fibre bundles were tested and were loaded until failure. Since the installation is normally used for testing small metal parts or wires, the grips were not used to the resin material that surrounds the fibres. Some of the tests failed due to the fibre bundle slipping from the clamps. On average the force at which the samples failed was 110 *N*, which was assumed to be the value at which the fibre bundles failed.

Fibre property calculation

With the force at failure to be estimated at 100 *N*, the tensile strength of the bundle and of the fibres itself could be calculated. Here it was assumed that there are no voids in the fibre filament bundle. Since the diameter of the bundle was known to be 0.374 *mm* and the area and thus the tensile strength of the bundle could be calculated. The area is 0.10985 *mm*², leading to a tensile strength of 1001 *MPa*.

Do note that this is the tensile strength of the fibre filament bundle, and not of the carbon fibres. Only 34.5% of the bundle consists of carbon fibres. The rest of the material is assumed to be nylon, which has a tensile strength of 54 *MPa*. By using the rule of mixture, the tensile strength of the carbon fibres was determined to be 2800 *MPa*.